CAAP Final Report

Date of Report: September 20, 2022

Prepared For: *U.S. DOT Pipeline and Hazardous Materials Safety Administration*

Contract Number: 693JK31950005CAAP

Project Title: *An Unmanned Aerial System of Visible Light, Infrared and Hyperspectral Cameras with Novel Signal Processing and Data Analytics*

Prepared By: *Pengfei Ma, Tarutal Ghosh Mondal, Ying Zhuo, Zhenhua Shi, Bo Shang, Liujun Li, and Genda Chen from Missouri University of Science and Technology.*

Contact Information: *Genda Chen, Ph.D., P.E., Email: gchen@mst.edu, Phone: (573) 341-4462*

Summary of Accomplishments from This Project

This project (September 30, 2019 - September 30, 2022) was completed. During the project performance period, we completed three publications, including one paper under review:

1. Pengfei Ma, Ying Zhuo, Genda Chen, and Joel Burken. "Gas Induced Vegetation Stress Leakage Identification and Discrimination via Hyperspectral Reflectance," Remote Sensing of Environment (under review).
2. Pengfei Ma, Liujun Li, and Genda Chen. "Gas Leakage Detection with Hyperspectral Imagery-Based Vegetation Stress Indices," Pipeline Research Council International 2021 Virtual Research Exchange, March 2-5, 2021.
3. Pengfei, Zhenhua Shi, and Genda Chen. "Pipeline Leakage Detection by Mapping Vegetation Stress Indices from Hyperspectral Imaging," Poster Competition (2^{nd} placement award), Geo-Resolution 2022, September 2022.

Two Ph.D. students, three post-doctoral fellows, and one research professor were trained to work on this project:

- Pengfei Ma, Ph.D. Student (September 2019 – September 2022); Mr. Ma's Ph.D. study was partially supported on this project.
- Ying Zhuo, Ph.D. Student (September 2019 – September 2022); Mr. Zhuo assisted Pengfei in this project during the field and laboratory study. His Ph.D. research is funded by another PHMSA CAAP Project No. 693JK31850012.
- Tarutal Ghosh Mondal, Post-doctoral Fellow (April 2022 – January 2023); Dr. Mondal contributed to the classification of plant stress states from deep learning of hyperspectral images on this PHMSA CAAP Project.
- Liujun Li, Research assistant professor (November 2021 – August 2022); Dr. Li started the flight mission plan and trained other team members for follow-up work.
- Zhenhua Shi, Post-doctoral Fellow (June 2022 – September 2022); Dr. Shi as a FAA approved pilot developed and executed flight mission plans.
- Bo Shang, Post-doctoral Fellow (September 2019 – September 2022); Dr. Shang contributed to the preliminary design of the integrated drone equipped with remote sensos.

Executive Summary

This project attempts to enhance pipeline safety by enabling a routine and maintenance inspection of pipelines using remote sensing with signal processing and data analytics. In this study, the stress condition of ground surface vegetations was considered indicative of the effect of methane gas leakage along underground pipelines, although other surface features of above-ground pipelines, such as mechanical damage and coating deterioration (e.g., pinholes and color changes), would be equally effective indicators. Vegetation data were collected, processed, and applied towards condition and risk assessments for pipeline operators. A manual or fully-automated unmanned aerial system (UAS) equipped with a RGB camera, an infrared camera, a hyperspectral camera, and a LiDAR scanner was designed and integrated to support this project for data collection tasks. The collected data such as spectra were processed to derive parameters (e.g., reflectance derivatives with respect to wavelength) that are sensitive to stress variants, and compressed by principal component analysis to improve computational efficiency and facilitate data analytics (e.g., linear/quadratic discriminant analysis) for vegetation stress discrimination and thus gas leakage detection. The stress condition was further classified using a deep learning approach, which can easily process a large set of imagery.

Laboratory tests on three plants (Grass. Shrub Gem, and Shrub South) under natural stressors (drought exposure, heavy metal contamination, and salinity impact), gas treatment, and no treatment were conducted to characterize the effects of different stressors on various vegetations and develop an effective method for gas detection using hyperspectral reflectance as it contains variance of the vegetations derived from exposure to the stress. It was found that the linear discriminant analysis can effectively identify gas treated vegetations with 79% - 91% accuracy from two-class detection (ideal scenario with no noise) and the quadratic discriminant analysis identified gas treated vegetations at a reduced accuracy (69% - 76%) from five-class detection due to the distraction of three natural stressors (extreme scenario with multiple types of noise). When distracted by one natural stressor (practical scenario with one type of noise), the quadratic discriminant analysis can differentiate gas treatment from the distracted natural stressor and the unstressed reference with 78% - 91% accuracy from three-class detection. The first derivative of visible and near infrared-ranged spectra (400-1000 nm) led to the highest accuracy in nearly all detection cases. The first derivative can significantly reduce the number of principal components

required for successful classification. Gas stress development in different plants was also found to vary greatly. Grass was more tolerant than the shrubs to the impact of gas treatment. To achieve a 75% or higher probability gas stress on the plants, 32, 37 and 56 days are required for shrub Gem, shrub South and Grass, respectively.

Open field tests with PVC pipelines buried three feet deep in four trenches were conducted to develop and validate a data-driven approach for the detection of gas-induced vegetation stress. Two pipelines were untreated as references and two were treated with methane gas on a regular basis. It was found that hyperspectral mapping facilitated a rapid identification of the differences between different trenches through one-pass flight of the drone with integrated cameras. Particularly, for each trench with the underground pipeline releasing methane gas, the boundary of gas affected areas along the test trench can be clearly identified and quantified. Given the depth of gas source from the underground pipeline, determining the 3D volume estimate of the gas affected space is readily achievable. In real-world applications, the thermal images can assist in the determination of gas leakage source (depth) by comparing thermal images over time (after taking out the effect of seasonal temperature changes). But the spatial resolution of thermal-based technique is low. Different hyperspectral stress indicators exhibited a various degree of effectiveness in detecting the stress occurrence on tested grasses. The chlorophyll characterized indicator (MCARI) was the most sensitive index for stress detection though the 'red edge' related indicators (RER, NVDI, and mND705) also saw changes from different gas treatments. All of them fluctuated significantly from one trench to another. It is thus recommended that the gas-treated trenches be compared with their surrounding grasses (also more practical in applications) to demonstrate the induced stress on grasses in a qualitative measure.

The extensive imagery collected was also used to train a multilayered perceptron neural network and classify the plants with or without methane gas treatment. Based on the classification example, the proposed deep neural network can successfully classify the plant with an overall accuracy of 96.2%. The 'red edge' chlorophyll-featured bands were the most informative in terms of classification. In comparison with the control group with no gas treatment, the methane stressed plant displayed a lower intensity in 500-600 nm and a higher intensity in 600-720 nm (chlorophyll absorption band). This indication is also proven by the bio-chemical measurement of the plant pigments and therefore can be a reliable criterion for the identification of methane gas affected plants in practicable applications. The deep learning approach is applicable to detect any surface features noticeable to human eyes, such as mechanical damage and/or coating deterioration of above-ground pipelines. However, the dataset needed to train the deep learning algorithm may be difficult to obtain since the case of above-ground pipelines with gas leakage is rare and, more importantly, may not be accessible due to liability concerns from pipeline operators' perspectives.

Acronyms and abbreviations

AGL	Above Ground Level
ASD	Analytical Spectral Devices
ATP	Adenosine Triphosphate
CFD	Computational Fluid Dynamics
Chl	Chlorophyll
CRI	Carotenoid Reflectance Index
DE	Drought Exposure
DNN	Deep Learning Networks
DNs	Digital Numbers
ECe	Electrical Conductivity
EKF	Extended Karman Filter
EPA	Environmental Protection Agency
FN	False Negative
FOD	First-order Derivative
FOV	Field of View
FP	False Positive
HMC	Heavy Metal Contamination
HSI	Hyperspectral Stress Indicator
HVL	Highly Volatile Liquid
IMU	Inertial Measurement Unit
LDA	Linear Discriminant Analysis
LIDAR	Light Detection And Ranging
MLP	Multilayer Perceptron
mND705	Modified Normalized Difference 705
NDVI	Normalized Difference Vegetation Index
NIR	Near Infrared
PCA	Principal Component Analysis
PHMSA	Pipeline and Hazardous Materials Safety Administration
PRI	Photochemical Reflectance Index
PVC	Polyvinyl Chloride

QDA	Quadratic Discriminant Analysis
REG	Red Edge
ReLU	Rectified Linear Unit
RER	Red Edge Ratio
ROI	Region of Interest
ROS	Reactive Oxygen Species
ROS	Robotics Operating System
SHAP	Shapley Additive Explanations
SI	Salinity Impact
SNR	Signal-to-Noise Ratio
SNV	Standard Normal Variate
SOD	Second-order Derivative
STD	Standard Deviation
SWIR	Short-wave Infrared
TN	True Negative
TP	True Positive
UART	Universal Asynchronous Receiver-Transmitter
UAV	Unmanned Aerial Vehicle
VIS	Visible
VNIR	Visible and Near-infrared
WBI	Water Band Index

Table of Contents

List of Tables

List of Figures

I. Introduction

Pipelines in society function like blood vessels in human body, bringing humanity with life-sustained necessities, such as water or natural gas, and discharging human wastes such as sewage. They are the most favorable mode of transportation for gas and liquid in large quantity. Due to their capital investment, pipelines must be free from the risk of degradation that could result in environmental hazards and potential threats to life.

According to the 2021 PHMSA statistical data, the U.S. has approximately 2.9 million miles of pipelines for gas distribution, gas gathering, gas transmission and hazardous liquid transport, including plastic pipelines primarily in the gas distribution system. Less than 10% of the total mileages or 229,949 miles is for the distribution of liquid and highly volatile liquid (HVL) such as biofuel, CO_2, crude oil, HVL flammable toxic, and refined products (PHMSA, 2021). Between 2003 and 2022, over 12,781 pipeline incidents occurred, resulting in $10,816,193,735 property loss, 274 fatalities and 1120 injuries (PHMSA, 2022). These incidents were caused by natural forces (earth movement, wind gusts, heavy rains/floods, lightening), excavations from third parties or operators, operation negligence, material defects, and corrosion (Lu et al., 2020). For instance, traffic and surface loads can make buried pipes and joints overstressed, leading to pipeline leakages and bursts (Khulief et al., 2012). Destructive causes, pitting corrosion and water hammers can also lead to pipeline leakages (Sun, 2011; Lazhar et al., 2013).

The most important impact by pipeline leakage is on safety and environment which is PHMSA's mission to protect people and environment. In addition, when not detected and repaired in time, a leakage in pipeline would cause a sudden decrease in pressure (Silva et al., 1996), increase delivering time, reduce the flow rate of fluids, and thus result in product loss and other serious damage (Sandberg et al., 1988).

Despite rapid technology advances in recent years, the most widely used inspection technique in pipeline industry is still ground patrol, which relies heavily on inspectors' observation and experience. Each patrol covers facility inspections, nearby construction activity monitoring, and pipelines' rights-of-way maintenances. It takes place more frequently in heavily congested areas than other areas with periodic maintenances, including leak surveys and safety device inspections in order to minimize the risk of high-pressure pipelines. Such a patrol, however, is often difficult or even dangerous due to field conditions, potential risks, and natural hazards. Therefore, advanced software and hardware systems have recently been developed to analyze pipeline risks and maintenance needs in a data-driven approach.

Research and application efforts are under way to develop cost-effective approaches to enhance pipeline integrity, inspection, monitoring, and risk management. To this endeavor, several hardware-based methods were applied to ensure pipeline safety. First, an acoustic emission method can record the pipeline noise generated in the process of liquid or gas leakage. This method can be integrated into an intelligent pig that travels inside a pipeline during inspection (Furness and van Reet, 1998). Acoustic sensors have also been installed outside a pipeline for continuous monitoring (Brodetsky and Savic, 1993). Second, both active and passive optical methods have been applied in pipelines. Active methods include Light Detection And Ranging (LIDAR) systems, millimeter wave radar systems, and optical fibers. For example, an optical fiber can be used to detect leak location, leaked gas concentration, and third-party activities along the pipeline's rights of way (Frings and Walk, 2011). Passive methods include thermal imaging (Kroll et al., 2009), multi-spectral (or hyperspectral) imaging (Gittins and Marinelli, 1998; Noomen et al., 2003), and gas filter correlation radiometry (Banica et al., 2008), which does not require any external energy source. Third, electric cables are also used for pipeline monitoring, which give more sensitive responses but are unable to quantify leakages (USEPA, 2004). Fourth, soil monitoring involves inoculating a gas pipeline with tracer compounds (Lowry et al., 2002). This expensive and high-sensitivity approach has a very low false alarm rate but is not applicable for aboveground pipelines. Fifth and lastly, a vapor monitoring system can be used for leak detection by sampling hydrocarbon vapor in the vicinity of pipelines (Sperl, 1991; Ren and Pearton, 2016).

Software-based approaches are also used to extract critical information of a pipeline and its surrounding conditions from collected data. In this category, the most straightforward approach is the mass or volume balance leak detection based on the principle of mass conservation. An imbalance between the input and output gas mass or volume is an indication of a leak (Liou, 1996; Parry et al., 1992). Following the similar concept, a real-time transient model with a sensor array is developed (Verde, 2001; Verde and Visairo, 2001). Statistical approach is also used to analyze data (Postaire et al, 1993), although it is less effective to estimate the volume of leakage. Lastly, signal processing techniques are used to analyze acquired data, which typically includes four steps of pre-processing, processing, feature extraction and classification (Jadin and Ghazali, 2014).

II. Objectives and Scope of Work

The overarching goal of this study is to enhance pipeline safety by enabling a routine and maintenance inspection of pipelines for critical data collection, processing, and application towards condition and risk assessments for pipeline operators. This goal will be achieved by developing an integrated Unmanned Aerial System (UAS) of infrared and hyperspectral cameras with signal processing and data analytics. This study aims to:

1. Develop and integrate a robust and stable, semi- or fully automated UAS with multiple sensors for multi-purpose pipeline safety data collection,

2. Explore and develop novel signal and image processing techniques for data analytics and condition classification, and

3. Evaluate and validate field performance of the integrated UAS for pipeline safety inspection.

These objectives will be achieved through analytical, numerical, and experimental investigations in three tasks:

1. Design and prototype the UAS for the collection of cohesive types of images from visible light, infrared, and hyperspectral cameras.
2. Develop and validate imagery and spectral processing techniques for two-dimensional (2D) image classification of stress conditions and three-dimensional (3D) object establishment for volume estimates.
3. Develop a deep learning neural network for the assessment of pipeline and ground surface conditions.

Note that the overall goal, objectives, and scope of this project are the same as described in the original proposal. Upon approval by the PHMSA personnel, however, some methods were modified to better achieve the goal and objectives of this project during the COVID-19 pandemic. For example, ¼-scale soil tests were originally proposed to be carried out in laboratory and the technology developed would be validated at one pipeline site with a company. Unfortunately, the period of this project was right in the middle of COVID-19. It would be impractical for the research team to contact the company and travel to the pipeline site to conduct research. Rather than delaying tasks and waiting till the COVID-19 was over, semi-controllable field tests were conducted in Rolla, Missouri, instead of fully controllable laboratory tests and uncontrollable field tests at a pipeline site. In doing so, both laboratory work and field work were addressed in a semi-controllable test setting. It turned out that this change in method proved effective. With full access to the open field and full control on test parameters, the research team accomplished and learned a lot more than they would have from an existing pipeline site since the research team access would otherwise be restrained due to security, safety, and liability.

III. Task 1-Design and prototype the UAS for the collection of cohesive types of images from visible light, infrared, and hyperspectral cameras

1.Preliminary design of the UAS

1.1 Requirement analysis and selection of airframe and sensors

A Duo Pro R640 camera (FLIR), as shown in Figure 1.1(a), and a Nano-HyperspecVNIR hyperspectral camera (Headwall), as shown in Figure 1.1(b), will be potentially integrated into an UAS that is installed on a custom-designed hexacopter, as illustrated in Figure 1.1(c). The Duo Pro R640 camera integrates a visible lens and an infrared lens arranged in parallel. The infrared lens can be used to take a thermographic image based on thermal radiation, and the visible lens is for a photographic image based on visible light reflection. The infrared camera has a measurement accuracy of ±5 °C or 5% of readings between -25°C and +135°C, and a thermal sensor resolution of 640 × 512 in space. The hyperspectral camera equips conventional spectroscopy with the capability of spatial/spectral information acquisition based on light reflection from a surface, greatly enhancing abnormality detection abilities and extending application scopes. The hyperspectral camera has 640 spatial pixels along a rectangular slit, perpendicular to the scanning direction during flight, and 270 spectral bands in 400 nm – 1000 nm. Unlike remote sensing via satellites, rapid improvements in camera resolution and stabilizer can further enhance video clarity and details particularly from close views obtained via a UAS.

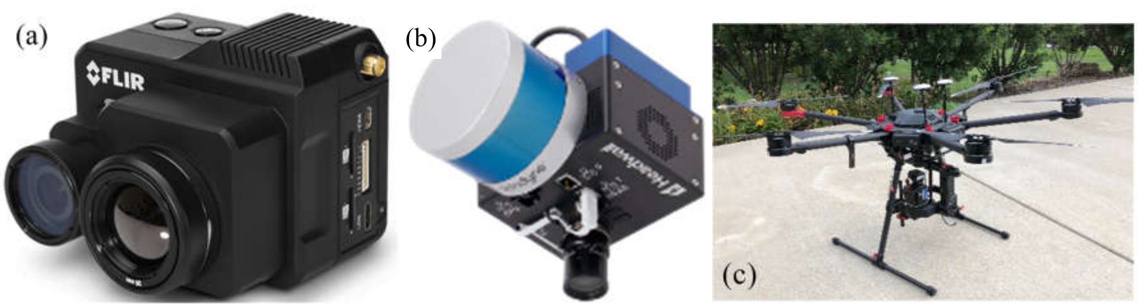

Figure 1.1 Key components in the proposed UAS for pipeline inspection: (a) dual-sensor visible light and infrared camera, (b) Nano-Hyperspec hyperspectral camera, and (c) hexacopter equipped with a hyperspectral camera

1.2 Aerodynamics and flight dynamics study

In an anticipation to integrate the sensors in a drone, a finite element model of the hexacopter started to be established. One of the four blades in the hexacopter was scanned using a 3D laser scanner (NextEngine 3D Scanner Ultra HD), as presented in Figure 1.2(a). Blades can exert a profound impact in the aerodynamics when in use. Point clouds were pulled into the Solidworks software and cleansed for visualization as illustrated in Figure 1.2(b). A mock test of hexacopter flying was also simulated to examine the stability.

In order to analyze the relationship between flight behavior and the system properties, the scanned propeller model was imported into Solidworks for CFD (Computational Fluid Dynamics) analysis. However, the computing time and the error increased dramatically when the UAV model and the environment model gets more and more complex. A more feasible model for flight analysis is a simplified aerodynamic model specifically for quadrotor aircrafts. Thesis (Bouabdallah, 2007) gave a summary on the flight dynamic of quadrotor from mathematical equations to experiments with a small UAV. A more practical way to a parametric study with the quadrotor would be using a flight simulator such as jMAVSim with PX4 as shown in Figure 1.2(d).

(a)

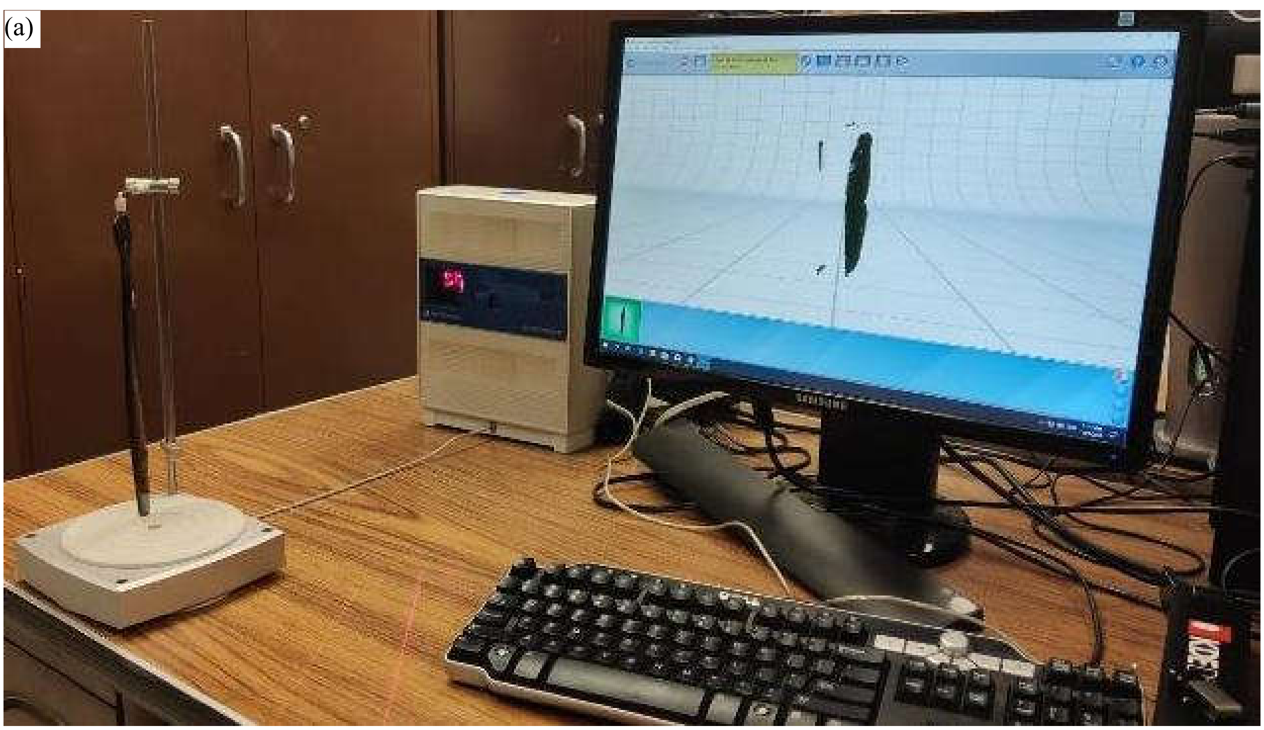

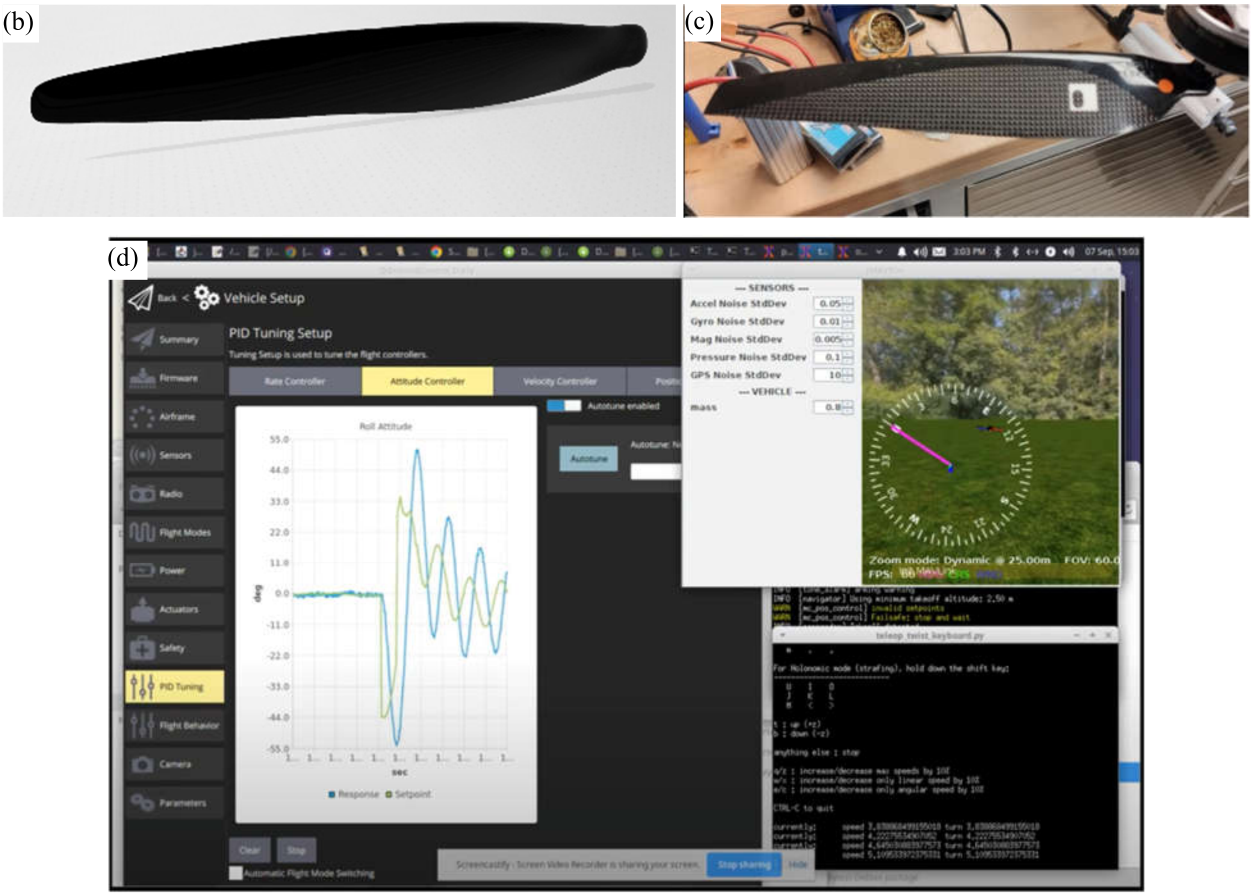

Figure 1.2 Modeling of a blade of the hexacopter: (a) raw data taken from the 3D scanner, (b) clean model, (c) blade prototype, and (d) UAV parameter study with jMAVSim and PX4

1.3 Non-GPS navigation based on visual odometry

A design of the integrated UAS with non-GPS navigation is proposed and tested in lab. Figure 1.3 shows the test quadcopter. A Jetson TX2 onboard computer in the black case is mounted on top of the drone. The Jetson TX2 is a powerful embedded computer with GPU inside. It has several interfaces that can connect with different types of sensors. A ZED 2 depth camera is mounted on the front of the drone to work as a visual odometry and data collector. The visual odometry is working as a supplement when the drone goes to some places such as buildings or tunnels where GPS signals are weak. The ZED 2 camera can detect objects such as humans and cars and keep a safe distance from other objects. The two antennas on the Jetson case are for Wi-Fi and Bluetooth communications. Wi-Fi is used to connect the Jetson TX2 to a ground control station. The black 3D printed frame around each motor is going to be used to mount safety carbon fibers to protect the propellers from hitting other objects.

Figure 1.3 Test quadcopter with an onboard computer

Figure 1.4 presents a signal flow diagram of the UAS. The ZED 2 camera is connected to the Jetson TX2 via a USB 3.0 cable. This high-speed connection can transfer real time image data up to 720 p at 60 Hz. This high updating rate helps compensate position drifts caused by disturbances such as wind. The ZED SDK does intensive computations with an algorithm, making use of both GPU and CPU to track the drone's position. This positional tracking information is imported to a Robotics Operating System (ROS). The ROS takes care of format and coordinate conversion based on the position where the ZED 2 camera is mounted. Eventually, a Universal Asynchronous Receiver-Transmitter (UART) communication cable is used to transmit the local position estimation information and confidence level to the autopilot, which is called ArduCopter. An Extended Karman Filter (EKF) data fusion algorithm is used to fuse the local positional visual information with data from the Inertial Measurement Unit (IMU) on ArduCopter. This whole process solves the non-GPS navigation problem.

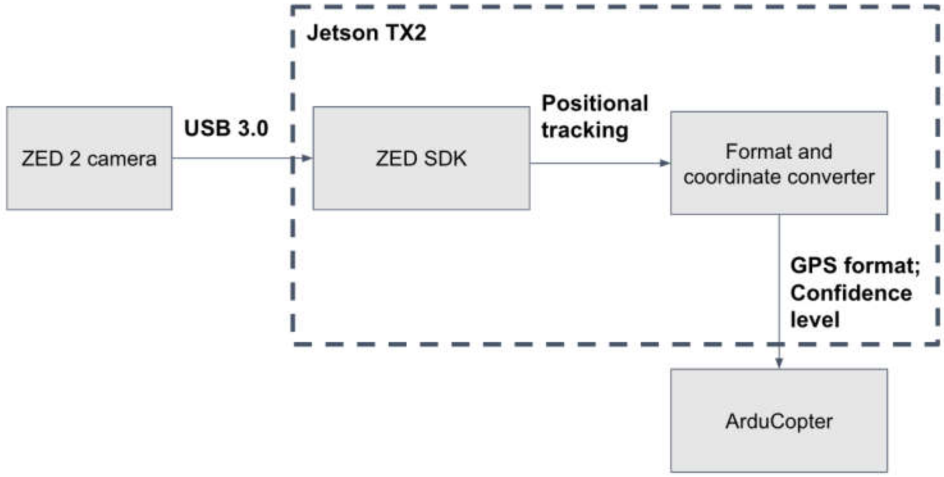

Figure 1.4 Signal flow diagram of the UAS system

2. Testing of the designed drone platform

2.1 Small drone net construction

To perform the necessary drone test in the laboratory before doing a field test, a test platform was set up in laboratory, as shown in Figure 1.5. PVC pipes (2” in diameter) were used to build a 4.3 m × 3.1 m × 2.2 m frame. Bungee balls were used to hang the drone net to the frame. Colorful foam blocks were used to add more visual features and protect the drone from damage when landing.

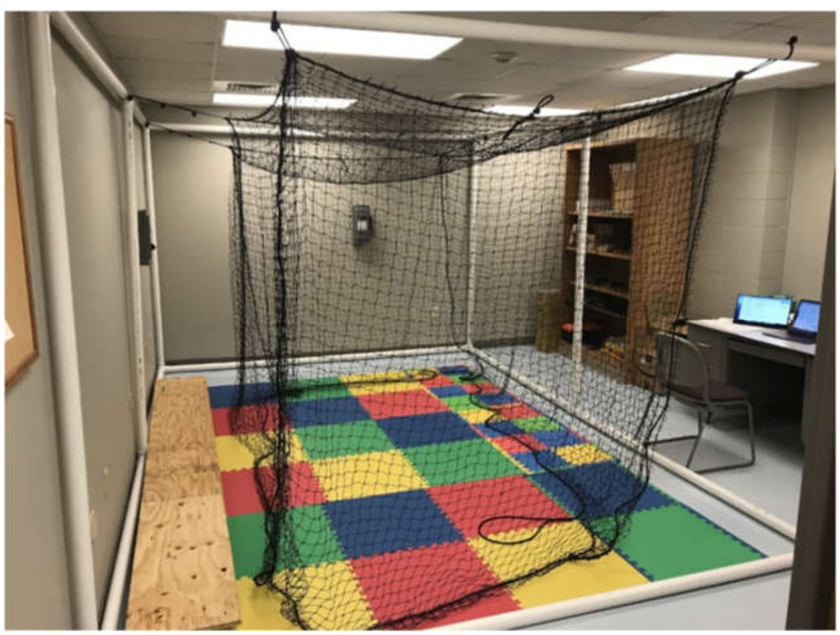

Figure 1.5 Indoor drone cage

2.2 Flight stability analysis for indoor and outdoor environment

Drone flight stability is critical to data quality. It is noted that the test quadrotor performs better outside than inside the drone net. To investigate the drone flying history in the view of stability, stability log data in each degree of freedom is displayed in Figure 1.6. The stability of the drone at each degree of freedom is illustrated in Figure 1.7. As the comparison results demonstrate, indoor flying test yields more fluctuations in the degrees of X, roll and pitch, which is approximately doubled in all three scenarios. For Z axis, the indoor fluctuations are about 25% of those outdoor. It is also observed that the stability in Y axis is comparable with indoor and outdoor environments. Part of the main reason for some modes of drone operation inside the drone net was the crowd space. The stability of the drone was affected by the reflection wind from the walls surrounding the net.

To improve the flight stability of indoor tests, a larger drone net measuring 11 m × 7.65 m × 6.12 m was built up in the HyPoint facility of Missouri University of Science and Technology (Missouri S&T) to reduce the air flow influence produced by adjacent walls. Figure 1.8 shows the large drone net for further drone flying tests.

Figure 1.6 Position fluctuations (in meter) of the drone when flying indoor and outdoor

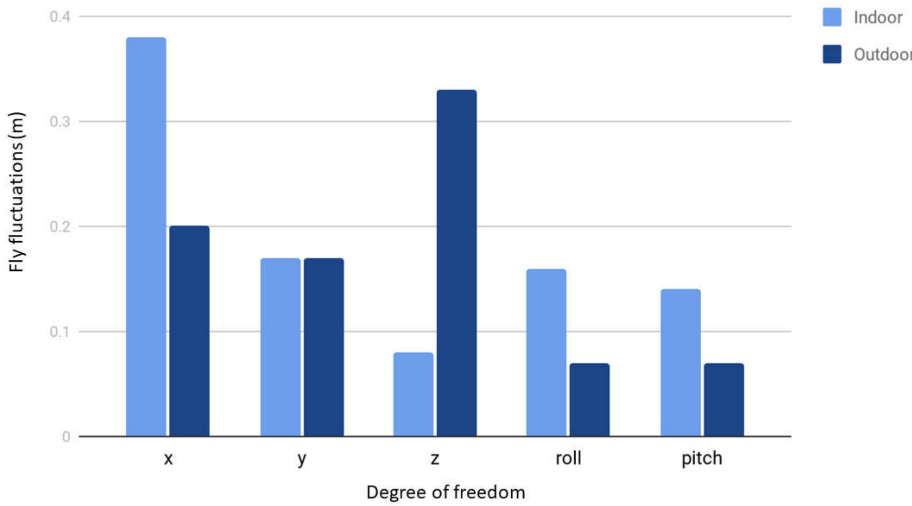

Figure 1.7 Indoor vs. outdoor flight stability using the fluctuation of drone positions in each degree of freedom

Figure 1.8 A large drone net in Missouri S&T's HyPoint facility

2.3 Platform based on the DJI M600 Pro

This platform as shown in Figure 1.9 was developed based on the DJI M600 Pro, which is a heavy, large size drone with 6 batteries. It measures 1,668 mm × 1,518 mm × 759 mm when propellers, frame arms, and GPS mount are in operation setting. Its total weight including six TB47S batteries is 9.5 kg. According to DJI, the flight time of the drone is 40 min with no payload and 18 min with 5.5 kg payload. The flight control system employs a DJI's own A3 flight controller.

Figure 1.9 DJI M600 Pro UAV with LiDAR, thermal camera and hyperspectral camera

Figure 1.10 shows the three payload sensors that are mounted on the DJI M600 Pro UAV. From left to right are a LiDAR scanner, a hyperspectral camera, and an infrared camera. The 16-channel Velodyne Puck LITE was selected to provide a 30° vertical field of view to deliver accurate real-time 3D data. Those data can be used for pipeline detection and 3D reconstruction. LiDAR Tools can collect high resolution LiDAR data and post-process point clouds output. The Nano-Hyperspec VNIR (400-1000 nm) was selected to have 270 spectral bands with a spectral resolution of 2.22 nm. In the direction of line scanning, there are 640 pixels in space. This DJI M600 Pro UAV is also equipped with a FLIR Duo Pro R camera whose resolution is 640 × 512. The field of view of this infrared camera is 45°, which enables a data collection frequency of 9 Hz.

Figure 1.10 Three payload sensors on the DJI M600 Pro UAS

2.3.1 Field of View calculation

The LiDAR scanner and the infrared camera have a field of view (FOV) of 30° and 45°, respectively. The hyperspectral camera has an initial slit image. Its FOV can be identified from characterization tests. During the characterization tests, the ground surface can be marked with a measurement tape that is deployed perpendicular to the flight direction. For example, with a lens focal length of 12 mm in our hyperspectral camera, each flight at an above ground level (AGL) of 15 m covers a ground area of 5.92 m in swath width, corresponding to a pixel size of 5920/640 = 9.25 mm. Considering 40 % overlapping in the covered ground area, the line spacing between two flight passes is 0.4×5.92 = 3.55 m. Figure 1.11 illustrates the relation between the camera position and the ground coverage. Point A represents the location of an unmanned aerial vehicle (UAV), and Line BC is what the hyperspectral camera can capture at one frame. In this example characterization test, AD = 15 m and BC = 5.92 m. Thus, FOV = 2α = 2×arctan(0.5×BC/AD) ≈ 2×arctan (0.5×5.92/15) ≈ 22.33°.

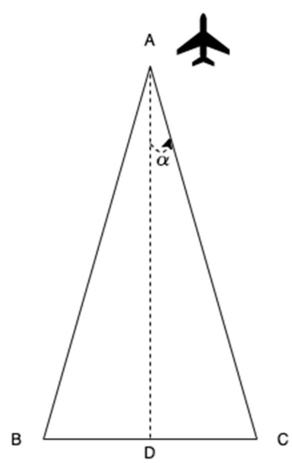

Figure 1.11 Field-of-view calculation

With 9 ms in exposure time, the required speed of the UAV can be determined from PixelSize = Exposure Time × AircraftSpeed, giving 9.25/9 = 1.03 m/s. Thus, FOV can also be determined from AircraftSpeed = AGL×FOV×FrameRate/SpatialBand, which is equal to 1.03×640/15/111×180/π ≈ 22.68°. The difference in FOV likely represents the effect of optical aberration, which is the bending of spectral lines across the spatial axis due to the change of dispersion angle at a field position. In other words, the theoretical value in covered ground area in Figure 1.11 may be estimated by 5.92 × tan(22.68/2)/tan(22.33/2) = 6.02 m. Table 1.1 summaries the optimal setting of the camera and its FOV identification from the calculator provided by Headwall Photonics, Inc.

Table 1.1 Camera setting and field-of-view calculator from Headwall Photonics, Inc.

Field-of-View Calculator

Determine optimal settings by entering exposure time or aircraft speed

Navigate to each of three tabs to select your lens and enter your Altitude (AGL in m), Aircraft Speed (m/s), Overlap (%), Exposure Time (ms), Flight Time (min) and Field Width (m).

Nano Exposure Time Input | Nano Aircraft Speed Input | SWIR Aircraft Speed Input

Headwall Photonics: Nano-Hyperspec® VNIR Airborne Calculator - Exposure Time Input								Inputs
Lens FL (mm)	Altitude (AGL) (m)	Overlap (%)	Exposure time (ms)	Spatial Pixel (mm)	Swath Width (m)	Line Spacing (m)	Frame Rate (Hz)	Aircraft Speed (m/s)
12	15	40%	9	9.25	5.92	3.55	111	1.03

2.3.2 UAV calibration and flight test without payload sensors

After the GPS and compass were properly set up, the compass was calibrated according to the instructions from the APP as the drone was rotated 360° in a horizontal plane as illustrated in Figure 1.12. After the compass calibration, the overall status of the drone became normal according to the APP. To test cameras and train remote pilots, we removed the LiDAR scanner, infrared camera, and hyperspectral camera and conducted flight tests without the payload sensors to prevent potential damage of the sensors, as shown in Figure 1.13.

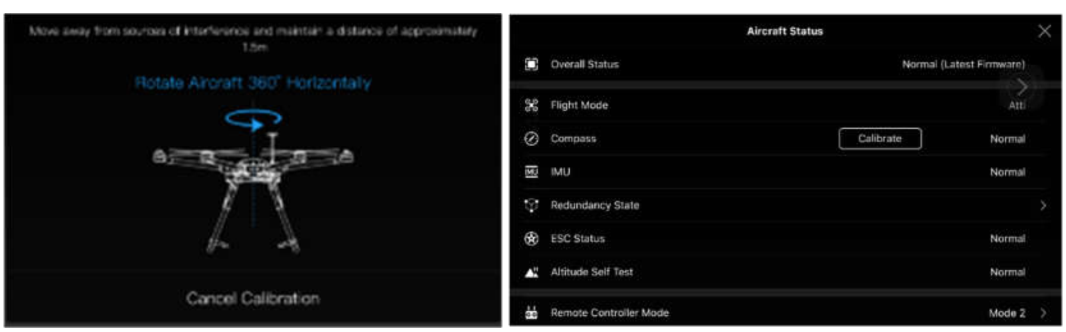

Figure 1.12 DJI M600 Pro UAV compass calibration

Figure 1.13 DJI M600 Pro UAV ready for flight test and training without payload sensors

2.3.3 Flight route planning using UGCS software

Figure 1.14 shows a flight route (green color) designed in the UgCS software (https://www.ugcs.com/). UgCS allows one to set up the parameters for drone flying, such as route design, flight height, and flying velocity. It also works as a platform to connect the drone and automatically control the aerial behavior. The green-bluish color in Figure 1.14 defines the perimeter to trigger the Nanospec hyperspectral sensor. The first few turns of the drone before entering the area of interest are designed for filter-tuning, which is beneficial to improve the drone's GPS. Figure 1.15 shows the drone that flies according to the designed flight path. The drone is directed as designed unless a manual operation is needed in presence of some unexpected scenarios like the disconnection of the drone control panel. We practiced how to operate the drone manually when the drone encounters any obstacle along the automated flight path. If the manual intervention can reconcile the issue in a short period of time, the drone can return to the automatic control mode and complete the planed path mission eventually. Otherwise, the drone may go beyond the control domain and can no longer connect to the ground control center. Figure 1.16 shows an image captured by the drone looking straight down to the test site with tarps and markers for calibration purposes.

Figure 1.14 Drone flight plan in the UGCS software

Figure 1.15 Automated flight of the DJI M600 Pro UAV

IV. Task 2 Develop and validate imagery and spectral processing techniques for two-dimensional (2D) image classification of stress conditions

1. Experimental Program

1.1 Greenhouse test setup

Greenhouse tests were conducted in the Hypoint Laboratory (37.955376 N, 91.771681W) at Missouri University of Science and Technology. As shown in Figure 2.1, one grass (karl foerster grass abbreviated as 'Grass') and two shrubs (southern sunshine 'Ligustrum sinense' abbreviated as 'South' and gem box 'inkberry holly' abbreviated as 'Gem') were selected to emulate gas leakage effects across plant species. All plants were fully grown to ensure that their heights do not change appreciably in the study period, having minimal influence on subsequent hyperspectral scanning. The plants selected were perennial to overcome aging deterioration. The plants were treated with natural gas and three other stressors: salinity impact (SI), heavy metal contamination (HMC), and drought exposure (DE). The other stressors served as distraction sets for gas leakage detection (Lichtenthaler, 1996; Smirnoff, 1998; Ahanger et al., 2017). For comparison, plants cultivated under optimal conditions were used as a control reference, which is referred to as non-stressed scenario. For each stress treatment condition including the non-stressed scenario, three tests were repeated. A total of 45 pots of plants (3 replicas×5 treatments×3 species) were prepared for the greenhouse tests.

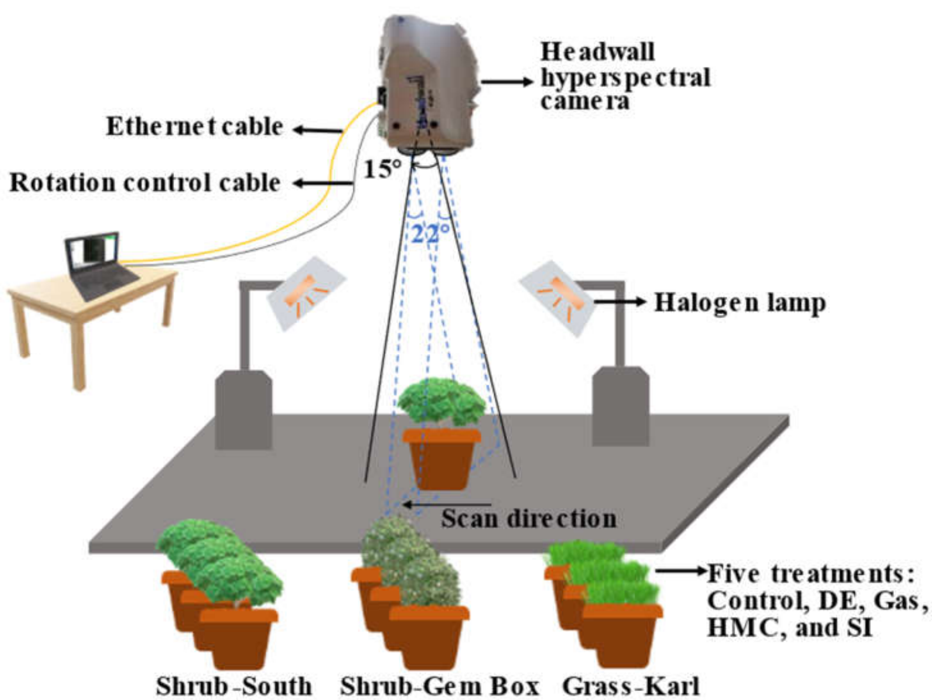

Figure 2.1 Test setup of hyperspectral imaging

Before any treatment, all plants were placed in the greenhouse for an acclimation period of 15 days to ensure they are adapted to the greenhouse environment. For gas treatments, plants were transplanted to 25-liter standard cylinder pots for easy distribution of methane gas. A percolated gas distributor in cross shape was installed at the bottom of each pot for methane application. The four ends of the cross were alternated clockwise to ensure that methane uniformly diffuses into the soil. Ultra-high purity grade methane from Airgas (Airgas Inc, Pennsylvania, USA) was used as a stress medium to stimulate the plants. The flow rate of the methane was regulated to 5 liters/hour over 10 hours a day. The gas was delivered through a transparent vinyl (D = 0.1875 cm). For Saline treatments, the soil was remodeled with $NaCl$ and $CaCl_2$ in 2:1 mol ratio to realize a moderate salinity for each species of plants (Provin and Pitt, 2001). Here, sodium and calcium chloride salts were used because of their abundance in nature. The moderate salinity was quantified by the soil saturated paste electrical conductivity (*ECe*) (Lara et al., 2016). In reference to saline resistances of different species, *ECe* was finally set to 6 dS/m, 8 dS/m, and 8 dS/m for Grass, South, and Gem, respectively (Karberg et al., 2015; Joseph et al., 2016). Before salinization, the original *ECe* of soil in each pot of plant was measured and the amount of salt needed was estimated. For HMC treatments, the composition of heavy metal elements and their concentration in soil were referred to the U.S. Department of Agriculture (USDA) regulatory limits as given in Table 2.1. In this study, the five most common heavy metal elements are considered: chromium, copper, zinc, nickel, and arsenic. As the metal salts are highly soluble in water, heavy metal salts are diluted into irrigation water and sprayed on the soil of potted plants in three batches to prevent overflowing (Lassalle et al., 2018). For DE treatments, irrigation water was reduced to half of the water intake as instructed on plant tags (Bellante et al., 2014; Wang et al., 2018). After each treatment, plants were transferred back to the greenhouse to mark the start of a stress cycle. For the reference group, plants were watered as instructed without any additional treatment on the soil to create a stress-free environment.

Table 2.1 USDA regulatory limits of heavy metal applied to soil developed by the U.S. Environmental Protection Agency (EPA)

Heavy metal salt	As	Cd	Cr	Cu	Pb	Hg	Ni	Se	Zn
Maximum (ppm)	75	85	3000	4300	420	840	75	100	7500

Between August 16 and December 18, 2020, all the plants were cultivated in the greenhouse with a temperature of around 25 ℃ and a relative humidity of 70%. TA series of LED lights with a constant 378 μmol·m^2/s photosynthetically active light intensity were uniformly distributed on the roof of the greenhouse to create a homogeneous radiation on each plant as it was in a normal transpiration system. A photoperiod of 14 hours of light and 10 hours of darkness was maintained throughout the greenhouse tests. In addition, the ventilation rate of the greenhouse was set to 50 liters/min to achieve a good air circulation for the plants in the greenhouse and maintain a constant temperature.

1.2 Hyperspectral image collection

The stress effects on the treated plants were characterized by hyperspectral reflectance, also known as spectral signature or spectral curve. A 'push broom' hyperspectral imaging platform built for this test was composed of four parts: imager, spectrometer, illumination source, and movement control, as shown in Figure 2.1. The Headwall dual-lens imager (Headwall Photonics, Inc., Bolton, MA, USA) that covers a full spectral range from 400 nm to 2500 nm was used to collect hyperspectral images. The full spectral range can be divided into two regions: VNIR (400-1000 nm) and SWIR (900-2500 nm). The VNIR range has 271 bands with 2.22 nm spectral resolution while the SWIR range has 267 bands at a 6 nm wavelength interval. Therefore, the full spectrum (400-2400 nm) used in this project has approximately 489 sampling bands. The external illumination was provided by two 300 W full-spectrum tungsten halogen lamps (Ushio Lighting Inc., Cypress, CA) that was arranged in parallel with the plant pots to produce a homogeneous radiation on the canopy of plants. Under the constant light exposure, the exposure time of the hyperspectral camera was set to 40 ms at a framing rate of 45 ms. The field of view of the camera on the side of two lens was 22°. In the plane of the dual lens, the hyperspectral camera can rotate 15° to cover the area to be scanned during tests. The speed of the hyperspectral camera was adjusted to fit the imaging setup to ensure no pixel distortion so that the object in the pixel was neither compressed nor extended in the movement direction. The camera parameter setup and speed control were finished in the software Hyperspec III (Headwall Photonics, Inc., Bolton, MA, USA).

To collect hyperspectral images, the plant canopy was set to be 1.2 m down below the imager. For each scanning, a screening line contains 640 pixels within the FOV of the imager and the obtained image has 640×1208 pixels. The spatial resolution of the pixel is 0.78 mm. Before the plant canopy was scanned, a gray mat was placed underneath each pot within the view of the camera to reduce the reflection from the background, lowering the risk of shadowing in the hyperspectral image. All the plants were scanned every five days at completion of the acclimation period.

1.3 Radiometric calibration

Hyperspectral reflectance extracted from the plant leave reflects physical, morphological, and biochemical status of the leaf surface (Lowe et al., 2017). The quality of image data is related to the imager detector properties such as lens, sensor, grating and filter. Raw images are subjected to radiometric calibration to reduce the influence of variability from the sensor (Thorp et al., 2017, Paulus and Mahlein, 2020). Raw digital numbers (DNs) captured by the detector are mapped to radiance through a calibration coefficient for each wavelength. Thus, the spectral power flux on the projected area can be plotted as a function of wavelength, creating a radiance fingerprint. When exposed to a constant source, the radiance from plant canopies can be converted to the hyperspectral reflectance to facilitate the identification and comparison between different scans. The radiance-to-reflectance conversion is done by collecting dark and white references (Kale et al., 2017; Wang et al., 2018; Asaari et al., 2018; Elvanidi et al., 2018; Moghimi et al., 2018). Prior to each scan, the camera when capped captures an internal dark current as the dark reference. The white reference is acquired by a standard 25.4 cm square Labsphere Spectralon ® (Labsphere, Inc., North Sutton, NH, USA) made of barium sulfate, which can reflect 99.7% light.

All pixels on the image are subjected to radiometric calibration by subtracting the dark reference and normalized by the white reference before any feature extraction from hyperspectral reflectance curves. All the conversion and correction are done in SpectraView software (Headwall Photonics, Inc., Bolton, MA, USA). The raw reflectance is normalized as shown in Eq. 2.1 to range from 0 to 1. This transformation makes the spectral signatures between scans comparable (Mahesh et al., 2008; Paulus and Mahlein, 2020).

$$I_r = \frac{R-D}{W-D} \tag{2.1}$$

where R and I_r are the raw and normalized reflectance intensities from a target pixel; D and W are its corresponding dark current and white reference, respectively.

1.4 Analysis Methods for Stressor Classification

1.4.1 Optimization of raw reflectance

The spectral curves retrieved from plants are typically not smooth especially from a single pixel (Foody, 2002). The Savitzky-Golay smoothing technique provides a moving average of n adjacent bands and fits the averaged points with a m-degree polynomial function. Another smoothing strategy to increase the signal-to-noise ratio (SNR) is to put l neighbor bands into one bin though reducing the spectral resolution (Sankaran et al., 2011; Paulus and Mahlein, 2020). Furthermore, a spectral curve of a spot is extracted from binning pixels in the region of interest (ROI) instead of picking an independent pixel. Figure 2.2 compares the two ways of data extraction: single pixel and spatial binning. It can be seen from Figure 2.2 that the noise is suppressed along the spectrum especially in the VNIR and the SNR is almost doubled by the spatial binning. The above raw hyperspectral reflectance curve extraction is achieved in the classification module of SpectraView software.

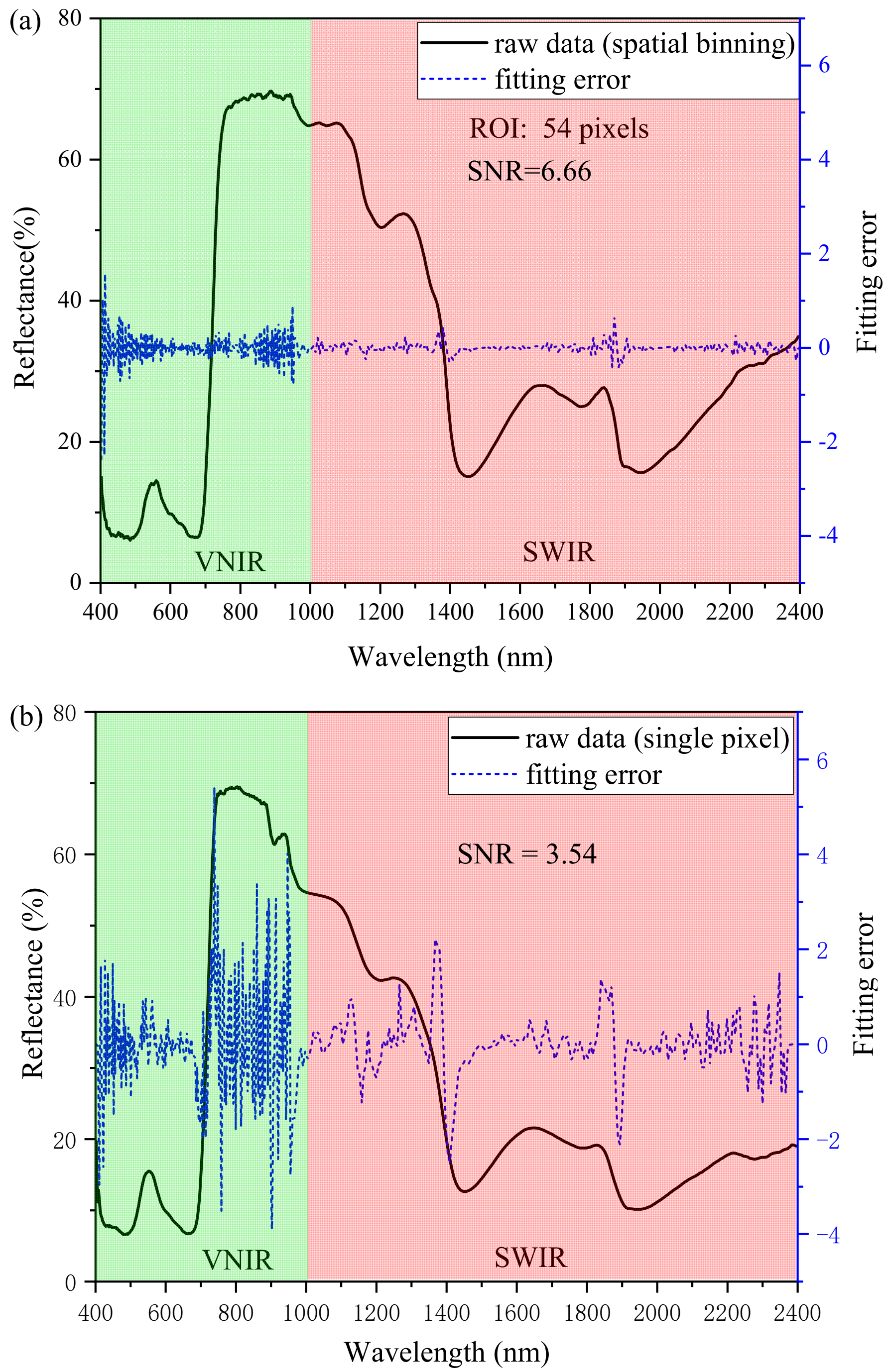

Figure 2.2 SNR of hyperspectral reflectance extracted from two strategies: (a) spatial binning of multiple pixels, and (b) spectral averaging at a single pixel

In addition, the canopy leaf inclination and thus distance to the imager detector affect the intensity of reflectance (Behmann et al., 2018; Asaari et al., 2018). Such variations can lead to locally higher reflection in some pixels and thus neutralize an artefact unintentionally (Thorp et al., 2017). To compensate for the above multiplicative factors, the standard normal variate (SNV) is introduced to normalize the spectra by removing their mean and dividing their standard deviation as indicated in Eq. 2.2 (Lara et al., 2016; Lassalle et al., 2018; Asaari et al., 2018).

$$C_{SNV} = \frac{R - mean(R)}{STDEV(R)} \tag{2.2}$$

where *R* and *C* denote the spectral curve before and after SNV processing; *Mean* and *STD* are the mean value and standard deviation of a spectral curve.

Mathematically, SNV can be viewed to rescale the variables such as leaf inclination and light scattering into a standard form. This transformation retains every minor feature of the original spectral signature, thus making the reflectance curves from pixels in the ROI comparable. After the SNV, the raw hyperspectral reflectance was differentiated with respect to wavelength to further reduce the effect of multiplicative variations (Sankaran et al., 2011). More importantly, derivative analysis augments absorption features that are masked by the noise (Tsai and Philpot, 1998; Wang et al., 2010; Roy, 2015; Thorp et al., 2017). In this study, both the first order derivative (FOD) and the second order derivative (SOD) of each hyperspectral reflectance spectrum are calculated by Savitzky-Golay filtering with a window of 9 bands and a polynomial order of 2. The Savitzky-Golay filtering can simultaneously smooth and differentiate the spectra following a least square optimization (Tsai and Philpot, 1998; Roy, 2015). All data transformations are done by using the Unscrambler X software.

1.4.2 Spectrum range for effective stress discrimination

Hyperspectral imaging collects spectral information across wavelengths continuously from 400 nm to 2400 nm; it can be divided into VIS, NIR and SWIR ranges (Manley et al., 2019). A spectral signature contains features, macro patterns, and subtle variations that are yielded by biochemical components within a circular area of a leaf during measurement. A certain portion of the electromagnetic spectrum, VIS, NIR or SWIR, is strongly correlated with the foliar biochemistry (Blackburn et al., 2007; Tarnavsky et al., 2008; Yu et al., 2013; Behmann et al., 2014). In the VIS range, photosynthesis pigments, especially chlorophyll, is characterized by the light absorption at wavelength 680 nm (Thenkabail et al., 2013). Carotenoid as an accessory photosynthesis pigment plays a dual role in both photosynthesis and photoprotection processes, which harvests photos within a green range of 530 nm (Thenkabail et al., 2013; Havaux, 2014). It signals stress occurrence and reacts with the stress induced reactive oxygen species (ROS), leading to a mitigation of stress conditions (Shah et al., 2017). In the NIR range, the high reflectance is dominated by the cellular light scattering through mesophyll. In the SWIR range, the dry biomass, lignin and cellulose, protein, and moisture are characterized (Behmann et al., 2014).

The gas leakage and natural stressors affect ground vegetations in different ways. Gas leakage replaces the oxygen in vegetation roots with methane, obtruding the oxygen assimilation and thus increasing chlorophyll (Smith et al., 2004; Noomen et al., 2008). In contrast, HMC stresses plants by making the chlorophyll malfunctional as the HMC cations displace centered magnesium (Mg^{2+}) (Slonecker, 2018; Mirzaei et al., 2019). Water deficit as a result of DE causes an early leaf senescence that terminates the development of leaf by decomposing pigments (mainly chlorophyll) and relocating the nutrient mass (Behmann et al., 2014; Asaari et al., 2018). The alternation of pigmentations featured by VIS spectroscopy can regulate the cell wall activities featured by NIR spectroscopy. However, it is unclear whether biomass and protein featured by SWIR spectroscopy are related to the presence of early stress though their effect on long-term stress exposure is evidenced. As such, three ranges of spectra, full, VNIR (VIS+NIR), and SWIR, are tested and compared to determine the most effective spectral range in presence of stress.

1.4.3 Multivariate analysis

Each hyperspectral reflectance spectrum contains 489 sampling wavelengths. The features manifested within a close range of wavelengths are sometimes interrelated since the chemical stretches interact with photons that have nearly tantamount energy. The reflectance curve also exhibits variations in the VNIR and SWIR range in terms of the importance of various stressors, which camouflages the distinction of each treatment and complicates the stress discrimination. To account for the above factors, multivariate analysis proved effective to successfully distinguish stress treatments (Mahesh et al., 2008; Sankaran et al., 2011; Song et al., 2011; Lowe et al., 2017; Lassalle et al., 2018).

1.4.3.1 Principal component analysis (PCA)

A single spectral curve can be expressed into a function of wavelength as displayed in Eq. 2.3,

$$H(w_1, w_2, \cdots w_p) = f_{w1}(w_1, w_2, \cdots w_p) + f_{w2}(w_1, w_2, \cdots w_p) + \cdots + f_{wp}(w_1, w_2, \cdots w_p) \quad (2.3)$$

where w_i represents the wavelength w at the i^{th} band out of a total number of samplings p in the spectral range of interest (e.g., 489 samplings of the full spectra); *H* denotes the spectral curve function; f_{wi} is the integration of contributions from p number of wavelengths centered at the i^{th} wavelength (i = 1, 2, ..., p). Multicollinearity at adjacent wavelengths often influences the interpretation of spectral curve features due to high dimensionality and entangled correlation. For the construction of a discrimination model, all features of the hyperspectral reflectance curve from each stress treatment can be expressed into $X_s = [H_0, H_1, \cdots, H_{s-1}]$, where *s* is the number of observations. H_0 is a collection of the p terms in Eq. (2.3) and written in vector form. To reduce the dimensionality of hyperspectral data, PCA is used to analyze the original and transformed spectral curves. PCA projects the p-dimensional data points to different orthogonal axes by maximizing the variance in each direction. The PCA process makes the information along principal component (PC) axes independent. The projection space is defined by the eigenvectors that are derived from matrix X_s. The eigenvalues of the directions associated with the eigenvectors can be computed from Eq. 2.4 (Uddin, 2015). The top eigenvalues are the indicators of the explanatory variance of the original data in the corresponding PC directions.

$$E^{-1}CE = \lambda \tag{2.4}$$

where *C* denotes the covariance matrix of the X; *E* is a matrix that represents a collection of the computed eigenvectors; and λ is a matrix including the eigenvalues in diagonal direction. The eigenvalues are displayed in a descending order and a higher eigenvalue means more contribution of that PC to representing the original data. The number of PCs, *n*, to use for further model construction is determined by the 95% accumulative explained variance of the raw reflectance data by the first *n* PCs. While increasing *n* unproportionally can cover more radiance, an excessive number of PCs is likely to cause a dimensionality havoc or Hughes phenomenon (Alonso et al., 2011). After the PCA, the features of the X_s can be remodeled as F with the *n* eigenvectors.

$$F = \mathrm{Xs}E_n \tag{2.5}$$

1.4.3.2 Linear/quadratic discriminant analysis (LDA/QDA)

The optimized and transformed raw reflectance data with reduced dimensions will be used to identify or distinguish various treatments among three species of plants. LDA/QDA groups different stressors by modelling the difference among samples through the feature vectors *F* from PCA analysis. It is performed by projecting features to hyperplanes that maximizes the distances between categories and minimizes the variation within each category. QDA classifies samples by maximizing the ratio between C_w (within-group covariance) and C_b (between-group covariance) (Uddin, 2015). Once the maximum ratio is located, the optimal differentiation space S_{QDA} is expressed into

$$S_{QDA} = \arg\ max_{QDA} \frac{|S^T C_b S|}{|S^T C_w S|} \tag{2.6}$$

where S_{QDA} represents the direction in which the groups are sectioned optimally in feature data space F. LDA is a simplified form (special case) of QDA in terms of discrimination strategy. LDA groups two stresses with a linear boundary while QDA can section more stressors with multiple quadratic boundaries. A lower-class discrimination with QDA risks with overfitting. A higher-class LDA likely fail in classification (Sankaran et al., 2011; Song et al., 2011; Mahesh et al., 2008; Lowe et al., 2017; Lassalle et al., 2018).

Five treatments (gas leakage, SI, HMC, DE, and a control group) were discriminated with the QDA. The differentiation of stressors was carried out on any individual group of plant species. To do so, 343, 386, 376 hyperspectral reflectance samplings were collected from Grass, South, and Gem, respectively. The spectral signatures were extracted from the ROI of the plants that exhibited notable stress symptoms. Reflectance data on each species of stressed plants were pooled and randomly split into 70% for model training and 30% for testing. The random selection of reflectance dataset is done by MATLAB and LDA/QDA model establishment, and classification is accomplished with the Unscrambler X software. The flow chart of the hyperspectral reflectance collection, processing and classification is presented in Figure 2.3. The entire process is divided into two steps: data acquisition and data transformation and model construction.

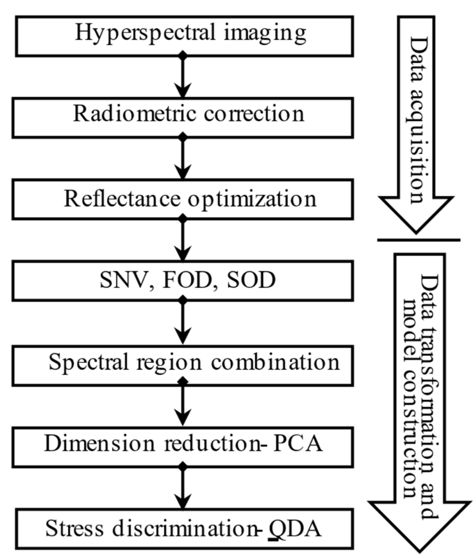

Figure 2.3 Flow chart of reflectance collection, processing, and stress discrimination

2. Results and discussion

2.1 Gas leakage identification

2.1.1 Raw hyperspectral reflectance extraction and stress symptoms

The hyperspectral responses under non-optimal ambient stress conditions were observed to be different from those under optimal/normal conditions due to the foliage composition and morphology changes of plants (Cotrozzi and Couture, 2020). Each spectral signature was retrieved from the plants that displayed obvious physical symptoms and were assigned corresponding stressor labels for dimensionality deduction and stress identification and classification. Every pot of a plant was securitized to locate the symptom spots in the HSI and RGB images.

2.1.2 Spectral correlation and dimensionality reduction with PCA

Hyperspectral redundancy indicative of the similarity between bands was quantified by the spectral correlation (Adjorlolo et al., 2013). Figure 2.4 shows the coefficient of correlation between two bands in VNIR and SWIR of the plant. The correlation map demonstrates the redundancy of spectral information. In the VNIR range, the most informative wavelengths are 540 nm in green, 680 nm near red, and 720-1000 nm. In the SWIR range, wavelengths between 1950 nm and 2400 nm are less interrelated as observed by Song et al. (2011).

(a)

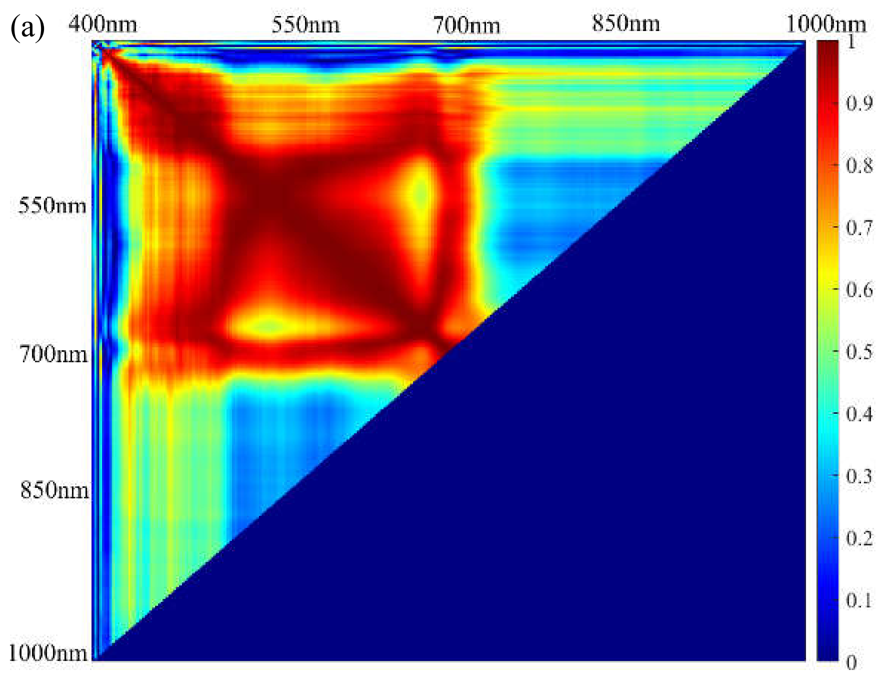

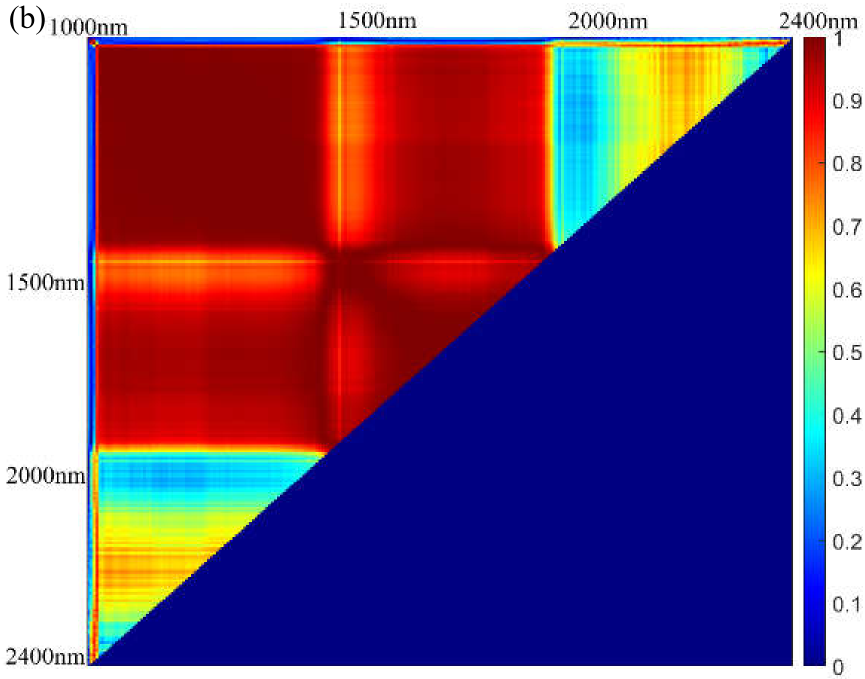

Figure 2.4 Coefficient of correlation of wavelengths of leaf hyperspectral data: (a) VNIR, and (b) SWIR

Based on the understanding of electromagnetic radiation and the interrelation of information at various wavelengths, the original hyperspectral data were compressed for efficient and effective stress detection. Without knowing individual wavelength contributions to the spectral information of interest, PCA was performed to project high-dimension spectra into several principal components (PCs), e.g., PC1-PC7. The eigenvalue of each PC indicated its contribution to the spectral information of interest. In the case of gas treatment, the accumulative explained variance by various PCs is presented in Table 2.2. The spectra loadings for the first three PCs are presented in Figure 2.5 to demonstrate the significance of a wavelength λ_i in each PC. As shown in Table 2.2, the first three PCs account for more than 96% of the variance and seven PCs can almost represent the whole spectra information (> 99%). In the direction of PC1, the REG region and 720 nm-1000 nm in the VNIR range account for the most and second most variabilities while 1950 nm-2400 nm in the SWIR range corresponds to higher loadings. Due to their overlapped spectral loading ranges, the directions of PC2 and PC3 are considered together. The green absorption (540 nm) and the REG in the VNIR range are two major dominating spectral regions that explain 6% of the original variance. In the SWIR range, 1400 nm and 1930 nm related to water feature contribute to the variance more significantly.

Table 2.2 The accumulated explained variance of full spectra from PCA

	PC1	PC2	PC3	PC4	PC5	PC6	PC7
Calibration (%)	88.3	93.7	96.2	97.9	98.4	98.9	99.2
Validation (%)	87.8	93.1	95.5	97.3	97.6	98.2	98.3

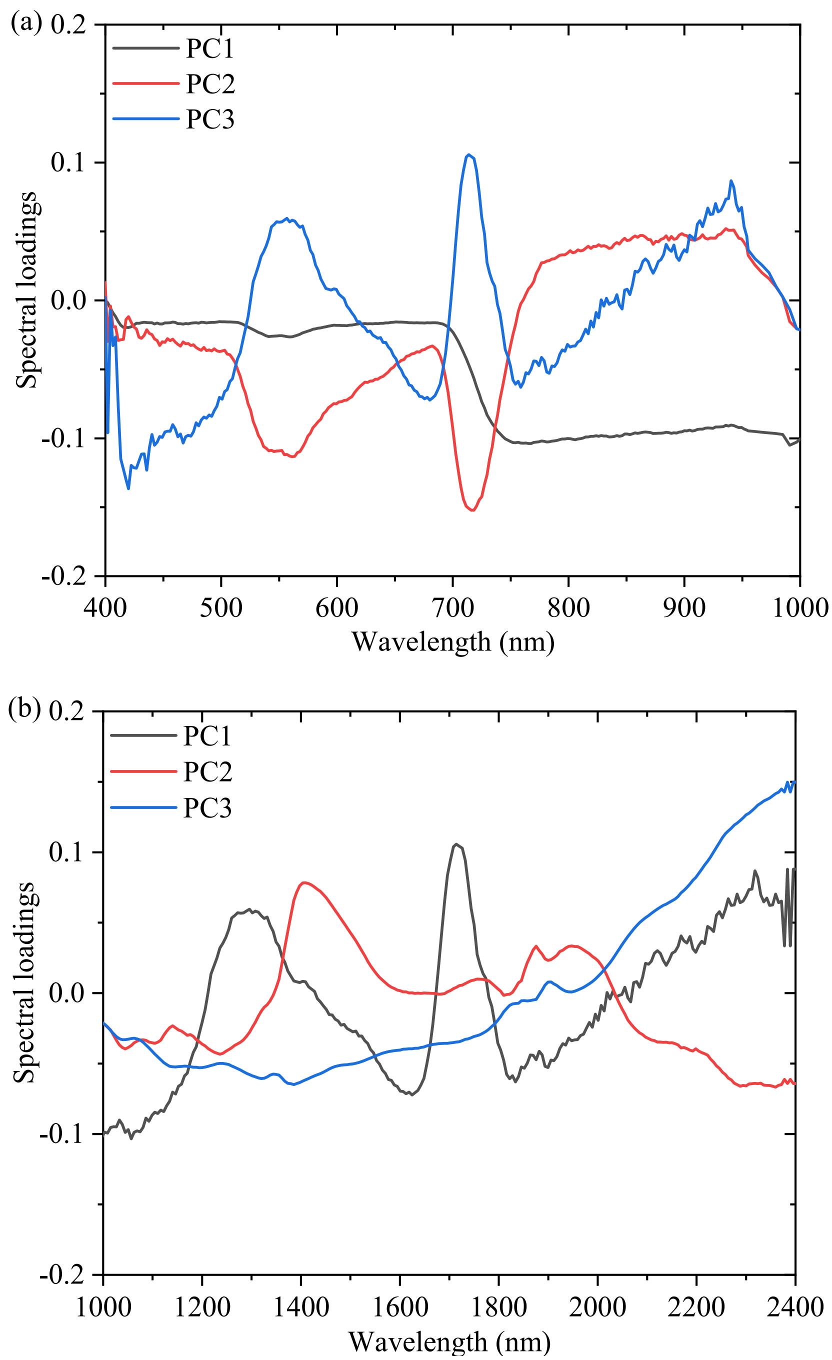

Figure 2.5 Spectral loadings for the first three PCs: (a) VNIR, and (b) SWIR

2.1.3 Gas treatment identification with LDA

The VNIR, SWIR, and full spectrum were considered in the LDA model for gas stress identification. Only the hyperspectral reflectance curves acquired from the gas-stressed and untreated control sets of plants were pooled in this case. Figure 2.6 presents the gas stress identification results with LDA for different plant species. In Figure 2.6, training and test accuracies are indicated by blue and orange columns, respectively, while the PCA-reduced features in LDA is represented by the number of PCs. The LDA model training accuracy ranges from 67.3% to 93.3% for a complete combination of four spectral transformations and three spectral ranges. Among the three spectral ranges, VNIR yields higher accuracy in LDA model training than SWIR and the full spectrum. As for the influence of data transformation on LDA modelling, FOD gives rise to the highest accuracy regardless of the spectral ranges used and SOD is the most uncertain in accuracy. The best identification (> 90% in accuracy) for gas stress is achieved with a combination of VNIR range and FOD transformation consistently for all three species of plants. Except for the Grass and South Gem in the SWIR range, SNV improves the accuracy in gas stress identification. It is noted that the number of PCs used in the stress identification varies from 3 to 5 among various data transformations. Gas stress identification with the original data requires the same number or more of PCs to represent a minimum of 95% variance of the data in feature space.

As shown in Figure 2.6, the accuracy in LDA model test is consistent with that in LDA model training. The best detection for gas stress is also achieved with a combination of VNIR range and FOD transformation. However, the stress detection accuracies on Shrub South and Shrub Gem are 90.5% and 88.5%, which is substantially higher than 78.6% on Grass.

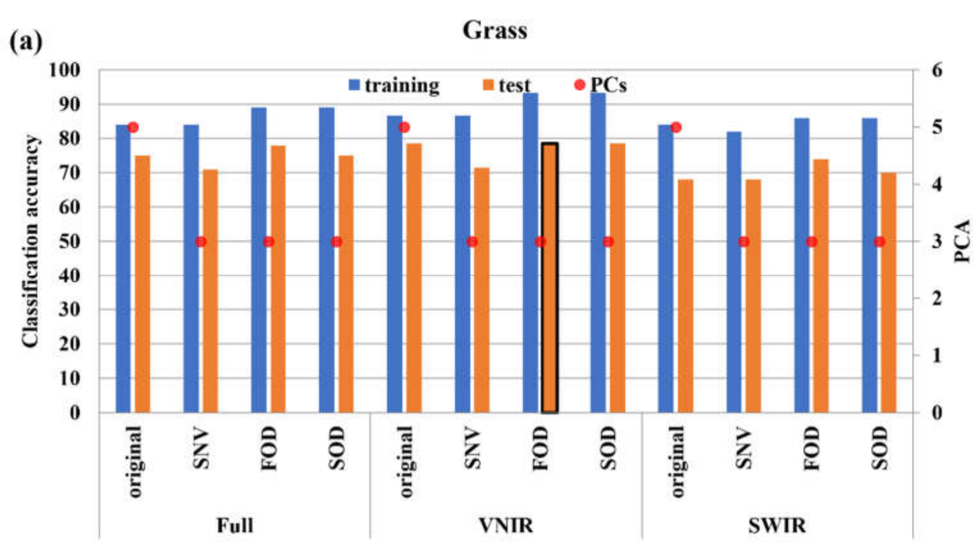

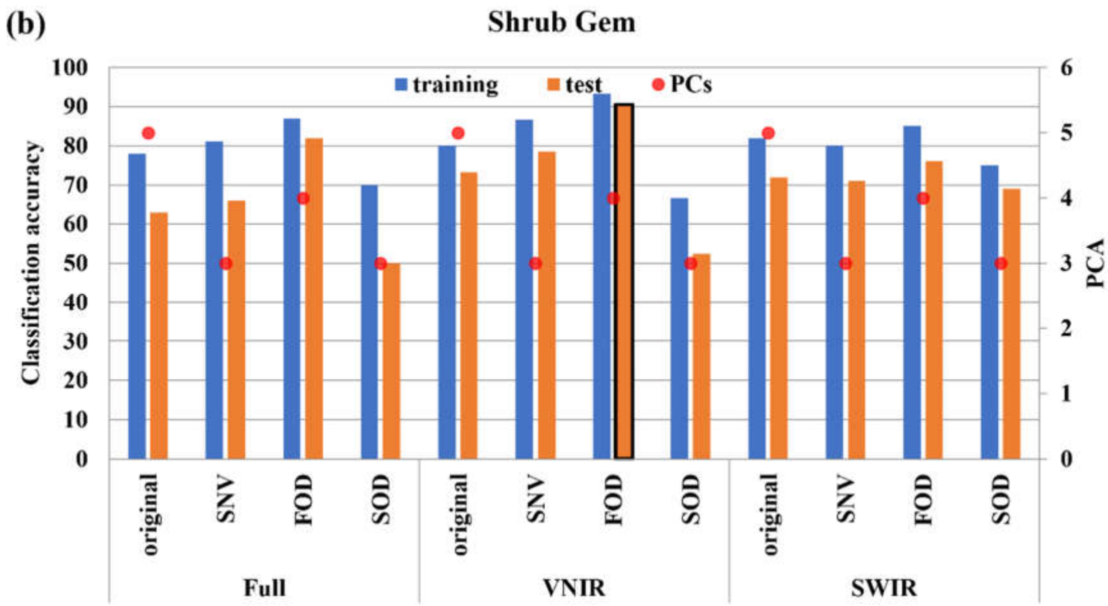

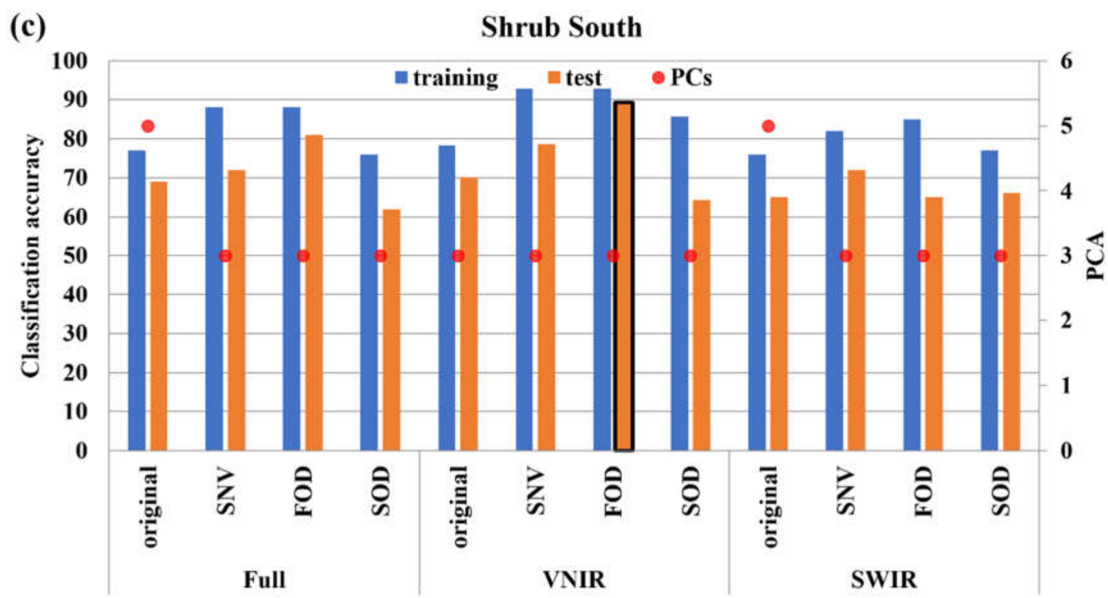

Figure 2.6 LDA-based gas stress identification from different plants: (a) Grass, (b) Shrub Gem, and (c) Shrub South

2.1.4 Gas stress discrimination from three other treatments with QDA in multi-class classification

SI, HMC, and DE were considered as distraction parameters for the detection of gas leakage in multi-class discrimination. Considering different covariances between classes, QDA was used to find optimal boundaries of the classes with a nonlinear function (Sankaran et al., 2011; Mahesh et al., 2008; Lowe et al., 2017). The hyperspectral curves collected from three species of plant under five treatment conditions were pooled for QDA classification.

Figure 2.7 presents the gas stress classification accuracy for each species with different hyperspectral curves in spectral range and data transformation. As it classifies stressors with a flexible boundary, QDA generally yields high accuracy in terms of model training (Lowe et al., 2017). The average training accuracy of all cases included in Figure 2.7 for different spectral ranges and data transformations surpasses 80% in gas stress discrimination model. The test accuracy of the model, however, differs from the training accuracy by at least 15.8%; the test accuracy could be as low as 50% of the modeling accuracy. Overall, VNIR shows the highest accuracy, and the full spectrum gives the second highest accuracy, which are consistent with the results obtained from one-class gas identification in Section 2.1.3. Most of the discrimination accuracies during model testing achieved from the hyperspectral reflectance in the SWIR range are below 60%. For model testing, FOD remains the most effective transformation in the gas stress discrimination, which is also consistent with the findings from one-class gas identification in Section 2.1.3. A combination of VNIR and FOD can most effectively separate gas stress from the other stressors with 76.3%, 70.4% and 68.8% accuracy for Grass, Shrub South, and Shrub Gem, respectively.

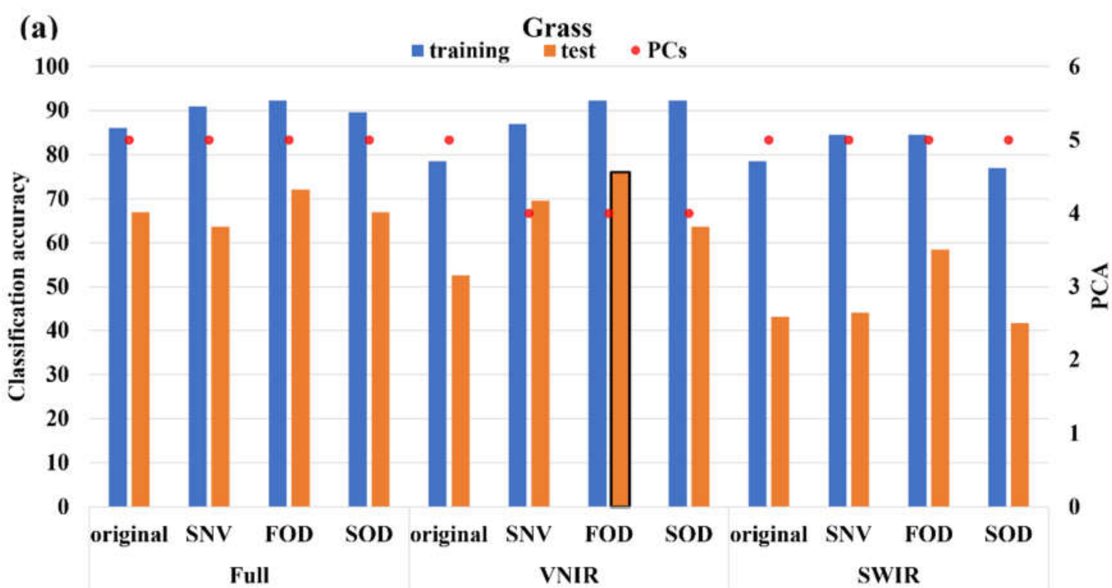

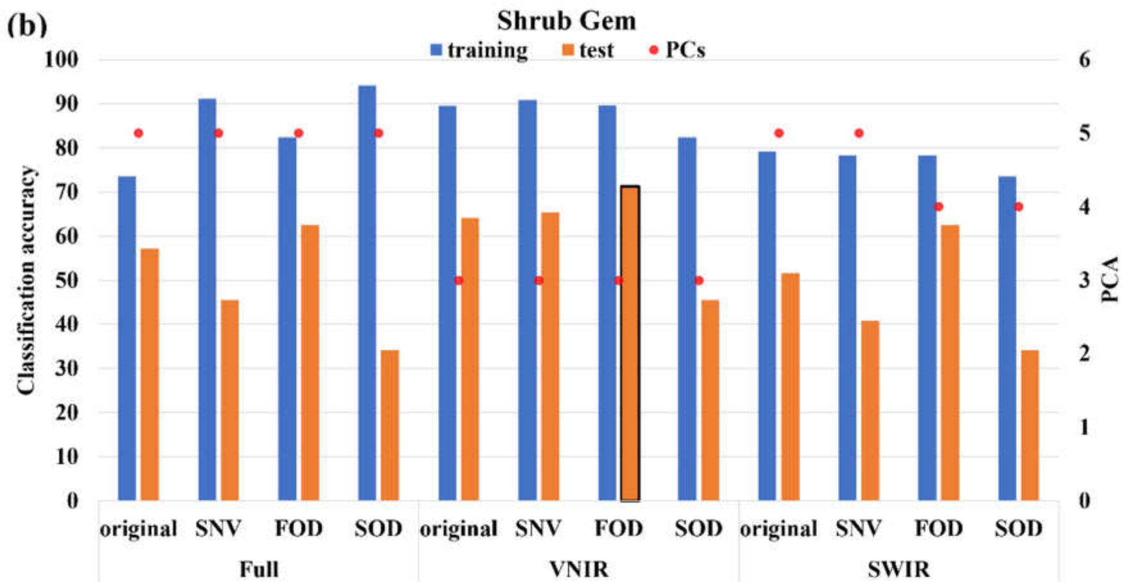

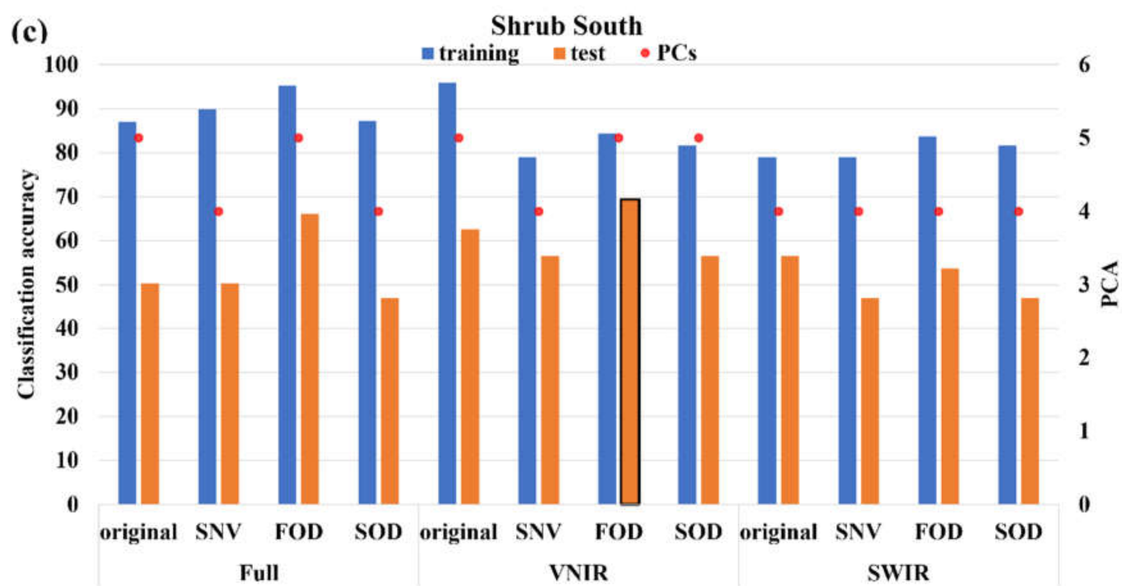

Figure 2.7 QDA-based gas stress discrimination from three other stressors on different plants: (a) Grass, (b) Shrub Gem, and (c) Shrub South

As observed in Figure 2.7, most combinations of spectral range and data transformation require 5 PCs to represent 95% of their key information in the original space. This is because an effective classification of multiple (four) stressors in a pool with an unstressed reference requires the use of more features in comparison with a single gas stressor in Section 2.1.3. Nevertheless, the number of PCs required for gas stress separation from the VNIR-FOD data remains 3 for all plants except Shrub South. The exception demands a minimum of 5 PCs for an accurate discrimination of gas treatments applied on the Shrub South.

2.1.5 Gas stress discrimination from another treatment with QDA in two-class classification

Section 2.1.3 and Section 2.1.4 discussed two extreme scenarios for gas stress detection with no and three disturbances, respectively. In applications, gas leakage in an environment with one disturbance stressor is more practical since natural stressors (SI, HMC, and DE) are seldom present at one location. Section 2.1.3 and Section 2.1.4 also indicated that the hyperspectral reflectance in the VNIR range can yield the most accurate detection results. Thus, only spectra in the VNIR range are included in the following analysis. Figure 2.8 shows the gas stress detection results with QDA when the gas stressor is pooled with no stress reference and one other predefined stressor on three species of plants. In Figure 2.8, 'Ref-Gas-DE' denotes a hyperspectral reflectance pool of three treatment conditions: no stress reference, gas treatment, and drought exposure.

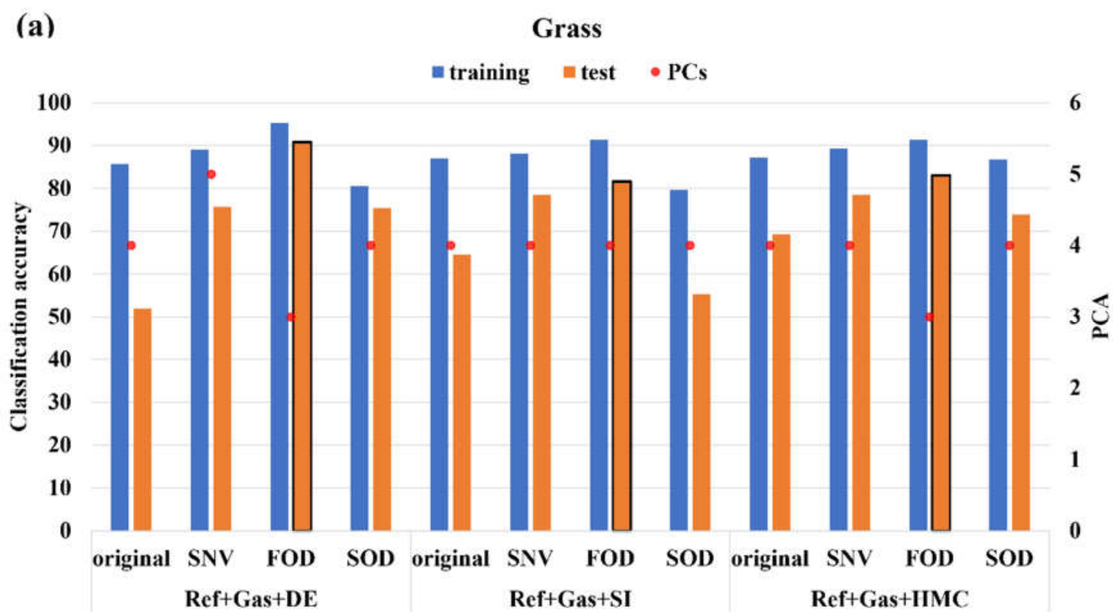

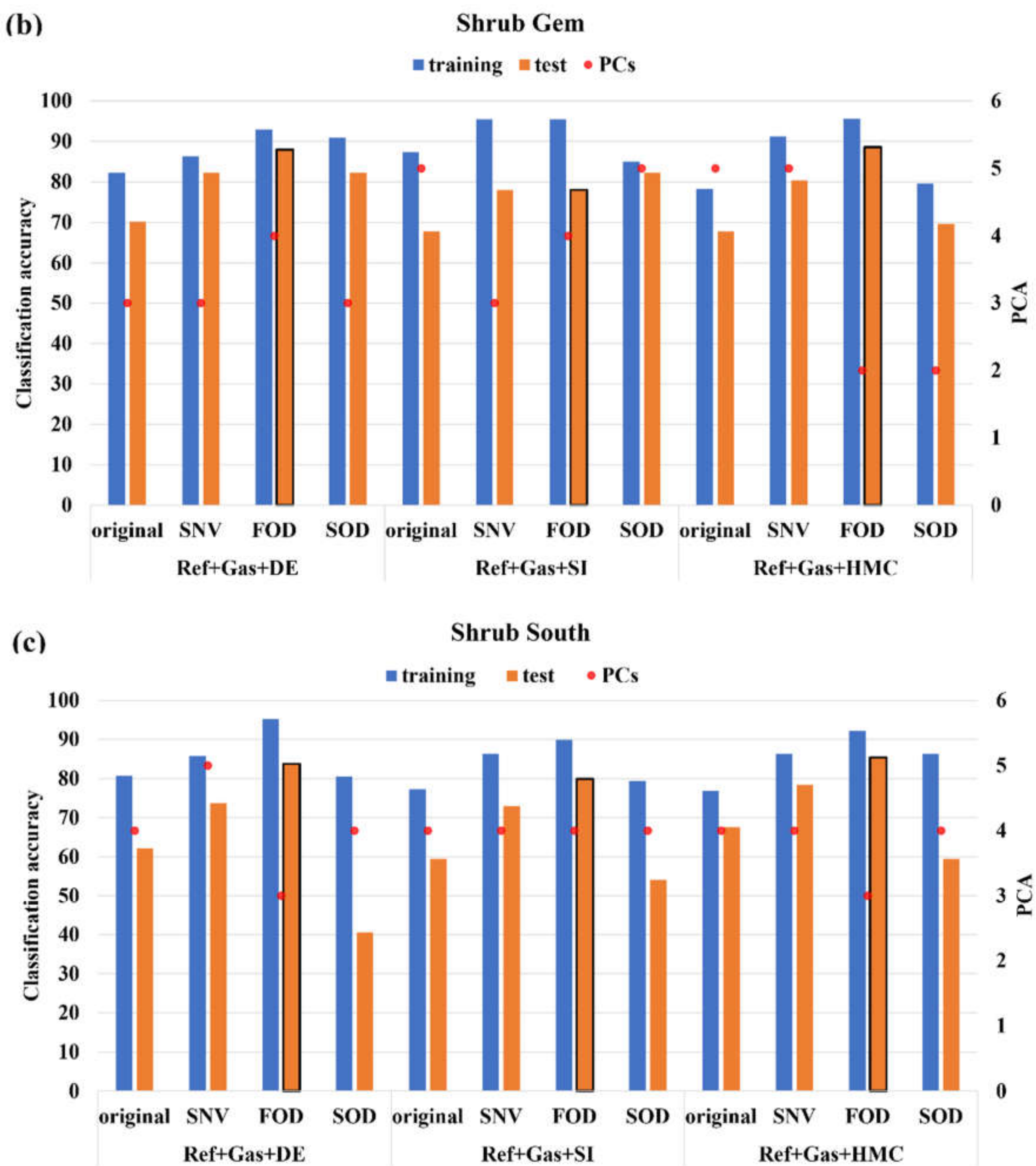

Figure 2.8 QDA of VNIR-ranged spectra for gas stress discrimination from one distraction stressor on different plants: (a) Grass, (b) Shrub Gem, and (c) Shrub South

Like Figure 2.6 and 2.7, Figure 2.8 indicates that FOD and SNV both yield more accurate classifications of stressors than that from the original data without any transformation. The most successful FOD transformation (85% accuracy) is approximately 5% more accurate than the SNV transformation. The third data transformation, SOD, is least effective to separate the natural stressor from gas leakage on each species of plants. The presence of drought exposure (DE) is most favorable to the gas stress detection with an accuracy of over 83.8% in which the lowest accuracy is associated with the Shrub South. The presence of salinity impact (SI) makes the gas detection most difficult, giving results that are generally 5% lower in accuracy than the HMC case and 8% lower than the DE case. The gas detection results appear consistent among all three species of plants, making the proposed method robust in practical applications.

2.1.6 Discussion

The use of a broadband spectrum in gas stress discrimination provides redundant information due to multicollinearity between wavelength bands. The information redundancy has been revealed by the inter-band correlogram that REG, 720-1000 nm in the VNIR range and 1930-2400 nm in the SWIR range, are almost independent as indicated in Figure 2.4. Some local regions around 550 nm and 680 nm in the VNIR range and spectra around 1400 nm in the SWIR range are also less correlated. Song (2011) observed similar spectral independency in the context of wavelength selection of hyperspectral reflectance for the discrimination of the spectral variations of paddy rice under different cultivation conditions. The PCA analysis in this study also demonstrated the significance of these spectra in the range of VNIR and SWIR, as shown in Figure 2.5. Therefore, it is believed that the spectra in these regions and locals should be considered in priority when the changes on the plant leaves are investigated.

Although spectra can be qualitatively related to stressors in plant identification and classification, their response to the plant stressors is yet to be quantified with better understanding on underlying mechanisms. After the PCA analysis, the spectral contribution can be described by the spectral loadings and the corresponding significance is denoted by the descending order of eigenvalue of PCs, where PC1 explains the most variability of the original data. The spectral loading of PC1 as shown in Figure 2.5 reveals that the REG spectral regions, 720-1000 nm and 1930-2400 nm, account for 88.3% of the original data as indicated by its corresponding PCA results in Table 2.2. The spectral loadings of PC2 and PC3 demonstrate that the local spectral bands around 550 nm, 680 nm and 1400 nm are the secondary variance source that illustrates 5.9% of the original data. The scattering of light from plants in the range of 720-1000 nm is dominated by the cellar components such as epidermis, cellulose, and soluble protein changes (Paul et al., 2019). Likewise, the spectral bands in 1930-2400 nm are related to the structural components of the plant cell such as lignin (Behmann et al., 2014). According to the spectroscopic analysis of plant pigments, the REG and 550 nm are a reflection of chlorophyll (chlorophyll a and chlorophyll b) and carotenoid while 1400 nm and 1930 nm are dominated by the presence of water (Thenkabail et al., 2013; Havaux, 2014). With the given importance of the spectral bands, it is suggested that chlorophyll, cell wall component and leaf physical structure featured bands can be primary consideration while the accessory leave pigment and water featured wavelengths are secondary information in the context of plant stress detection.

The influence of spectral ranges (VNIR, SWIR or full spectra) on the accuracy of gas stress detection is notable. The VNIR range of spectra yield higher accuracy than the full spectrum in both the discrimination model construction and gas leakage identification as discussed in Section 2.1.3 and Section 2.1.4. In contrast, the SWIR range accounts for the least detection scenario with lower accuracy. To investigate why their accuracies differ greatly, it is important to note that the discriminant technique, both LDA and QDA, was applied to the hyperspectral reflectance acquired when the plants have already exhibited obvious stress symptoms. Therefore, the uncertainty of the stress status labeling can be eliminated and the likelihood for misclassification of the plant stressors is reduced. As LDA and QDA classify different plant stressors using the variations in certain spectral ranges, the notable difference in gas leakage identification accuracy between the VNIR and SWIR ranges implies that the cellar components of the plants are more sensitive to the difference in various stressors (gas leakage, SI, HMC and DE) than the structural components (Hennessy et.al., 2020). For example, gas stress increases the reflectance on crops at 550 nm and decreases at NIR but induces no apparent change in the SWIR range (Smith et al., 2004). Song et al. (2011) confirmed that spectra in the VNIR range are more responsive to stress. The full spectra including less-responsive information in the SWIR range smears the more-responsive information in the VNIR range, thus resulting in a lower accuracy of gas detection than the use of the VNIR range. Another potential reason for the low accuracy in gas detection from the SWIR range spectra is attributed to the developmental stages of stress on plants. The tests in this study lasted 109 days excluding the acclimation period. This duration appeared too short to exhibit the change to stressors to its full extent in the SWIR range.

The adoption of spectral signature transformation makes a significant difference in accuracy of gas leakage detection. The FOD achieved the highest accuracy among the original hyperspectral curve and its different transformations considered in this study. The minimum average accuracy of the FOD transformation is 78.6% both in gas stress identification as shown in Figure 2.6 and gas stress discrimination as shown in Figure 2.8 during the predictive tests. The FOD emphasizes the reflectance variation with respect to wavelength or the slope of a hyperspectral curve; it can distinguish even the imperceptible features in hyperspectral curves by reducing the ambience effect. For example, the REG shift can be identifiable from the derivative analysis but not feasible in the dimension of hyperspectral reflectance. The FOD was also found the most accurate method in stress identification between oil seepage and heavy metal contamination (Lassalle et al., 2018). Although it can neutralize the multiplicative effect of factors, making the spectral curves taken from different samples more comparable, the SNV transformation keeps the dimension of hyperspectral curve with multicollinearity between wavelengths. In most cases, the SOD leads to the lowest accuracy in detection of gas leakage. This is because the high-order derivative analysis is highly sensitive to noise dispersiveness. That is, the noise at a specific band diffuses forwards and backwards in the process of derivative analysis, thus contaminating useful information. Furthermore, the second-order derivative represents the curvature of the hyperspectral curve; it is positive when concaved upward and negative when concaved downward even though the local change in reflectance data is similar, resulting in low accuracy in detection of a shallow peak or valley on the hyperspectral curve. In addition, the number of PCs required to classify stressors successfully is 3 from the FOD but 4 or 5 from the SOD. These results suggest that the FOD operation requires less effort to locate the changes in hyperspectral features due to stress effects.

By comparing Figure 2.7 with Figure 2.8, the QDA of VNIR-ranged spectra when five treatment cases are co-present is less accurate than when gas treatment is pooled with one other natural treatment only. As indicated in Figure 2.7, the FOD transformation can differentiate the gas stress from the other three natural stressors and the control reference with an accuracy range of 68.9% - 76.2%. As indicated in Figure 2.8, the FOD can distinguish the gas stress from the others with an accuracy range of 78.3% - 90.8%. Figure 2.8 further indicated that it is the easiest task to separate the gas stress from the DE effect with a minimum accuracy of 83.8% (for South) and the most difficult from the SI with an averaged discrimination accuracy of 79.8% (for Gem). There are two reasons for this accuracy contrast: number of discrimination classes and number of training samples. In Figure 2.7, five classes were considered. In general, the more the number of classes, the less accurate the discrimination of the classes. As the number of classes increases, three are more grey boundary areas to separate, making the discrimination of gas stress more difficult. At the same time, the total training samples associated with the three natural stressors in Figure 2.7 are approximately three times as large as the training samples associated with one natural stressor in Figure 2.8. The overwhelming training data from the three natural stressors may dominate the process of machine learning over the effect of the gas stress. As a result, this biased dataset generally reduces the detection accuracy of the gas stressor due to its small samples.

2.1.7 Conclusions

This chapter summarized the feasibility study on detecting gas stress on vegetations from hyperspectral reflectance as it contains variance of the vegetations derived from exposure to the stress. Due to plant generic responses to electromagnetic radiation, the transformed hyperspectral data in different spectral ranges (VNIR, SWIR, and full spectra) were compared for the first time. The multivariate analysis technique (LDA or QDA) was used to statistically differentiate the gas stress from both the unstressed reference and three natural stressors (DE, HMC, and SI). Based on the extensive tests and analyses, the following conclusions can be drawn:

1. The LDA can be applied to effectively identify the gas stress on vegetations from unstressed vegetations with an accuracy of 78.6% - 90.5% in the two-class detection process.
2. With the distraction of three natural stressors, the QDA can be applied to discriminate the gas stress from the natural stressors with an accuracy of 68.8% - 76.3% in the five-class detection process.
3. When distracted by one natural stressor (DE, HMC or SI), the QDA can differentiate the gas stress from the distracted natural stressor and the unstressed reference with an accuracy of 78.3% - 90.8% in the three-class detection process. This level of accuracy is comparable to that for gas stress identification from the unstressed vegetations. These results have practical implications in natural gas and oil pipeline industries.
4. The FOD of the VNIR-ranged spectra (400-1000 nm) can always lead to the highest accuracy in almost all detection cases. The FOD can effectively simplify the feature space of raw data by reducing the number of PCs required for better classification.

2.2 Gas stress development

2.2.1 Gas stress development

After the gas is delivered to the plant, the microbial environment will be altered due to the ingress of methane. In addition, oxygen is replaced or diluted, which potentially affects the respiration of the plants. Vegetations exposed to the adverse condition call for the internal system to suppress the reactive oxygen species (ROS) to prevent the breakdown of the plant functions like the decomposition of Adenosine Triphosphate (ATP) to supply energy. The changes are demonstrated as the sign of both physical and biochemical stress. Biochemical changes precede the physical changes. Hyperspectral camera can capture the biochemical changes by the variations in the hyperspectral reflectance to indicate the stress occurrence. In an aim of gas stress detection, it is also instructive to understand how much time is required to induce 'visible' biochemical changes on plants in terms of the spectral signature from a hyperspectral camera.

2.2.2 LDA models for stress development identification

Hyperspectral data were arranged chronologically after the methane gas had been applied to test the development of stress. Likewise, LDA models were established by integrating the hyperspectral reflectance curves from plants under gas stress and control treatments after the presence of obvious physical changes. Figure 2.9 illustrates how the LDA stress identification model works for different plants. Each model integrates the spectral curves under control and gas stress treatments. As demonstrated in Section 2.1.4 and Section 2.1.5, FOD yields the highest accuracy. Thus, all the spectral curves are subjected to the FOD transformation prior to the model construction and stress identification. The number of the spectral curves used to train the stress identification model is 195, 296 and 209 for Gem, South and Grass, respectively. The LDA model groups the hyperspectral reflectance from different treatments based on the distance in the feature space. In each model, 70% of the samplings are used for training while the remaining 30% for testing. The 10-fold cross-validation results indicated that there is a 94.5%, 88.18% and 89% probability that the LDA can discriminate each of the stress treatments.

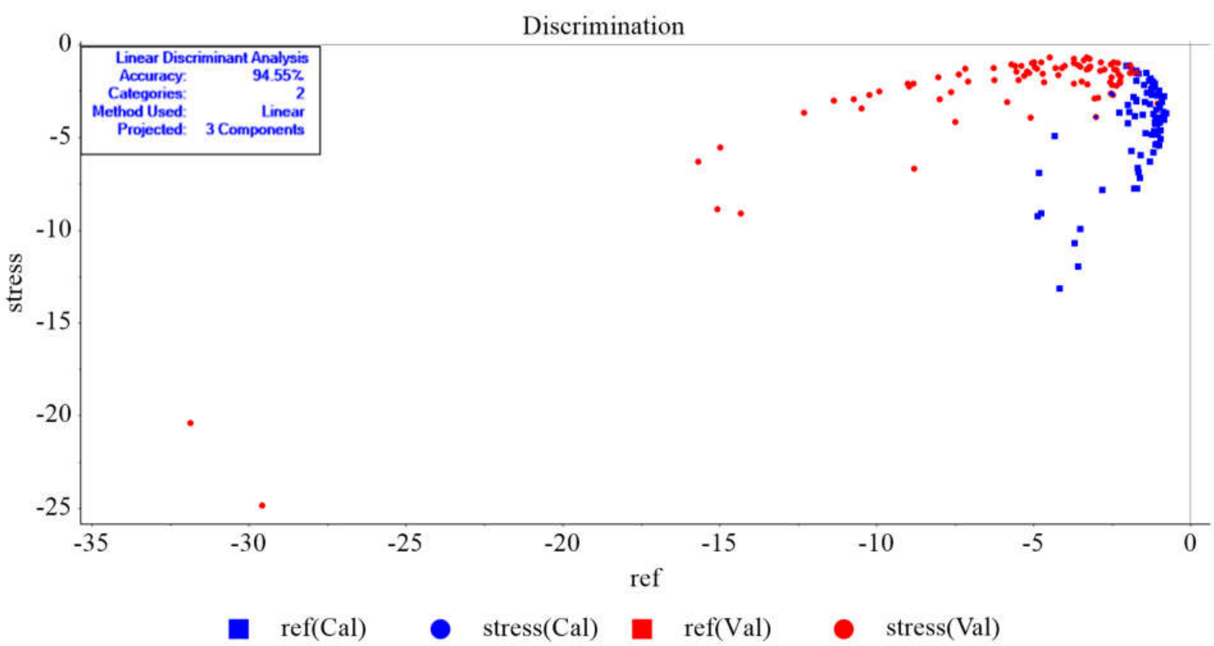

(a) Gem

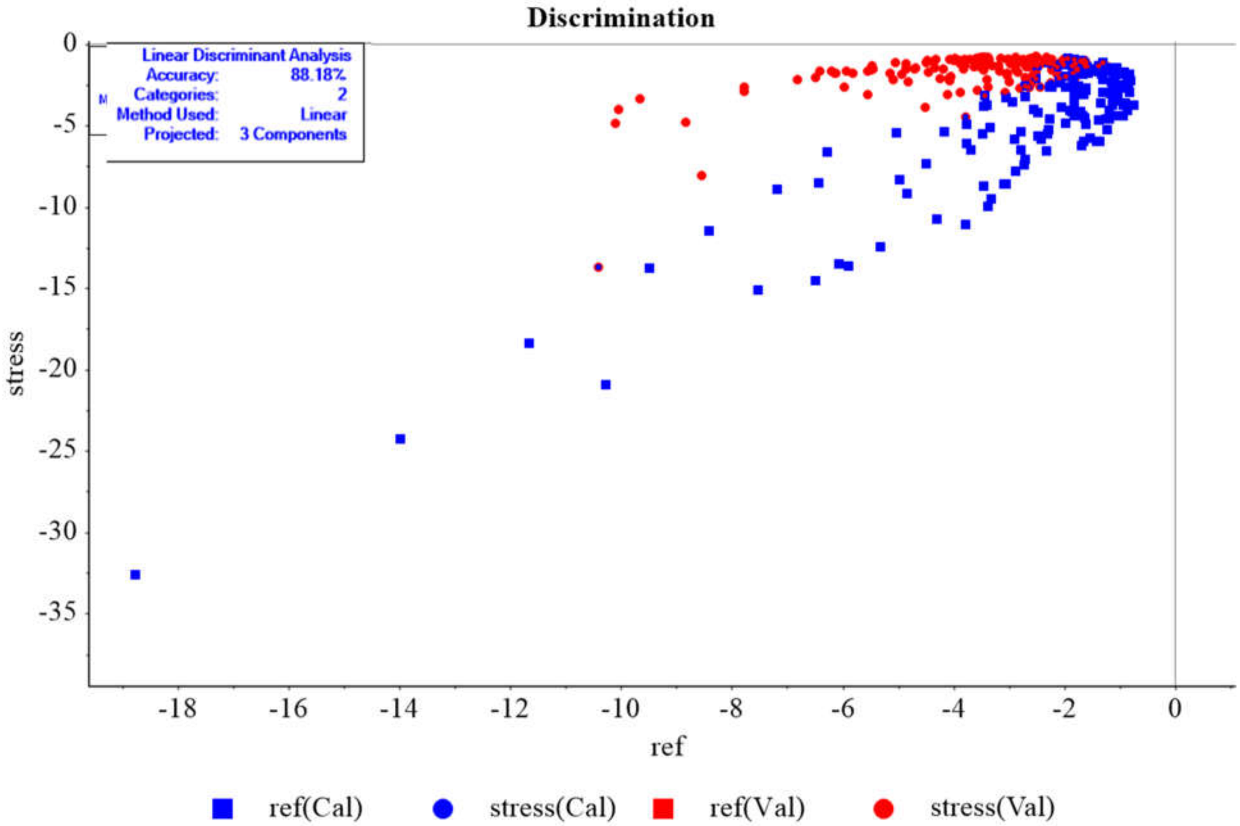

(b) South

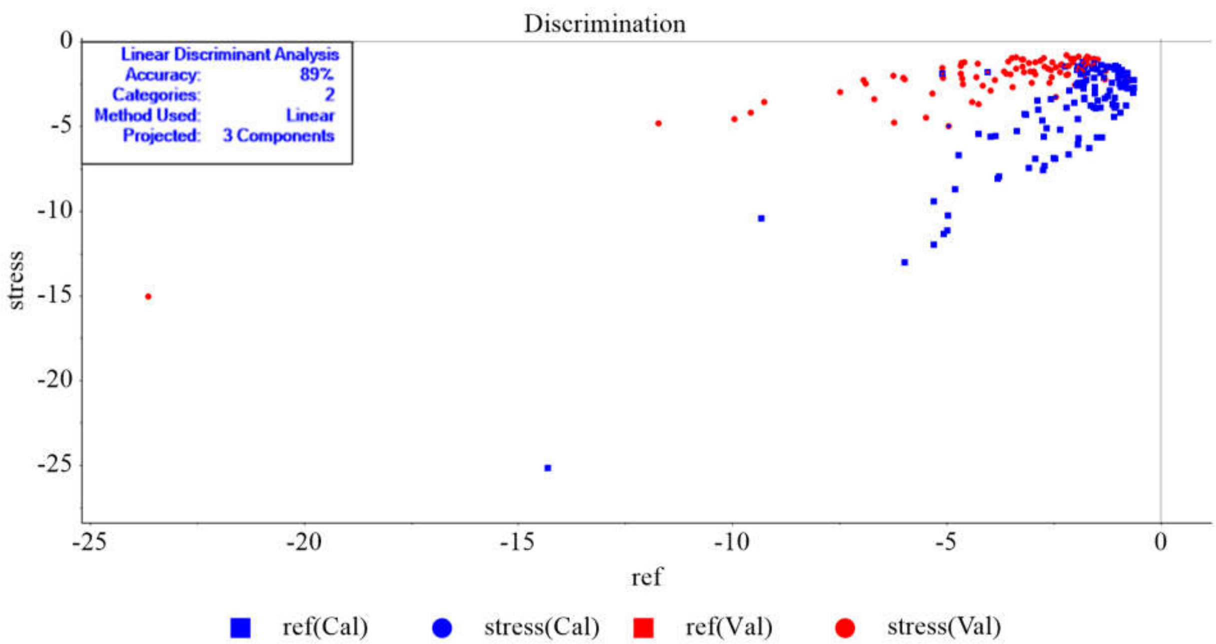

(c) Grass

Figure 2.9 LDA discrimination models for gas stress identification from different plant species

2.2.3 Results and discussion

The probability of the gas stress occurrence on different plants is presented in Figure 2.10. The probability of control and stress treatments are calculated respectively. The control condition is included as a reference in the discrimination test to demonstrate that the LDA model is not biased during the stress identification. As indicated in Figure 2.10, the plant under control conditions can be detected at an accuracy of 78.31%-93.58%, 78.86%-95.42%, and 81.25%-94.31% for plant Gem, South and Grass, respectively. As the nonstress status of the plants can be effectively detected, the high accuracy indicates that the LDA models are not biased between the samplings and can be a reliable model for the detection of the stressed vegetations. The stress probability increases over time in days. For Gem, the possibility of stress on the plant ascends from 1.64% at day 3 to 66.27% at day 20 and finally stabilizes around 76%. Plant south yields a similar stress development trend as that of Gem. The stress occurrence rate starts from 11.04% and reaches the critical 50% after 10 days. At day 32, there is a 75.88% possibility that shrub South get stressed. The identified stress probability on Grass fluctuates greatly; it goes beyond 50% at day 32 but drops to 42.20% at day 37. After 49 days of gas stress induction, the likelihood of detected gas stress remains below 60% though it finally reaches 96.06% at day 56.

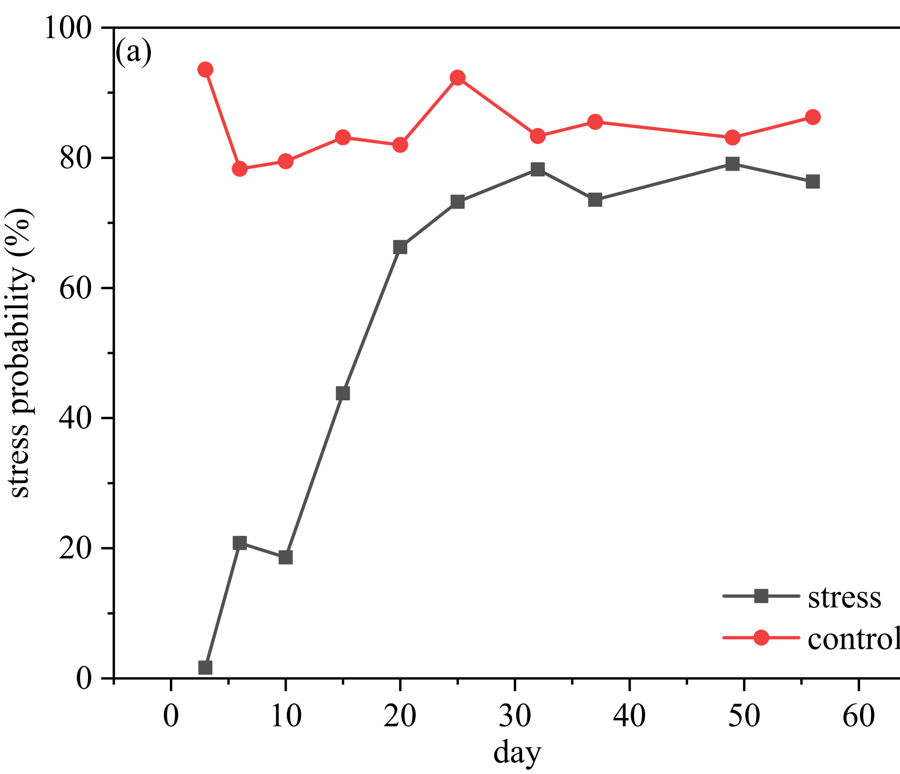

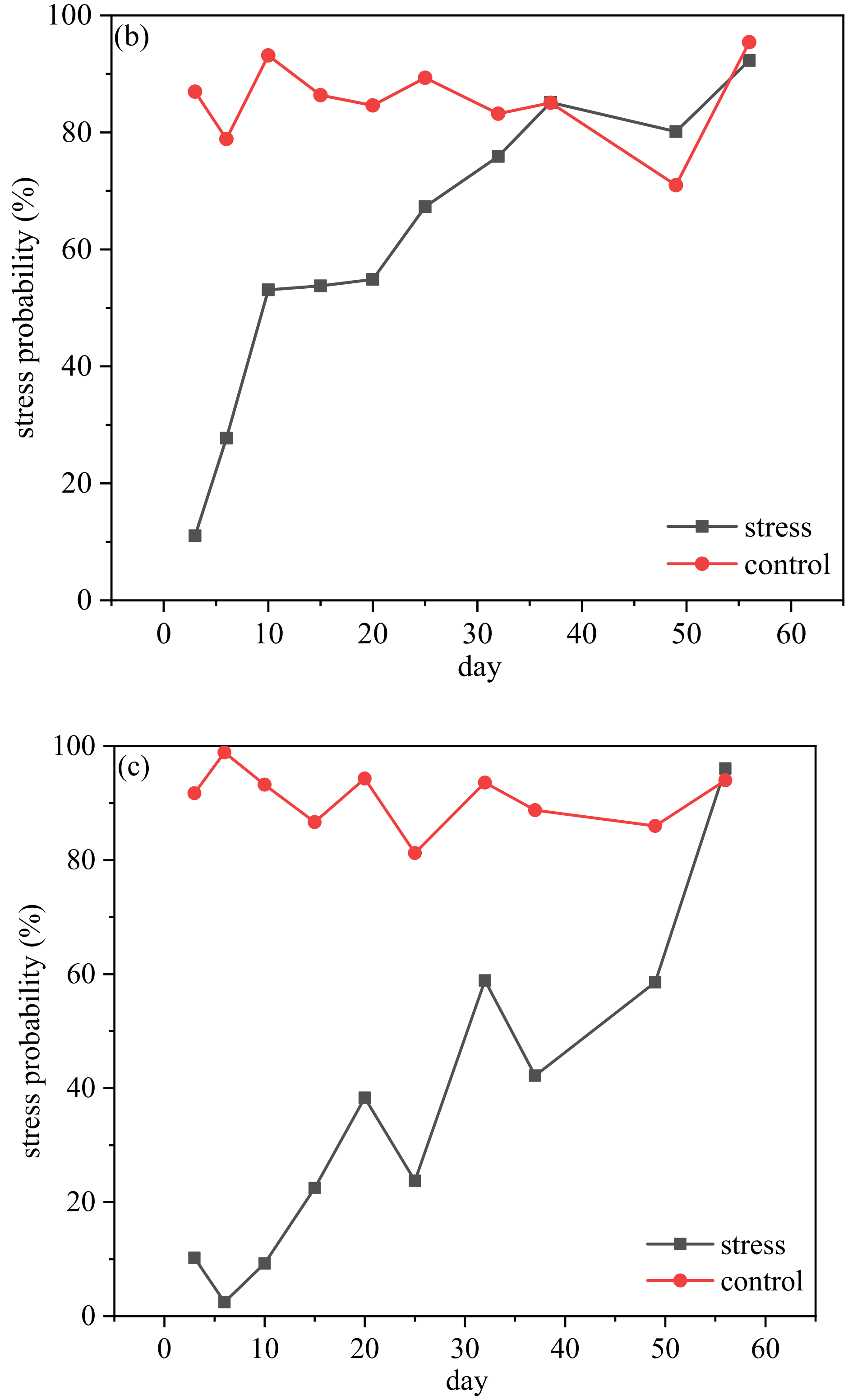

Figure 2.10 Probability of the identified methane gas stress in time series on plants: (a) Gem, (b) South, (c) Grass

As the LDA model in this context performs a binary classification, 50% is a critical point for the stress status identification. To ensure over a 50% probability of stress detection, it takes more than 20 days of stressor application on shrubs (the Gem and South) and 32-49 days on the Grass. Due to their more developed roots in comparison with the Grass, the shrubs are likely to sense the environmental alteration in soils and manifest their stress conditions sooner. In addition, the leaf tissues of the shrubs are much thicker than that of the grass. The larger exposure of the tissue is more sensitive to the stress according to the negative feedback mechanism. That is, the defense mechanism is activated to prevent the malfunction of leaves before breakdown. As the stress develops, it is noted that there is approximately 80% of probability that the shrubs get stressed due to the methane gas leakage after 35 days. In comparison, 50 to 59 days of stressing are required to induce more than 80% of the probability for stress existence on the Grass. Basically, the stress on the Grass develops slower than that on the shrubs. In addition, the stress identification results are not as stable as those of the shrubs, which even drops 16% at day 37 after it reaches 58.8% at day 32. Overall, stress on the shrub Gem and South can be fully developed after 32 days of gas treatment while more than 50 days are required for the Grass.

2.2.4 Conclusions

Based on the experimental results and analysis, the following conclusion can be drawn:

1. Gas stress development varies greatly between plants. Grass is more tolerant to the impact of gas treatment than the shrubs. To achieve a 75% or higher probability gas stress on the plants, 32, 37 and 56 days are required for shrub Gem, shrub South and Grass, respectively.
2. The detected gas stress probability increases monotonically over time for shrubs (Gem and South) but fluctuates for the Grass before it reached the final 96.06% probability at day 56.

V. Task 3 Develop a deep learning neural network for the assessment of pipeline and ground surface conditions

With the aim of detecting vegetation stresses as an indicator of methane gas leakage, many elements, biochemical and physiological, are involved in health/stress status indexing. Stress indicator can be a powerful tool in plant stress detection as it employs little spectral information in particularly sensitive wavelengths when characterizing the plant conditions. In view of the spectral signature, the characteristic pattern of light reflected from a surface is the product of different chemical compounds' interaction with light absorbing, reflecting, or transmitting at different wavelengths.

Although the reflectance spectra of plants can be quite complex, there are several common features whose magnitudes (peaks and valleys in a spectrum) have been correlated with the chemical properties of plants at various stages in their life cycles. Many of these spectral features have been characterized by "Spectral Indices", each index being a numerical value that largely depends on the relative reflectance values at a small number of wavelengths. The calculation of spectral indices is a method to reduce the complexity of spectral images, thus greatly simplifying the analysis of the data. Interested wavelengths are selected based on the unique plant response under stress. For example, chlorophyll on plant (e.g., alfalfa) leaves under heavy metal stress decreases as the centered magnesium is replaced by the heavy metal elements such as Cu^{2+} . As chlorophyll is characterized by the reflectance at 670 nm and 540 nm, the photochemical reflectance index (PRI) that is a ratio of reflectance values at the two wavelengths decreases. Under stress conditions, the stressed plant demonstrates differences in term of the stress indicators, which facilitates the discrimination of stress origins such as gas leakage. Given the spectral indices, some changes of plants due to stress effects can be mapped to discern the stress. In addition, spectral indexing mapping makes it easier to identify the stress from a neural network as the dimension of the input data change reduces greatly.

Just like light reflectance from a hyperspectral camera is responsive to the chemical change of plants due to gas impact, thermal radiation from an infrared camera is another feature for the detection of gas leakage spots. Methane gas in soil is known to strap heat, which makes the gas leakage area detectable in thermal images. Beside methane's inherent heat-trapping property, the gas tress is reported to impact the stomal conductance of plant leaves, thus causing a temperature rise. However, the temperature difference is still different to distinguish from a normal condition. Overall, thermal activities can be another dimension in the detection of gas leakage.

1. Experimental Program

1.1 Field test setup

Field tests to simulate underground gas leakages were planned in an off-campus open field (37.957856, -91.788070) as pinpointed in Figure 3.1. Four rectangular trenches are labelled with two control trenches (designated as T-control1 and T-control2) without any treatment and two trench configurations for gas treatments (designated as T-treat1 and T-treat2). Each trench is 60 ft long, 8 in wide, and 3 ft deep. Two parallel trenches are spaced 10 ft to eliminate their potential interference in gas diffusion. All trenches are refilled consistently with a few layers of materials before sods (patches of grass) are placed to ensure that the grass can grow under the same circumstance. The semi-circle area is enclosed by a fence to prevent trespassing and protect any trespassed people from injuring associated with the gas leakage.

Figure 3.2 displays the vertical profile of each 3-ft deep trench. The trench is refilled in five layers. From top to bottom, the five layers are moss sods, backfill soil, overlay gravels, two side-by-side 4 in. perforated PVC pipes, and base gravels. The pipes are perforated along the lengths to ease the release of gas. The gravels on top of the pipes are placed to prevent the blockage of the holes on the pipes and also ease the gas diffusion.

Figure 3.3 illustrates the entire process and steps from trench digging to sod placement, starting on August 29, 2021. Before excavation, the ground surface was first labelled for the location of trenches. Then, the marked trench area was excavated and refilled with base gravels to make a flatbed of the trench before two parallel PVC tubes were placed side by side along the direction of the trench. Since fine soil particles of top backfills would potentially penetrate through the holes on the perforated PVC tubes, potentially making the gas diffusion path uncertain, the PVC tubes were overlayered with another 3 in. gravels. Next, the excavated soil was back filled into the open trench to 2 in. below the original ground surface. Finally, moss sods were customized to fit into the 2 in. deep space on the top of all four trenches.

The perennial moss sods on the top of four trenches were cultivated under the same condition to eliminate the variation of aging effects during field tests. The control trench and one separate moss sod are shown in Figure 3.4. The fresh moss sod acclimates the local environment for at least one month to allow for a full development of the root system. Only when the grass reaches a stable state can the field test start to prevent the unreal impact on the grass itself when compared with real-world applications in pipelines.

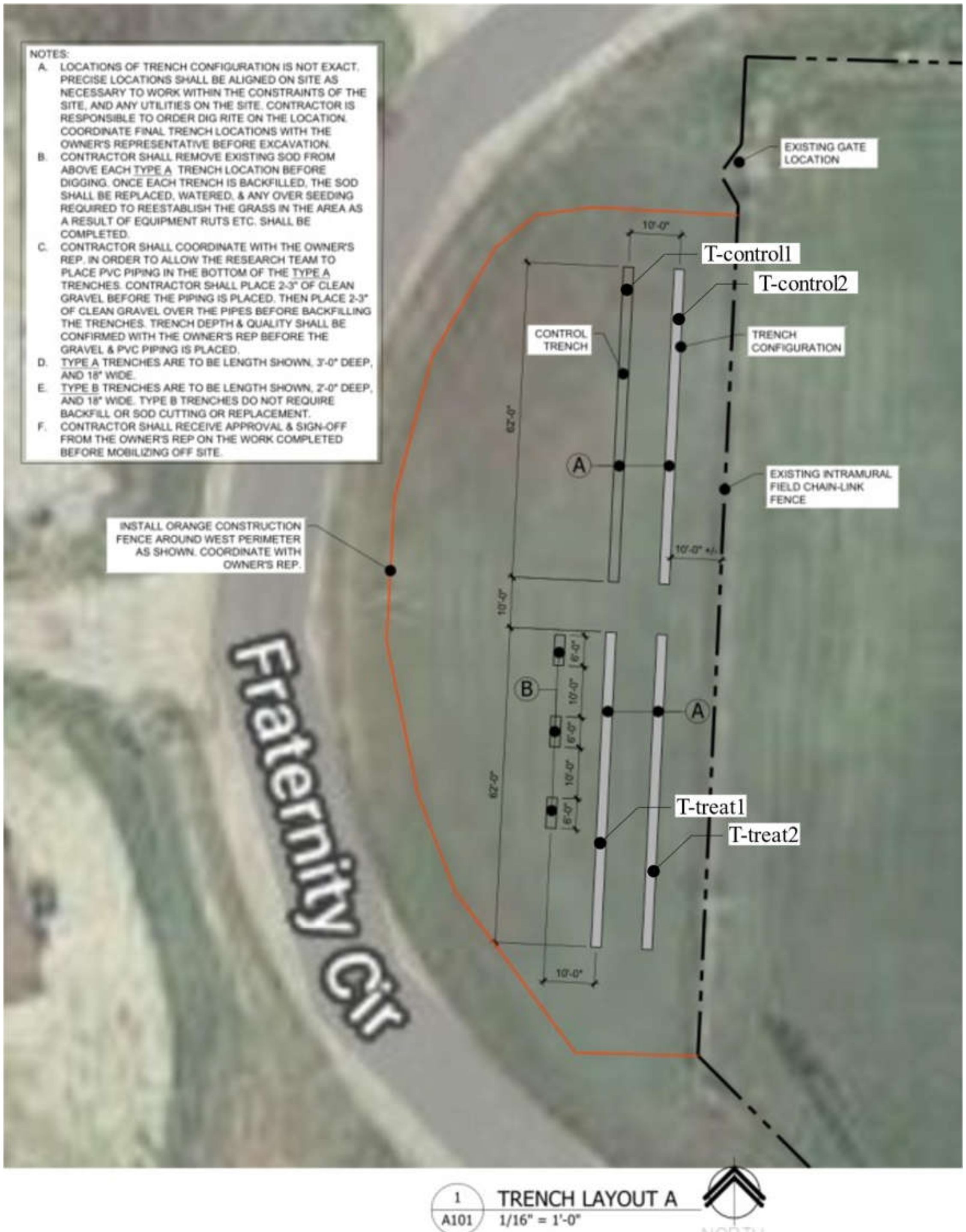

Figure 3.1 Configuration of four pipeline trenches on the test site

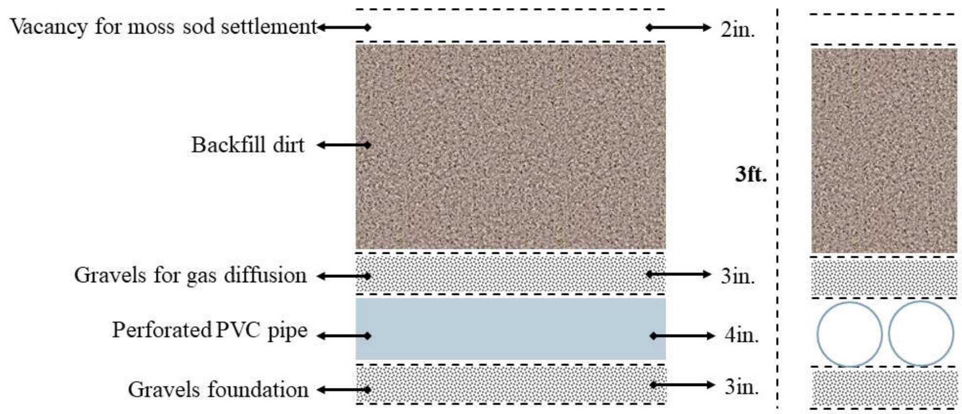

(a) Side view (b) Cross-sectional view

Figure 3.2 Schematics of various layers in each trench

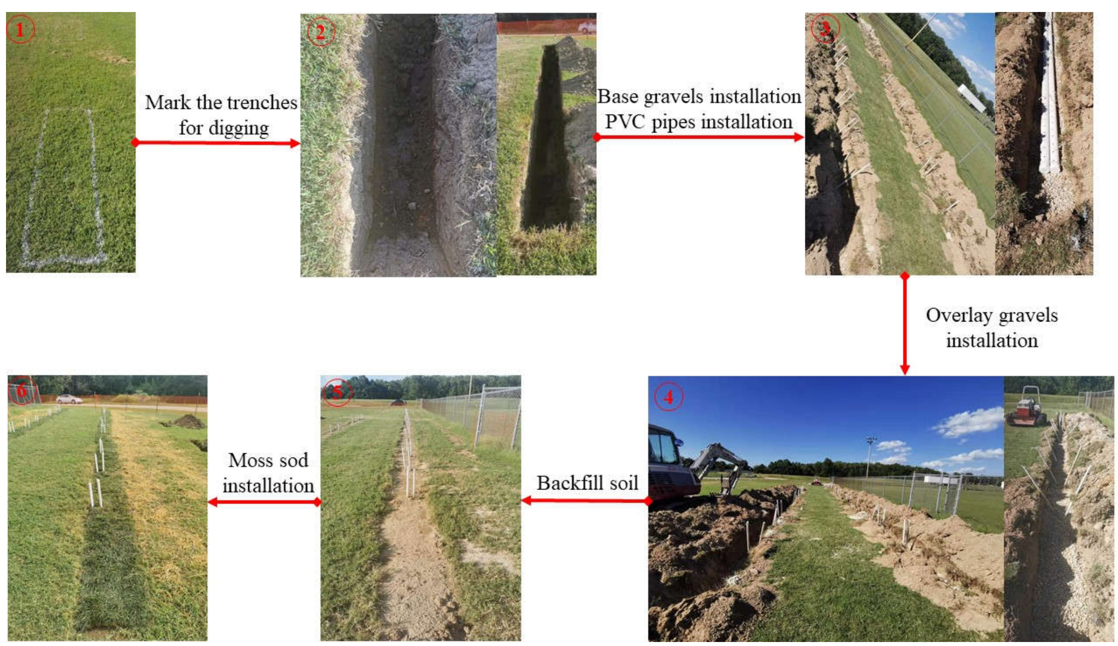

Figure 3.3 Steps in the process of trench excavation, pipeline installation, and grass placement

(a) The control trench (b) A patch of moss sods

Figure 3.4 A view of moss sod placement

Figure 3.5 shows the field test setup. The grasses in all trenches were trimmed one month before methane gas was supplied to allow suffcient time for its growth and to ensure that all the grasses were approximately at the identicial condition. For the gas supply, cylinders of 99% chemical purity methane gas (CH_4) were purchased from Airgas. The flow rate of the gas supply was controlled by the methane gas regulaor and the outlet presure was set to 10 psi in the current study. A transpaent vinyl tube was used to connect the gas cyliner with the underground pipe as shown in Figure 3.5 to deliver methane gas. Each underground pipe has three inlets from which gas was delivered alternately to ensure it was evenly distributed along each trench.

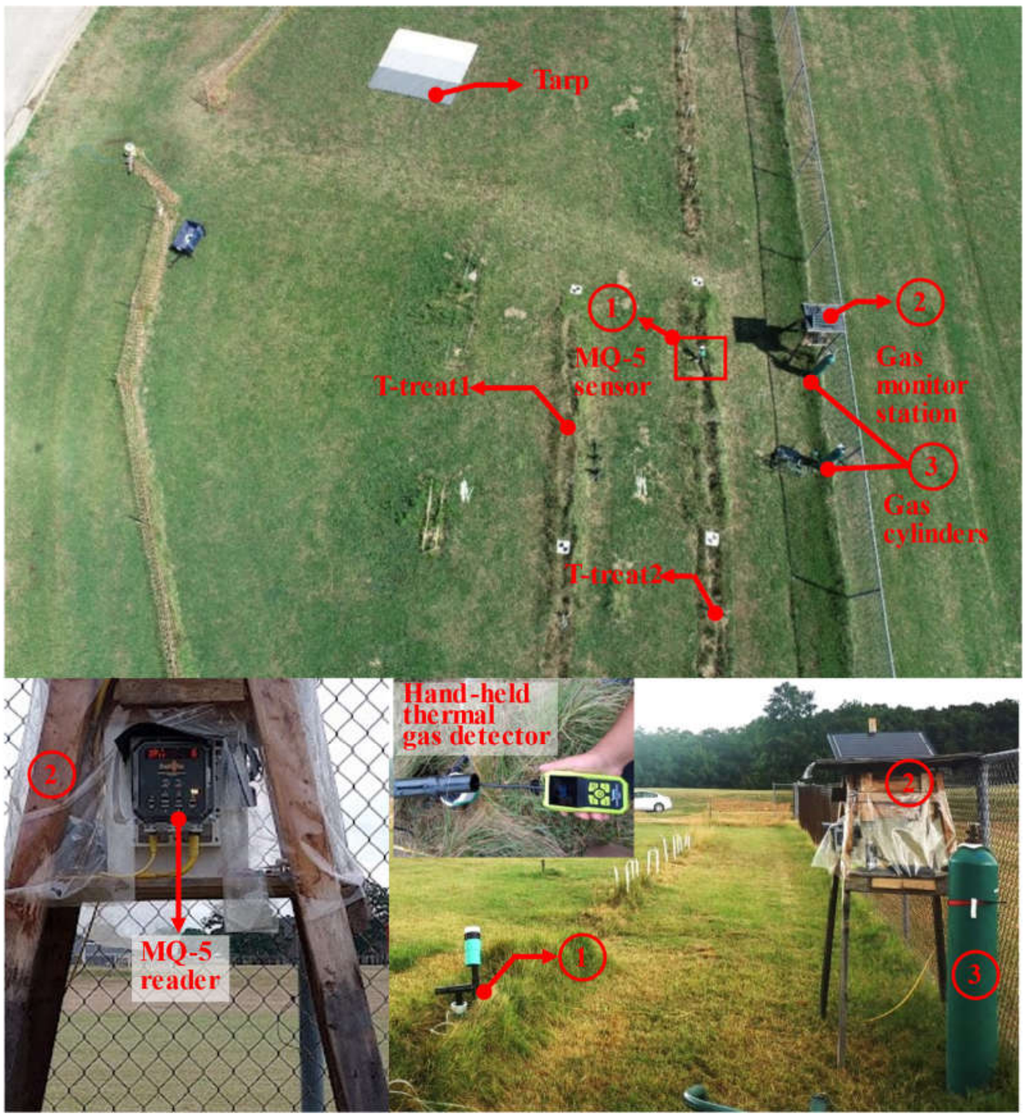

Figure 3.5 Methane gas leakage simulation setup

The methane gas concentration on groud surfaces of the test trenches was measured using a thermal gas detector, which enables a detection of concentration from 50 ppm to 50,000 ppm. In addition, gas leakage concenration on the treated trenches was monitored by a MQ-5 methane gas sensor for 10 hours per day during the test period. The gas concentration was collected every 5 minutes. A gas concentration monitoring station was established on site to facilitate continuous measurements and then the integrated wireless data transferring system store the logged data into cloud for easy remote access.

Once the ground setup was completed, the grass trenches within the test field was periodicallly monitored by the UAS including a hyperspectral camera to record the health condtion. The DJI M600 drone as illustrated in Figure 1.9 was used to monitor the field since the first day of the grass acclimation till the last day of the expected test so that the evolution of the grass conditions can be fully reflected. The drone was remotly connected with a control unit at the groud station. The periodical drone scanning is illuatred in Figure 3.6. The flying route was specifically designed for this test to ensure that all the test trences can be captured with a good imaging condition. The flying altitude was set to 24 m to avoid the any barricades whthin the scanning field. The parrallel overlapp between two parallel paths was set to 40% as suggested by the flying instruction by Headwall Photonics Inc. The flight speed was set to 1 m/s in accordance to the camera exposure configuration to avoide any imaging extension or compression in the flying direction. The route design as completed in a commercial software UgCS also enables a remote control of the drone. Before take-off of the drone, the integrated hyperspectral camera was calibrated by collecting the dark current reference. Moreover, a spectralon (white board) was used to determine the appropriate exposure time to avoid over exposure. As the field scaning was performed around noon to guarantee the quality of solar radiation, the exposure time was set to 4.5 ms and may be alterated accoding to the weather condition.

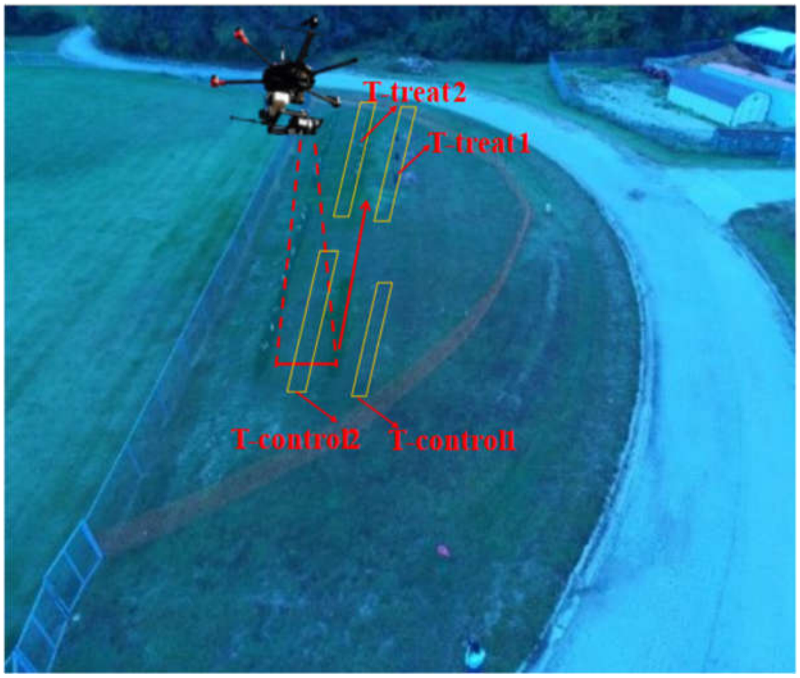

Figure 3.6 Periodical drone scanning of the test field

Figures 3.7(a) and 3.7(b) display the designed and actual flight routes, respectively. It can be seen that there is a long way hovering before the drone enters into the polygon test area to initiate scanning. The hovering is included herein to allow some time for the drone to establish a smooth connection with the ground control units and also for the adaptation of the condition at the designed altitude. Abrupt entrance into the test area may introduce unnessary instability of the drone and then the distoration on hyperpectral imaing. The actual drone flight path deviated from the designed route as indicated in Figure 3.7(b) due to the effect of wind. In the longitude log plot, some apparant changes were identified in the timescale. The starting point of the Altitude changes is a few seconds ahead of Longitute changes though they are well corresponded to each other. This observation indicates that the Altitude change might be a precuresor of the alteration of Latitude.

The hyperpectral camera in this field test is different from the one used in Section IV though both are Headwall Photonic products. Micro-Hyperspec® VNIR E-Series sensor used in this section is specifically configured for manned/unmanned airborne applications. The camera enables 250 bands from 400 nm to 1000 nm with a spectral resolution of 3 nm. The pixel size in the focal plane of sCOMS is 6.5 microns. Based on the above drone test configurations, one pixel can cover the information in a 1 cm × 1 cm square domain as indicated by the UgCS software. The specfication of the hyperspectral camera is given in Headwall (2022).

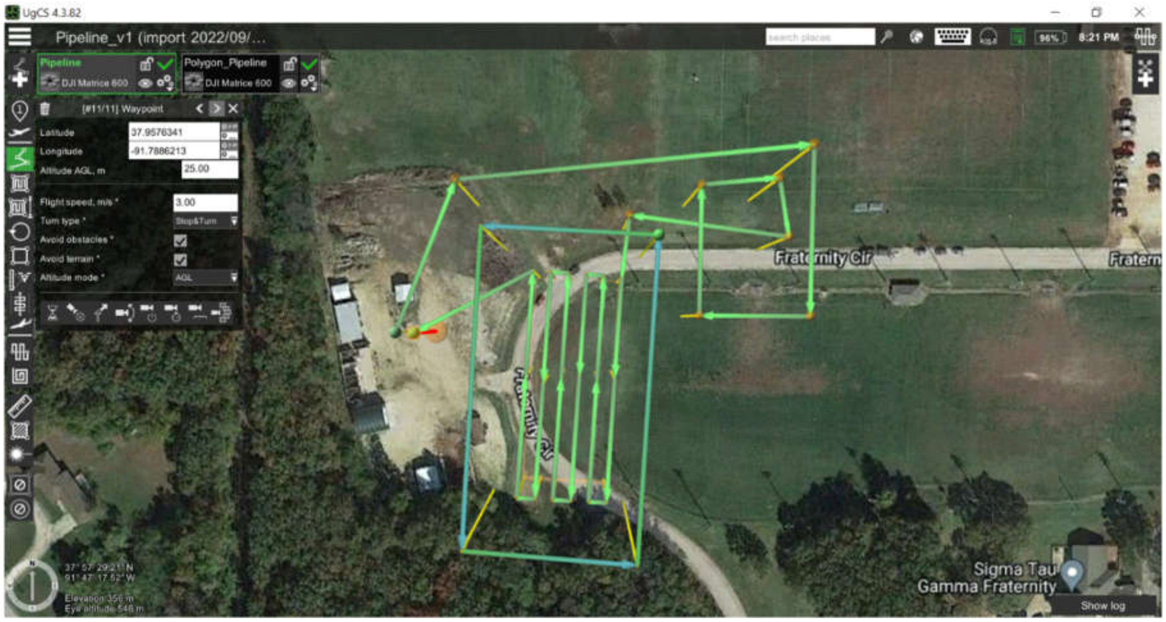

(a) The designed flight route and corresponding configuration

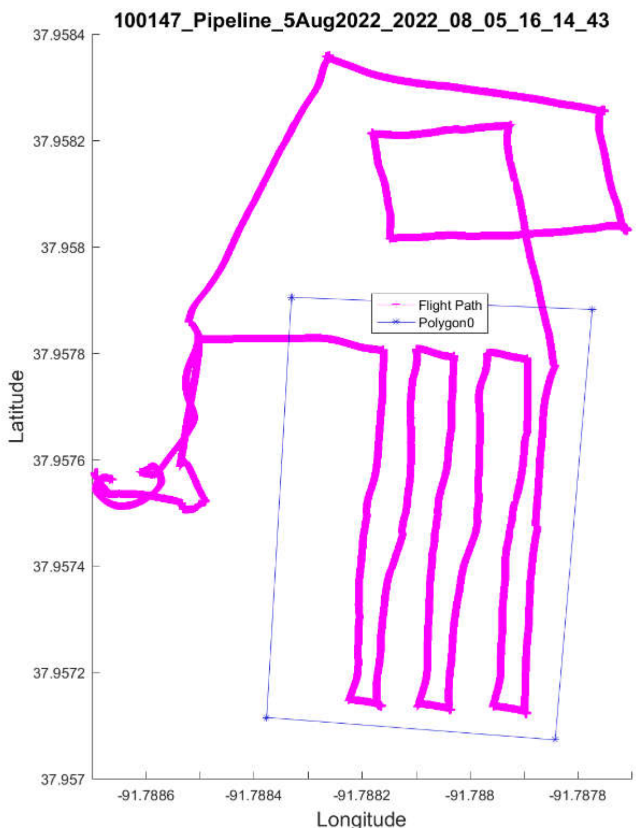

(b) The actual flight route of the scanning on August 5, 2022

Figure 3.7 Drone flight plan in the UgCS software

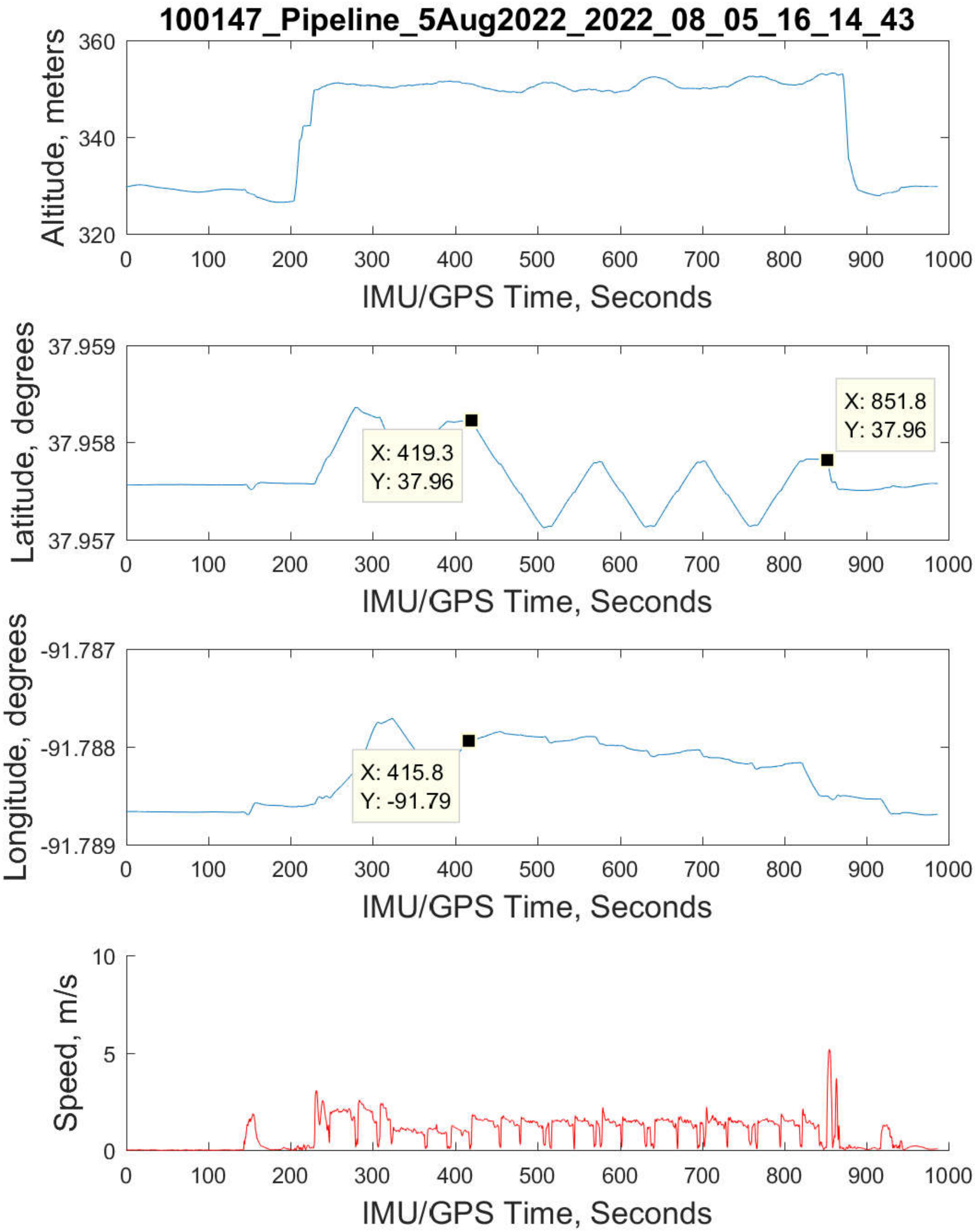

Figure 3.8 The data log of different configuration parameters for the drone scanning on August 5, 2022

1.2 Method

After hyperspectral imaging, spectral signatures were used to evaluate the stress condition of test grasses. There are 250 bands within the VNIR range. It is not practical to include the information from every band because of the intercorrelation between bands within a small range. Some plant physiological effects are reported to be related and can be characterized by the spectra from particular bands. For instance, the change of chlorophyll in plant leaves has been well correlated with band 670 nm. Under stress conditions, plants stimulate their internal negative feedback system to suppress the stress symptoms and thus the changes of some pigments and structural components. To detect the gas leakage from plant stresses with minimal spectral bands, the hyperspectral stress indicators are introduced. Such spectral indices can be more direct to indicate the stress occurrence on vegetations. Some indicators are introduced to reflect the condition of the plant by its corresponding biochemical activities on the plant leaves. Following is a brief discription of seven indicators for the presence of gas stress.

1. Red edge ratio (RER)

   The "Red Edge" refers to an abrupt increase in reflectivity in the near-infrared (NIR) region due to a drop-off in the absorption of Chlorophyll superimposed on a strong NIR reflectivity due to the internal structures of leaves. RER is a ratio of the reflectivity on the NIR side to that on the red side of a red edge. That is,

   $$RER = \frac{R_{700}}{R_{670}} \tag{3.1}$$

   where R is the reflectance at a specific wavelength and its subscript is the corresponding wavelength in nm. For example, Chlorophyll is a function of the red edge and 670 nm is its characteristic absorption wavelength. As such, RER can serve as a quantitative measure of the total chlorophyll content in a leaf and therefore is a general measure of leaf health.

2. Normalized difference vegetation index (NDVI)

   NDVI is a scaled measure of the Red Edge. It is a "normalized" difference between a red wavelength and a NIR wavelength on the short and NIR wavelength sides of a red edge, respectively. Chlorophyll absorbs light strongly and weakly on the short and NIR wavelength sides, respectively. In the latter case, scattering by internal leaf structures dominates the reflectivity of light.

The rationale of NDVI comes from the fact that photons in the visible region of the spectrum have energies sufficient to drive the photosynthesis process, and therefore plant chlorophyll absorbs strongly in the visible region. Otherwise, photons in the NIR region are unable to initiate the photosynthesis and therefore these wavelengths tend to be reflected by plant leaves. For better comparisons across various measurements and conditions, the difference in reflectance is "normalized" by dividing the absolute difference by the sum of the two reflectance values. That is,

$$NDVI = \frac{(R_{800} - R_{680})}{(R_{800} + R_{680})} \tag{3.2}$$

3. Modified normalized difference 705 index (mND705)

Complementary to NDVI as a broad band index, mND705 is a narrow-band index developed for an accurate measurement of the red edge.

$$mND705 = \frac{(R_{750} - R_{705})}{(R_{750} + R_{705} - 2 \times R_{445})} \tag{3.3}$$

In comparison with the NDVI, the mND705 index is also less sensitive to the difference in leaf surface across species. By subtracting the reflectance at 445 nm (where most leaf pigments absorb strongly) from the values on either side of the red edge, the index corrects the specular reflection from shiny leaf surfaces.

4. Photochemical reflectance index (PRI)

The photochemical/physiological reflectance index (PRI) can be used to measure the efficiency of photosynthesis or light use efficiency for a plant in real time. The PRI is inversely proportional to the instantaneous photosynthesis activity.

Plants must expend energy and nutrients to generate the structures involved in photosynthesis. Thus, there will be a limit to the amount of light that a given plant can use in the photosynthesis process. Damage to the chlorophyll can occur if light is absorbed more quickly than the energy can be used. The energy from excessive absorbed light is dissipated through changes in the Xanthophyll pigments, which are associated with an increase in reflectivity in the green around 531 nm. If the reflectivity in this region increases, the plant becomes less efficient in using the incoming light. PRI is calculated from the normalized difference between reflectance in the Green (531nm) and Yellow (570 nm). That is,

$$PRI = \frac{(R_{531} - R_{570})}{(R_{531} + R_{570})} \tag{3.4}$$

5. Water band index (WBI)

The water molecule has a strong absorption feature (band) in the NIR at 970 nm. The higher the water content in plant tissues, the stronger the absorption at this wavelength. By dividing the reflectance at this water band by the reflectance at a nearby wavelength (900 nm) outside the water band, a quantitative measure of the water content is obtained. The band 970 nm is used because the reflectance in this range is hardly influenced by the status of plants. That is,

$$WBI = \frac{R_{900}}{R_{970}} \tag{3.5}$$

6. Chlorophyll (Chl)

Chlorophyll is the green pigment responsible for absorption of light that drives the process of photosynthesis. Chlorophyll absorbs strongly in the blue and red regions of the visible spectrum. But it reflects green light, which is why plants appear green. Chlorophyll does not absorb much in the NIR, leading to the "Red Edge" in the reflectance spectrum of plants. A Modified Chlorphyll Absorption in Reflectance Index (MCARI) is introduced as follows.

$$MCARI = (R_{700} - R_{670}) - 0.23 \times (R_{700} - R_{550}) \frac{R_{700}}{R_{670}} \tag{3.6}$$

Most of the nitrogen in plant leaves is contained in chlorophyll molecules. Therefore, the nitrogen and chlorophyll content of a leaf are closely related. In conjunction with measurements from the other indices, the MCARI index can inform decisions about the amount of nitrogen fertilizer to be applied to plants.

7. Carotenoid reflectance index (CRI)

Carotenoids are pigments in plants that produce bright yellow, red, and orange colors. They function in the process of light absorption and protect plants from the harmful effect of too much light. Weakening vegetation contains increasing concentrations of carotenoids relative to chlorophyll. Therefore, CRI is one measure of stressed vegetation.

$$CRI = \frac{1}{R_{510}} - \frac{1}{R_{550}} \tag{3.7}$$

The value of this index often ranges from 0 to 15. The common range for green vegetation is 1 to 12. This index uses reflectance measurements in the visible spectrum to take advantage of the absorption signatures of stress-related pigments.

2. Results and discussion

The spectral signatures were retrieved from the control and test trenches to detect the change in spectral range due to gas leakage. Stress indicators were mapped over the test trenches to locate the overall stress distribution of the methane induced stress. A validation biochemical experiment was executed in lab to validate the stress indicators. Additionally, the thermal images were analyzed to support the detection and location of the gas leakage by identifying the thermal difference between the control trenches and the methane affected trenches.

2.1 Spectral indicator mapping

Figure 3.9 demonstrates the mapping of a hyperspectral stress indicator (HSI) used in this study. In the hyperspectral data cube in Figure 3.9, three example pixels are selected near a trench and labelled by squares in red, green, and blue colors, respectively. Their spectra are presented with two bands (670 nm and 700 nm) marked. The stackable layers corresponding to the two bands are sliced from the cube to give features in those two bands only. The RER index for each of three pixels can be calculated from Eq. (3.1). When all the pixels in the two stackable layers are considered, a RER map can be generated as illustrated in Figure 3.9.

To demonstrate the presence and progression of grass stress in a treated trench with cumulative methane applied over 106 days, Day 0 and Day 50 screenings are compared in Figure 3.10. Figure 3.10(a) shows seven indicator mappings of grasses before they are treated with methane gas. It can be seen that the treated trench can be easily identified by some of the indicators such as RER and NDVI. Due to the presence of various species of surrounding wild grasses, a clear boundary of the trench can be determined from the HSIs. After 50 days of gas treatment, some changes can be readily observed from the HSI mappings in Figure 3.10(b), particularly RER.

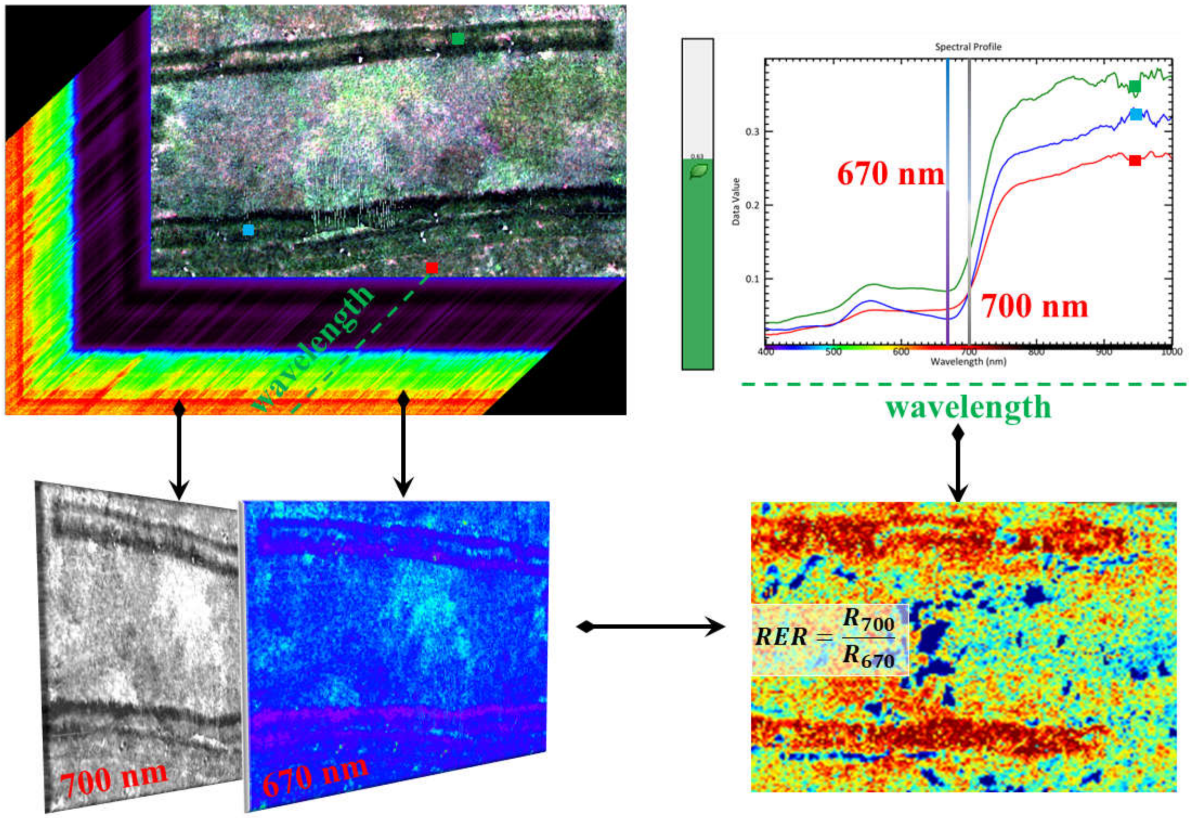

Figure 3.9 Demonstration of mapping a hyperspectral stress indicator (HSI) - RER

Overall, the RER index shows a significant increase for the two gas-treated trenches (T-treat1 and T-treat2) in comparison with one control trench (T-control1). The increase is also observed in NDVI and mND705. However, the WBI displays a negligible difference between the control and gas-treated trenches. The WBI indicates that the water content on the grass may not change significantly due to the stress symptoms. Natural gas stress may not influence photosynthesis activities notably as PRI remains not discernable between T-control1 and T-treat1 (or T-treat2). As photosynthesis involves many biochemical components during the reaction process, the severity of the stress does not induce that much accumulated effect on the plants to decisively change the way of grass energy harvesting. Unlike the complex biochemical process, the pigments in the grass are quite susceptible to the external changes and then altered to counteract the stress effect. The chlorophyll-characterized MCARI shows a great escalation from Day 0 to Day 50. At Day 50, the difference among the three trenches (T-control1, T-treat1, and T-treat2) is not visually obvious as all three have reached the maximum in the color scale of MCARI. In contrast, the CRI shows a decrease from Day 0 to Day 50. Carotenoids are the secondary pigments in grass and CRI demonstrates a sparser distribution on the test trenches. It is an indication that gas stress may influence the carotenoids on plants, though the overall effect is small.

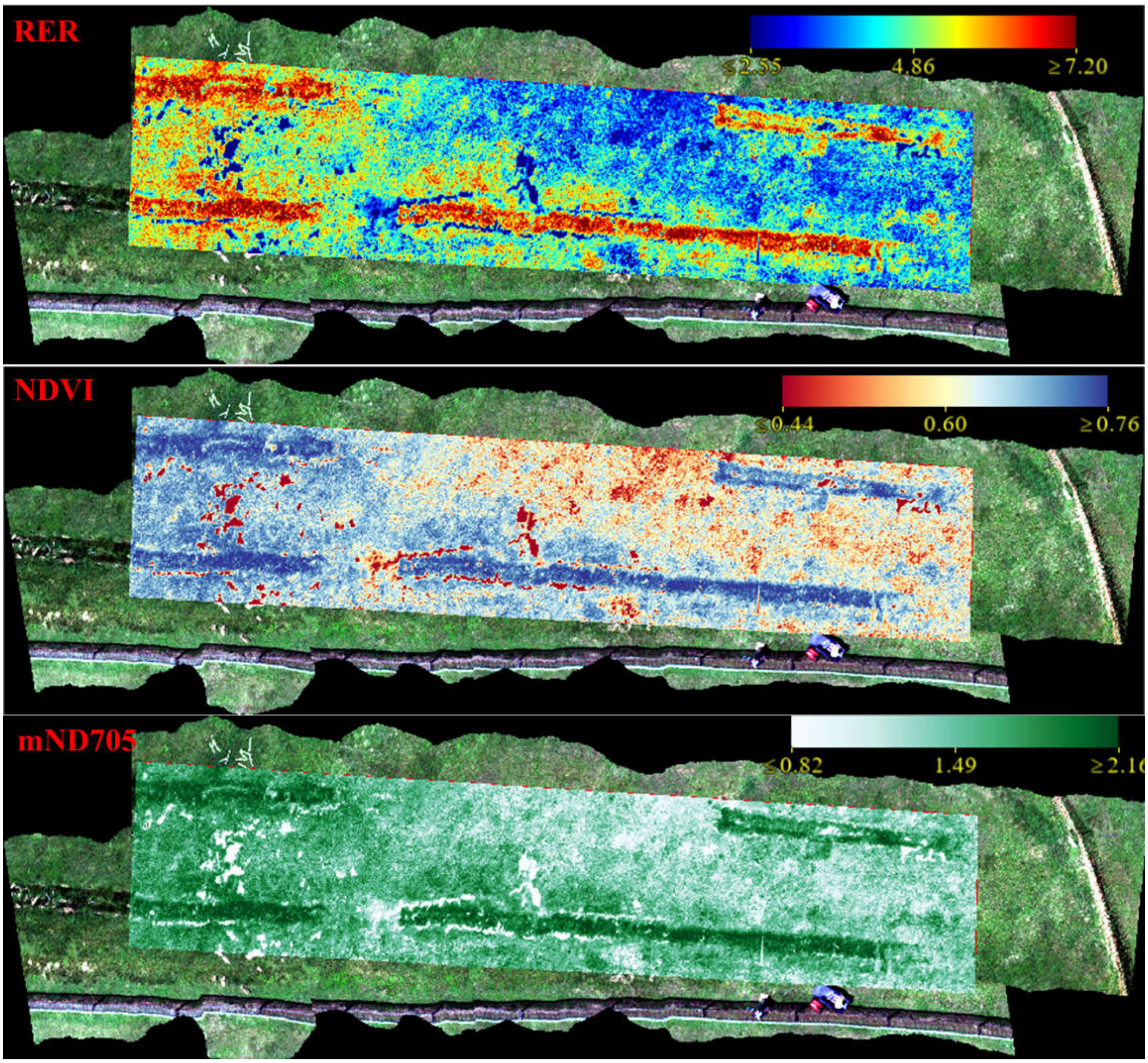

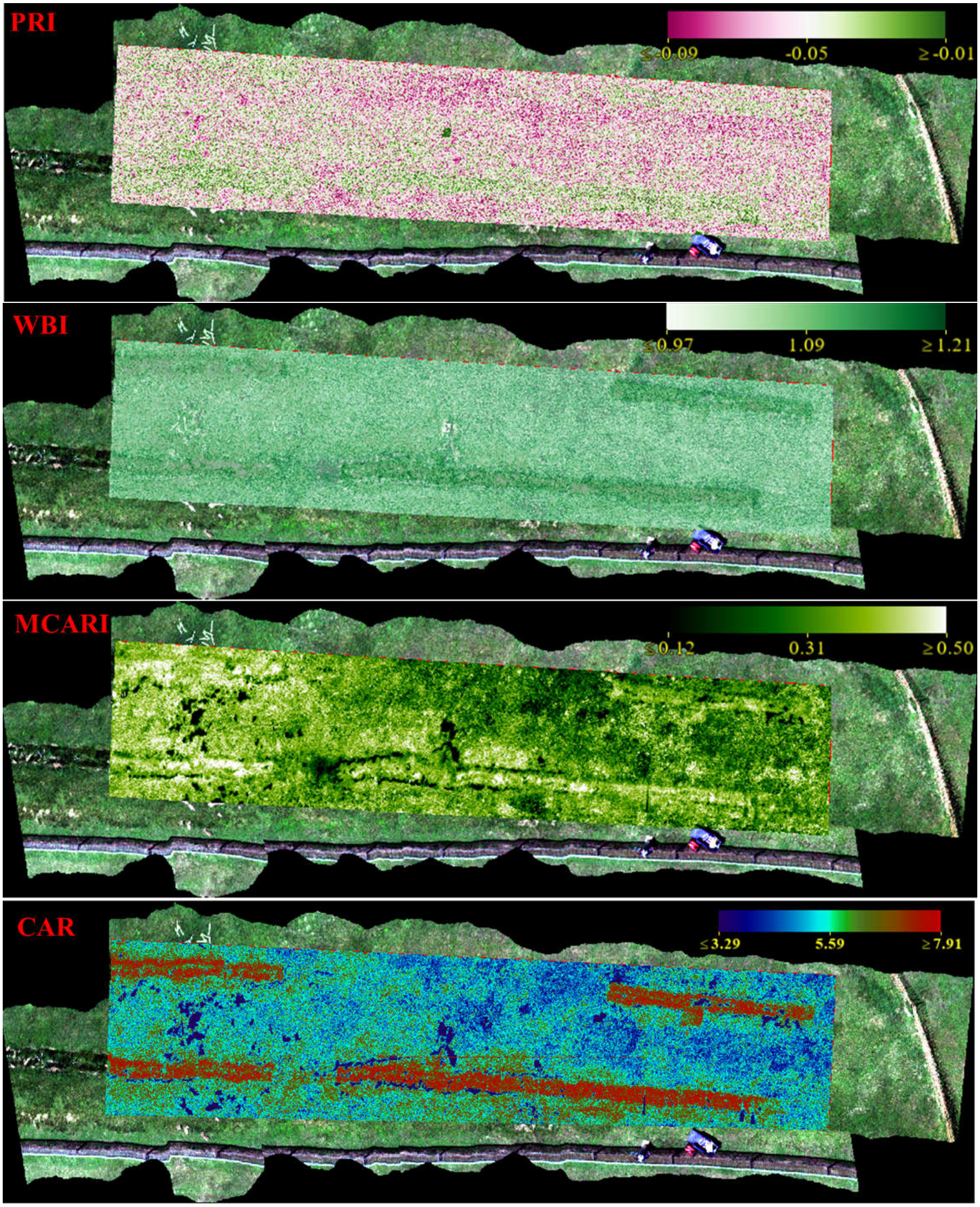

PRI
≤-0.09
-0.05
≥-0.01
WBI
≤0.97
1.09
≥1.21
MCARI
≤0.12
0.31
≥0.50
CAR
≤3.29
5.59
≥7.91

(a) Day 0

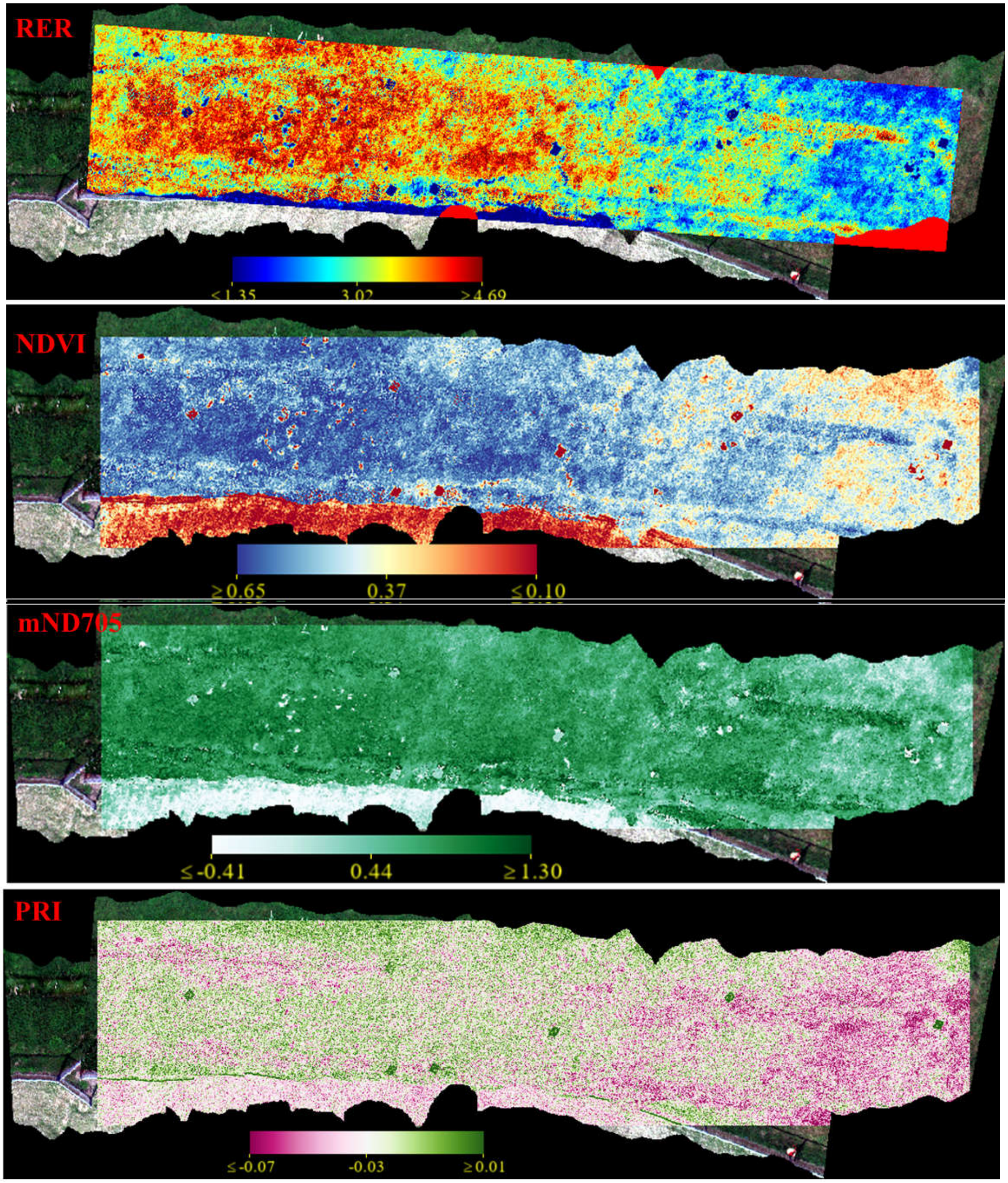
RER
≤1.35
3.02
≥4.69
NDVI
≥0.65
0.37
≤0.10
mND705
≤-0.41
0.44
≥1.30
PRI
≤-0.07
-0.03
≥0.01

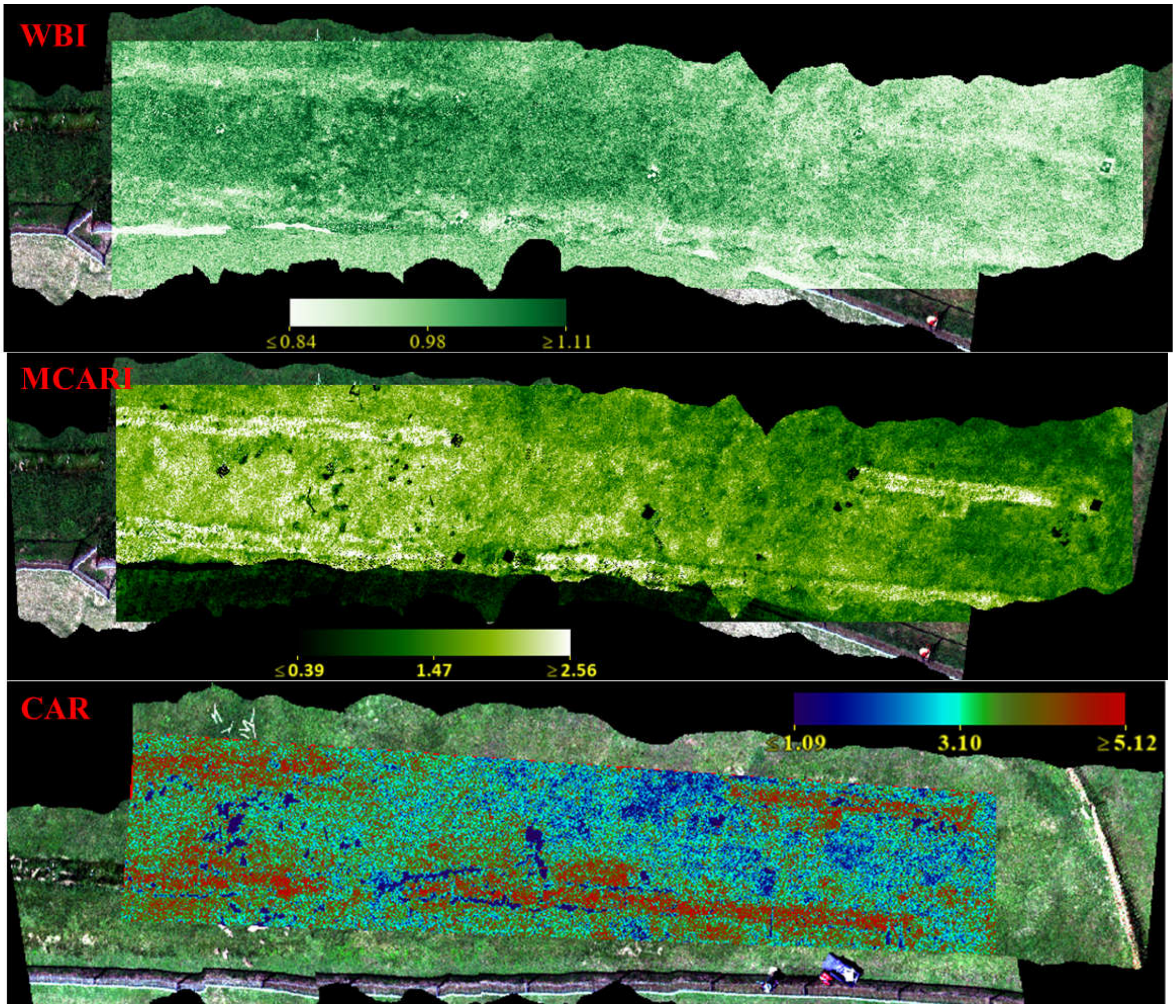

(b) Day 50

Figure 3.10 Mapping of spectral indices to demonstrate stress presence and progress over time

HSI mapping provides a convenient method to locate the difference between control and stressed vegetations. However, this qualitative comparison does not give the degree of the difference; indices within the domain of each trench need to be extracted for quantitative evaluation. Figure 3.11 displays the evolution of each HSI over the test period. Three ‘red edge’ related indicators (RER, NVDI, mND705) show a similar trend. During the acclimation period, some difference can be clearly observed though insignificant. Prior to the fully grown grasses, the three indicators show a moderate decrease before they finally reach a close range on June 8. After the gas treatment, these three indicators remain close for more than one month. The overall changes of the indicators are attributed to natural weathering exposure. Grasses change internally to accommodate the temperature and humidity in different seasons. A slight increase in RER is detected after 35 days of gas treatment while both NDVI and mND705 seem to change little. The mND705 is a narrow band indicator of 'red edge' in comparison with the NDVI, though both do not show any difference in the process of gas treatment. After one more week, the changes can be identified from all three indicators. By then, the cumulative stress effect begins to show consistently the significant difference in RER, NDVI and mND705. After July 24, the three indicators for the test trenches with gas treatment show a dramatic increase and continue this trend to the end of the test on August 23, 2022.

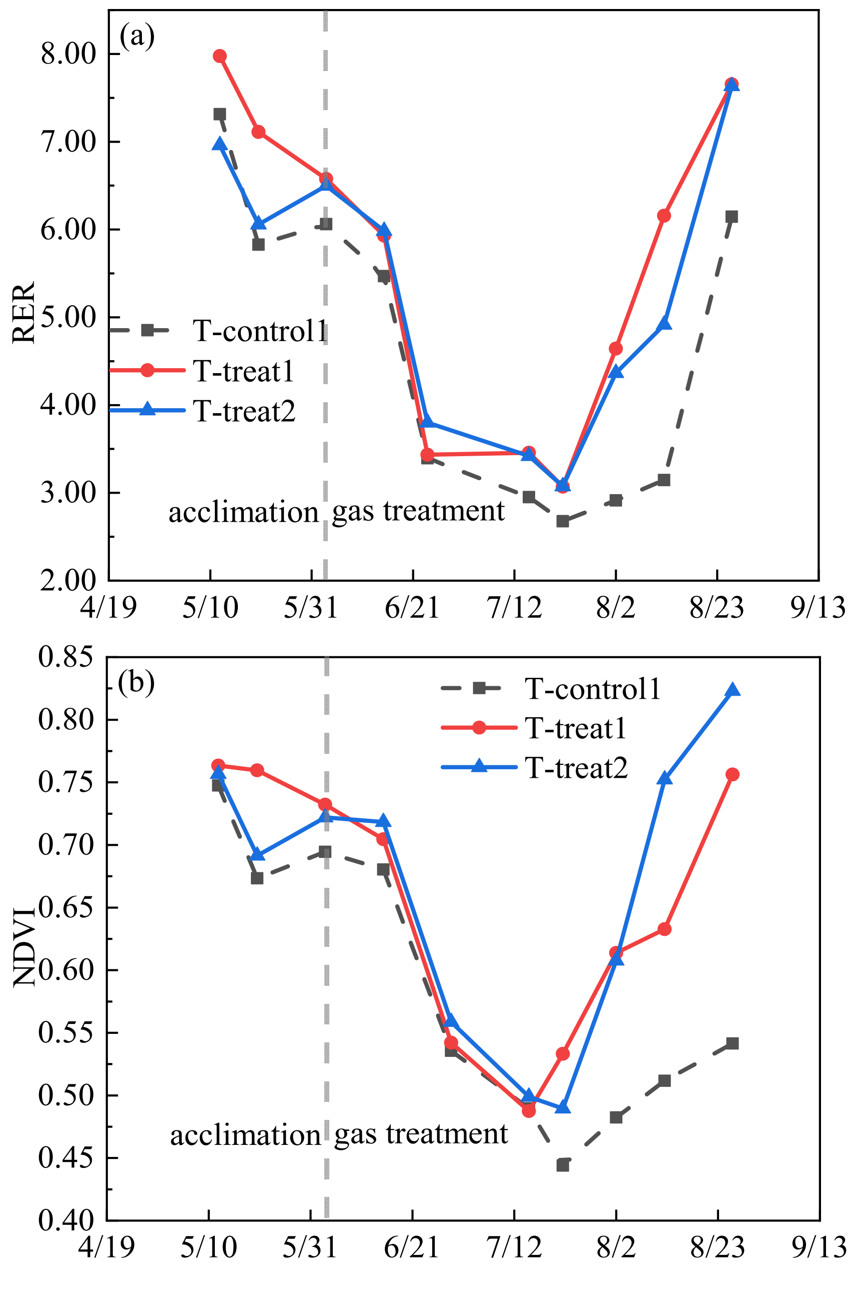

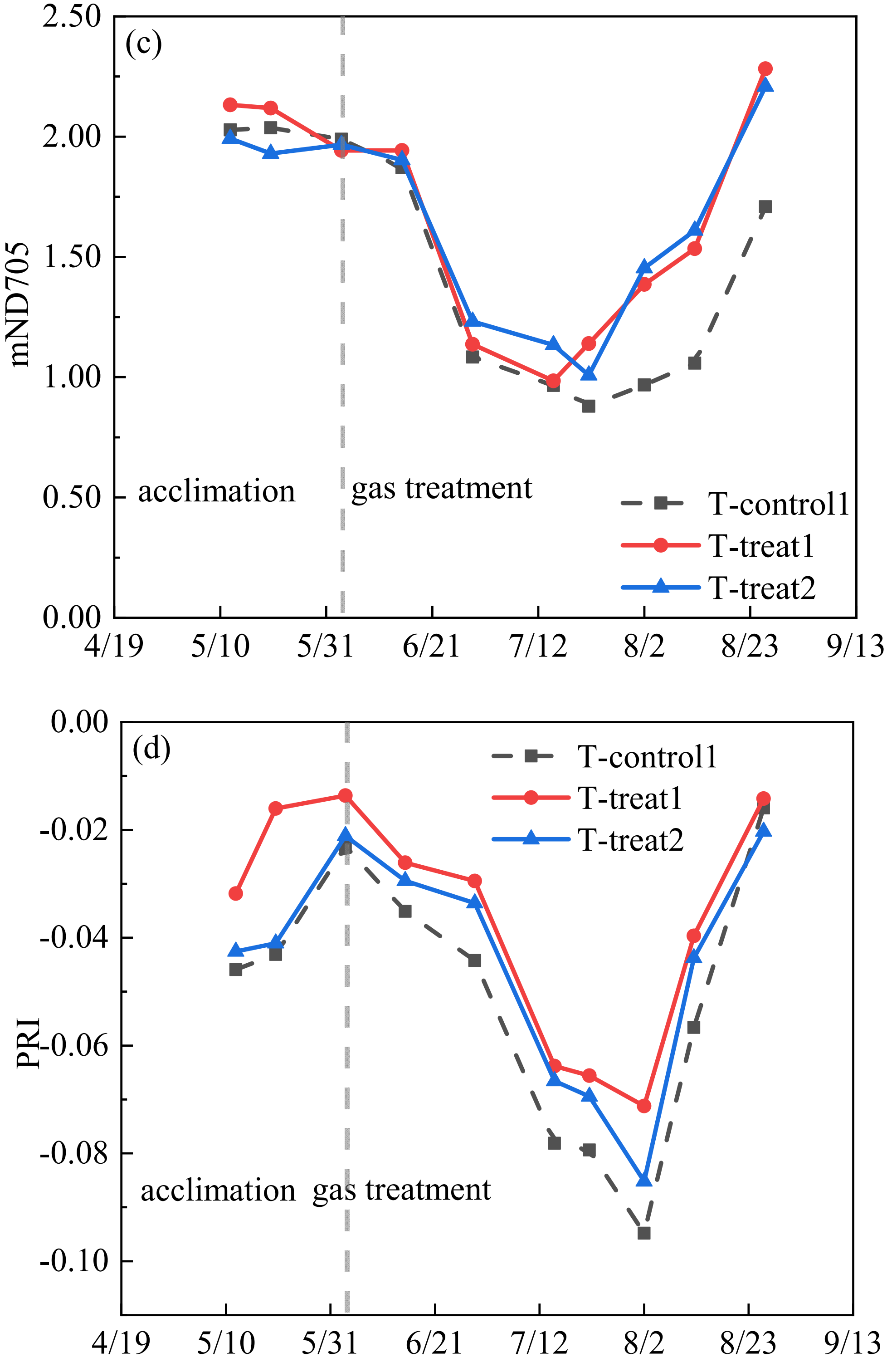

(c)
mND705
2.50
2.00
1.50
1.00
0.50
0.00
acclimation
gas treatment
T-control1
T-treat1
T-treat2
4/19
5/10
5/31
6/21
7/12
8/2
8/23
9/13
(d)
PRI
0.00
-0.02
-0.04
-0.06
-0.08
-0.10
acclimation
gas treatment
T-control1
T-treat1
T-treat2
4/19
5/10
5/31
6/21
7/12
8/2
8/23
9/13

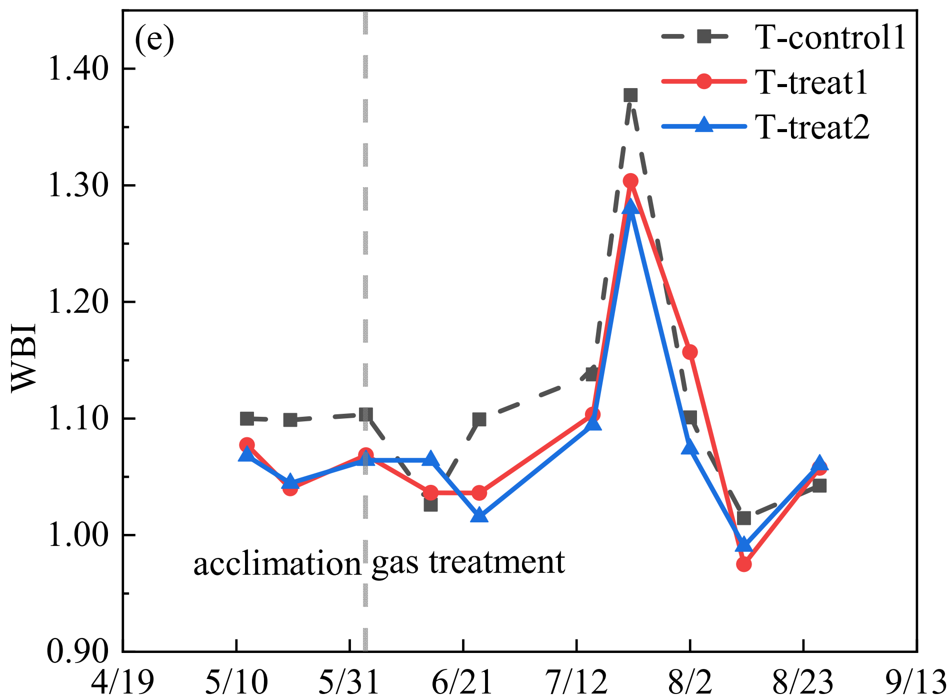
(e)
T-control1
T-treat1
T-treat2
WBI
acclimation
gas treatment
1.40
1.30
1.20
1.10
1.00
0.90
4/19
5/10
5/31
6/21
7/12
8/2
8/23
9/13

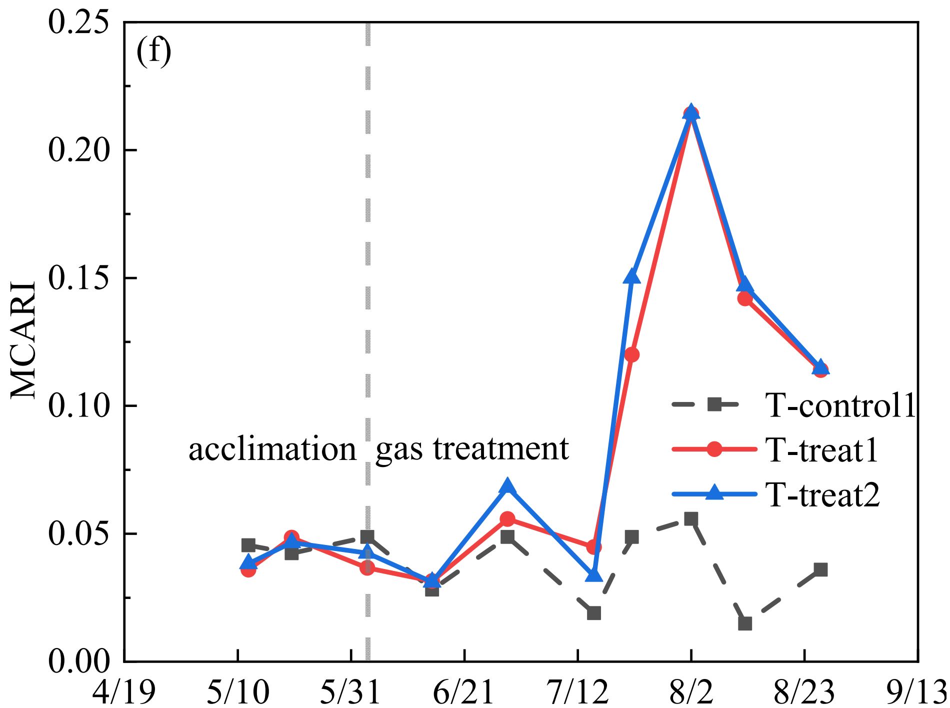
(f)
T-control1
T-treat1
T-treat2
MCARI
acclimation
gas treatment
0.25
0.20
0.15
0.10
0.05
0.00
4/19
5/10
5/31
6/21
7/12
8/2
8/23
9/13

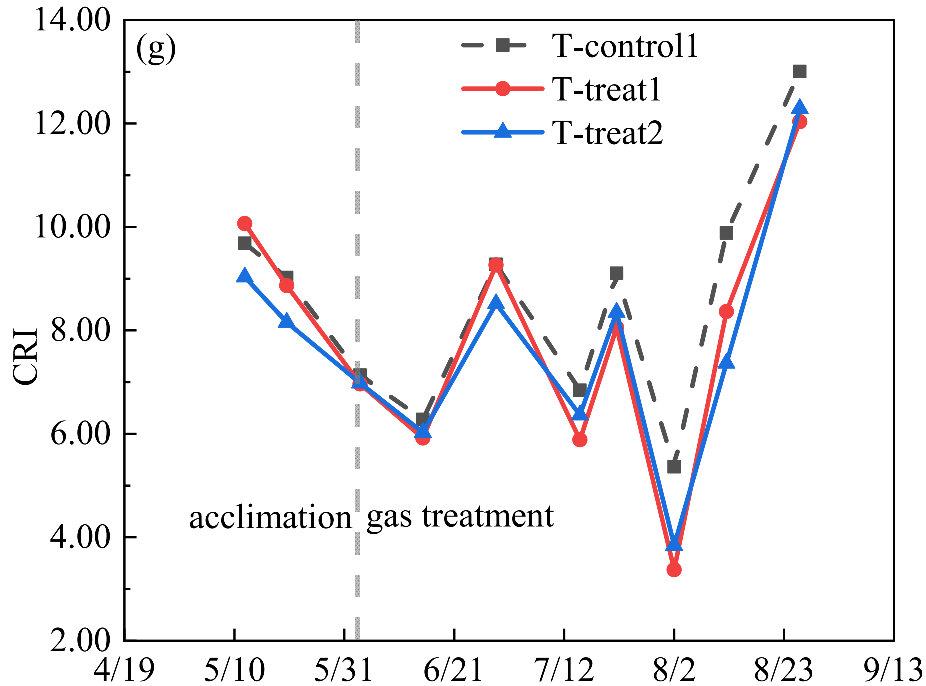

Figure 3.11 The evolution of seven HSIs over time: (a) RER, (b) NDVI, (c) mND705, (d) PRI, (e) WBI, (f) MCARI, (g) CRI. The gray dash line indicates the starting point of gas treatment.

Among other biochemical indicators, WBI does not exhibit too much difference among the three trenches (T-control1, T-treat1, and T-treat2), although grasses experience global changes over time as indicated by RER, NDVI, and mND705. This trend is generally applicable to PRI though the indicators for the two gas-treated trenches are slightly higher than the indicator for the control trench. This is because the complicated photosynthesis process involves many components that are affected with different degrees by the cumulative stress effects. Unlike systematic photosynthesis, plant pigments are very sensitive to the stress because they can annihilate the oxides and suppress the stress effect to prevent a plant from breakdown of its normal internal system. Chlorophyll indicator (MCARI) shows almost no difference among the three trenches before Jun 28. After 20 days of the gas treatment, the MCARI starts to display changes with a slowly increasing trend with the gas treatment. On July 24, however, a huge surge shows up in the MCARI value and the gap appears to broaden along with the progress of the field test. This trend lasts until August 2, 2022, though the gas-treated trenches remain higher at the end of the gas treatment. The drop of the increase trend results from the constant rainfall at that time. Rain allows the plant to recover from the stress status. Another pigment-featured indicator, CRI, as presented in Figure 3.11(g) show small differences between the test trenches in the acclimation period. After nearly one month of gas treatment, a slight decline of CRI is noticed for the gas-treated trenches while fluctuating enormously. The decrease of CRI gradually grows as indicated by the gap between T-control1 and T-treat1 (or T-treat2).

2.2 Conclusions

To demonstrate the presence of gas stress in grasses on the test trenches, seven HSIs are mapped over hyperspectral imagery within the domain of the interest. The mapped HSIs can directly identify the difference between the control and gas-treated grasses. The differences are further quantified to illustrate the degree of gas leakage induced influence and the evolution of gas development through various HSIs. The specific findings are summarized as follows.

1. Mapping of the HSI can facilitate a rapid identification of the changes between different trenches through one-time hyperspectral scanning.
2. Different HSIs exhibit a various degree of effectiveness in detecting the stress occurrence on tested grasses. The chlorophyll characterized indicator (MCARI) is the most sensitive index for stress detection though the 'red edge' related indicators (RER, NVDI, and mND705) also see changes from different gas treatments. Overall, MCARI, RER, NVDI and mND705 all show an obvious increase with a cumulative gas treatment. In contrast, CRI shows a slight decrease over time.
3. The above indicators for the test trenches fluctuate significantly during the field test. It is recommended that the gas-treated trenches be compared with surroundings to demonstrate the induced stress on grasses and the comparative results are used as qualitative measures.

3. Biochemical test for indicator validation

To validate the changes occurred with the previous indicators, a biochemical experiment was conducted to measure the concentrations of plant pigments. Only the chlorophyll and carotenoid were extracted and measured along with the field test. At the same time, grass leaves were measured using an ASD FieldSpec Pro spectroradiometer to obtain ground-truth spectral signatures for derivative analysis.

3.1 Material

The pigments extraction protocol used in this study is referred to Lichtenthaler and Buschmann (2001). Fresh leaves were collected from the test trenches and divided into three replicas for pigments extraction. For every trench, three samples were prepared to understand and minimize random errors. For each measurement, 50 mg leave was cut from the collected leaves and then minced into small pieces in a mortar bowl. The leave tissues were ground with a pestle for 3 minutes with 3 ml spectrophotometric acetone to allow the extraction of pigments. Since the plant tissues may release some acids during the extraction, 10 mg magnesium oxide was added into the mixture to prevent the degradation of chlorophyll prior to a final measurement. When exposed to acids, chlorophyll forms pheophytin that, once accumulated to a large quantity, may cause a shift of absorption peak from approximately 660 nm to nearby wavelengths. In addition, 100 mg fine grade pure quartz sand was used to increase the friction of contact with the mortar bowl during grinding. The extraction solution is the 99.5% spectrophotometric acetone from Thermo Fisher Scientific. The extracted turbid pigments composing of all the previous mixtures are transferred into a 15 graduated glass centrifuge tube. The mortar bowl is then rinsed with 9 ml acetone solvent. In the extraction process, a total of 12 ml acetone was used for each sample. The extract is centrifuged with 400 g in 5 minutes to precipitate the turbid, in which the measurement would be deviated otherwise. Any turbidity and light scattering in the extract solution yields wrong pigment values with particularly too low Chl a/b ratios. This is because the Chl b content in turbid solutions is estimated to be much too high. The total carotenoid x+c levels are incorrect. After the clear extract solution is prepared, a 3 ml is then transferred into a quartz cuvette for a spectral radiometric analysis. The absorption spectroscopy is obtained within 350-800 nm by a Cary 50 UV-VIS spectrophotometer with a spectral resolution of 2 nm. The measurement of the extract is repeated by adding acetone into the clear solution until the absorbance reading around 645 nm falls in the range of 0.3 to 1.0. A typical absorbance spectroscopy is presented in Figure 3.12. In addition, to protect the integrity of the chlorophyll, the whole process is executed in a dim environment as light decomposes pigments.

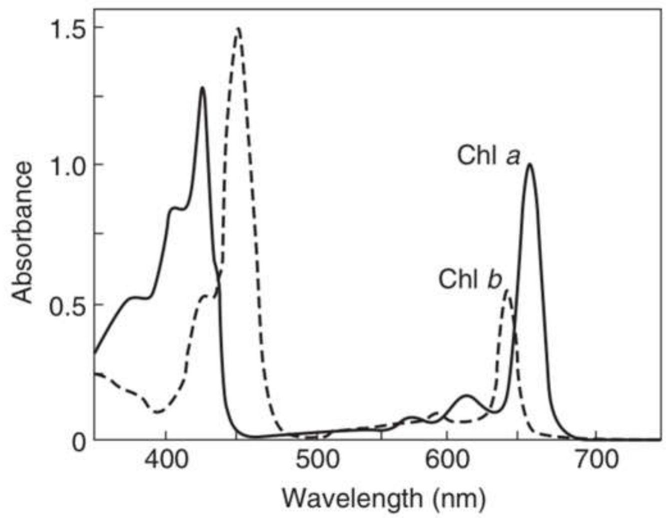

Figure 3.12 Absorption spectra of freshly isolated Chl a and Chl b in diethyl ether (pure solvent). The spectra were measured 40 minutes after extraction from leaves and 3 minutes after eluting the two Chls with diethyl ether from a TCL plate (Lichtenthaler and Buschmann, 2001).

3.2 Method

The pigments can be quantified through absorptance spectroscopy. For 100 % pure acetone, the amount of pigments can be determined from Eqs. (3-8), (3-9), and (3-10). If a precise wavelength like 661.6 nm is unattainable with a spectrophotometer, use a round-off wavelength 662 nm. This approximation is also applicable to other wavelengths.

$$chlorophyll\ a: C_a = 12.25A\_663.2 - 2.79A\_648.8 \quad (\mu g\ per\ mol\ in\ solution) \quad (3\text{-}8)$$

$$chlorophyll\ b: \ C_b = -5.10A_{663.2} + 21.50A_{648.8} \ (\mu g\ per\ mol\ in\ solution) \quad (3\text{-}9)$$

$$Total\ carotenoids: \ C_{x+c} = (1000A_{470} - 1.82C_a - 85.02C_b)/198 \quad (3\text{-}10)$$

The pigments were determined on the leave scale to validate the HSI mappings. Section 2.1 presents hyperspectral results at the plant scale from remote sensing. The hyperspectral reflectance of leaves was also collected between 350 nm and 2500 nm using an ASD Fieldspec Pro spectroradiometer (ASD, Boulder, USA) fitted with a fiber optic probe having a 10º FOV, as illustrated in Figure 3.13. The sampling interval in the 350–1050 nm range is 1.4 nm with a spectral resolution of 3 nm. In the 1050–2500 nm range, the sampling interval is about 2 nm, and the spectral resolution is 10-12 nm. The obtained hyperspectral curve is interpolated by the ASD software to produce readings at a 1 nm resolution. Measurements on the plant leaves were taken between 11:30 am to 12:30 pm to ensure a good solar radiation quality.

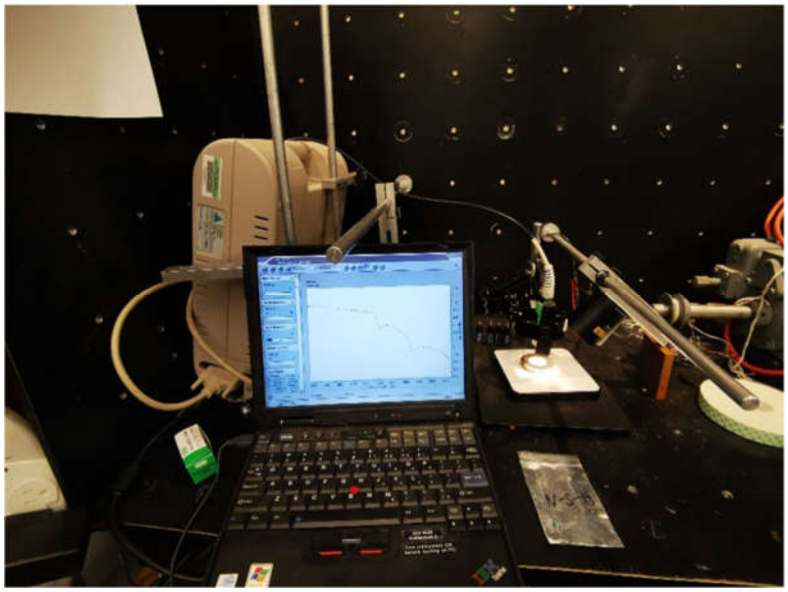

Figure 3.13 Grass leave measurement with an ASD FieldSpec Pro spectroradiometer

For each test trench, 15 leaves were randomly selected, and 10 scans were taken on a single leave. Prior to the vegetation scanning, the spectra collection was optimized by a halon panel that can reflect more than 99% of the incident radiation. Therefore, the subsequent scanning will be normalized with the same object. Since the surrounding changes, the sensor calibration was repeated every 5 minutes and extra calibrations are required whenever the weather condition changes suddenly. The collected spectral signatures are subjected to both first order derivative (FOD) and second order derivative (SOD) to locate the 'red edge' as mentioned in a few HSIs. The red edge is defined as the infection point of a dramatic surge of original spectral curves in a range of 680 -750 nm. Red edge at 725 nm was found to shift to the shorter wavelength due to the influence of stress as the chlorophyll is altered to counteract the stress symptoms.

3.3 Results and discussion

Figure 3.14 presents the measured pigments along with the field test. There are two types of chlorophyll (Chl a and Chl b) with their corresponding concentrations displayed in Figure 3.14(a) and (b), respectively. They follow a similar trend over time. However, Chl a concentration is much higher than Chl b. The chlorophyll pigment increases with time though the control trench (T-control1) only experiences a slow and small change over the entire test period. In contrast, the change in chlorophyll concentration in the gas-treated trenches varies greatly; a greater chlorophyll could occasionally exist even prior to the gas treatment. The higher chlorophyll on the gas-treated trenches exacerbates with the field test but shows a dramatic drop as the field test continues in August 2022. A similar phenomenon was also observed in the HSIs as shown in Figure 3.11 and the continual rainfall at that time alleviates the stress effect as the plant root system is supplied with sufficient oxygen. Carotenoids generally follow a similar trend to that of chlorophyll for both the control and gas-treated trenches. Though all three pigments experience an increase over time, the relative pigment changes are utilized to denote the presence of stress on plants. This is because an absolute amount of pigment is susceptible to random sampling and measurement errors.

Figure 3.14(d) and (e) show a ratio of C_a/C_b and $(C_a + C_b)/C_{x+c}$, respectively. Pigment ratios can directly show the change of plant pigments to reflect the potential effect of gas stress. Prior to the gas treatment on June 8, 2022, the difference in pigment ratio between the control and other trenches is negligible. The fact that both ratios show consistent values identified from all three trenches validates them in practical applications since all the three trenches are not yet treated with gas during that period. After 13 days of gas treatment, the C_a/C_b ratio shows a notable difference between the control and gas-treated trenches. The average ratio of the two gas-treated trenches exceeds the ratio for the control trench by a small growing increment over time. The change in pigment ratio precedes that in HSIs for almost one month. In contrast, $(C_a + C_b)/C_{x+c}$ for the gas treated trenches is significantly lower than that for the control trench even though the differences in ratio for both chlorophyll and carotenoids individually exhibit a large increase over time. $(C_a + C_b)/C_{x+c}$ for the control trench continues to increase gradually over time, while those for the gas-treated trenches drop consistently and significantly after 13 days of gas treatment. The difference between the control and gas-stressed trenches slightly narrows down over time.

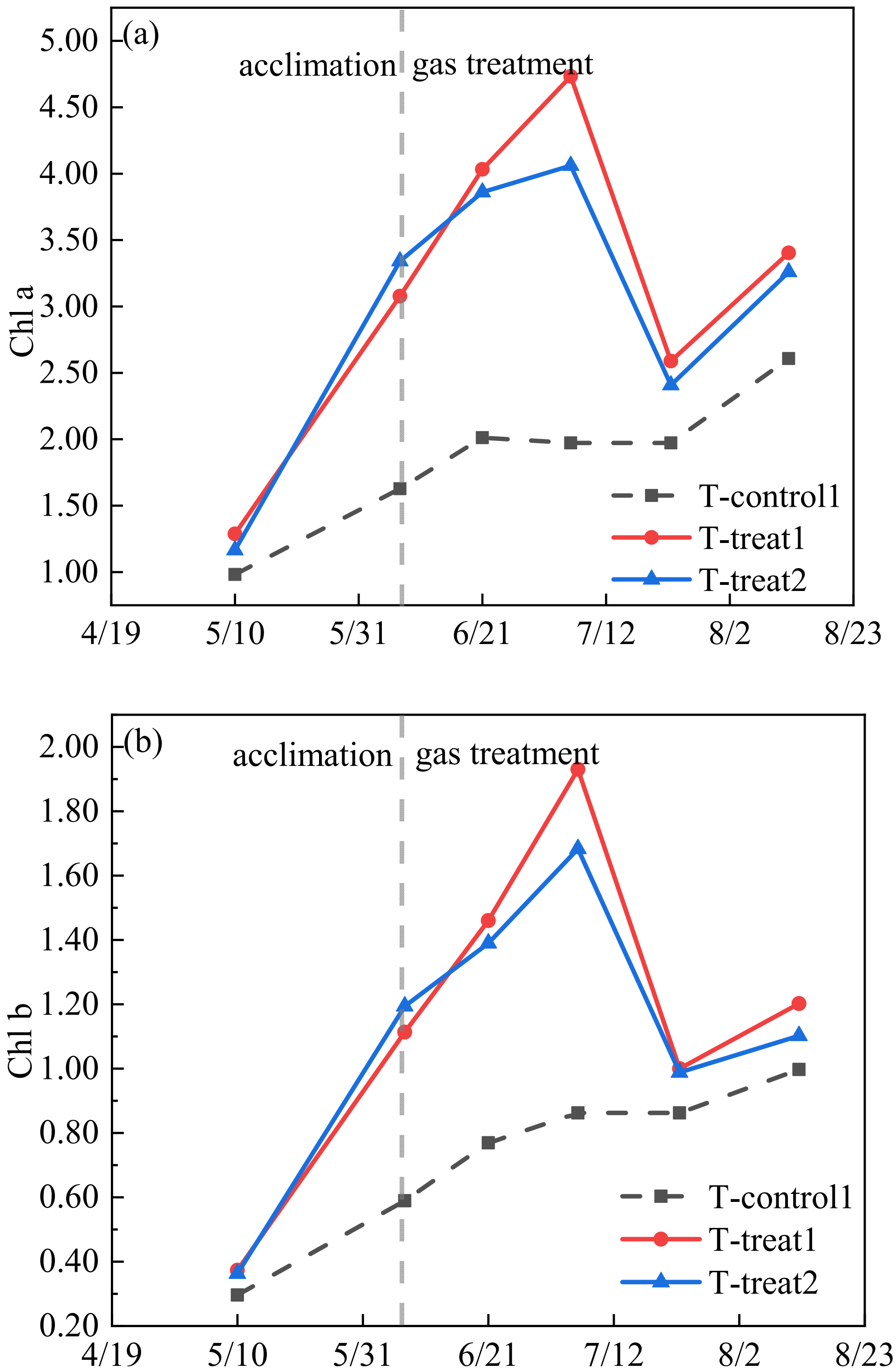

(a)
acclimation
gas treatment
Chl a
5.00
4.50
4.00
3.50
3.00
2.50
2.00
1.50
1.00
4/19
5/10
5/31
6/21
7/12
8/2
8/23
T-control1
T-treat1
T-treat2
(b)
acclimation
gas treatment
Chl b
2.00
1.80
1.60
1.40
1.20
1.00
0.80
0.60
0.40
0.20
4/19
5/10
5/31
6/21
7/12
8/2
8/23
T-control1
T-treat1
T-treat2

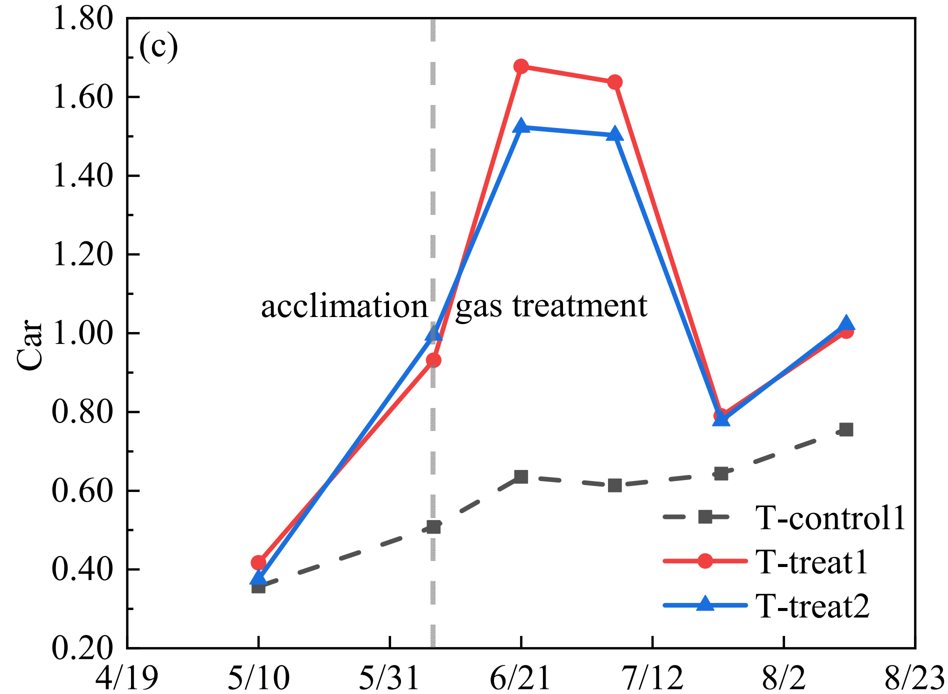

(c)
Car
acclimation
gas treatment
T-control1
T-treat1
T-treat2
1.80
1.60
1.40
1.20
1.00
0.80
0.60
0.40
0.20
4/19
5/10
5/31
6/21
7/12
8/2
8/23

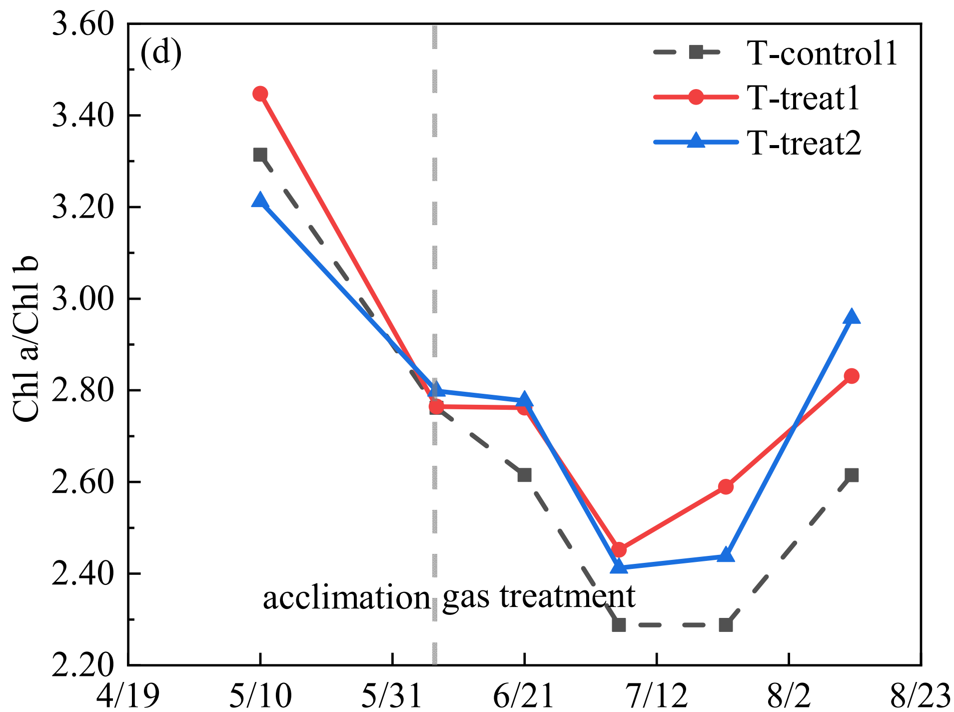

(d)
Chl a/Chl b
T-control1
T-treat1
T-treat2
acclimation
gas treatment
3.60
3.40
3.20
3.00
2.80
2.60
2.40
2.20
4/19
5/10
5/31
6/21
7/12
8/2
8/23

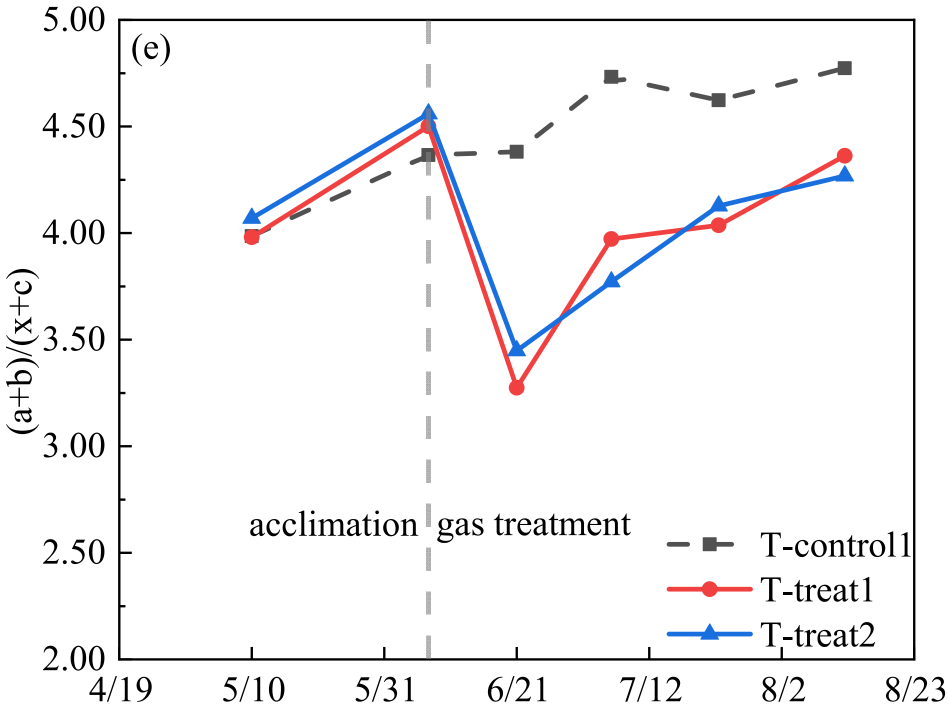

Figure 3.14 The evolution of the plant pigments and the pigment ratios: (a) chlorophyll a (Chl a), (b) chlorophyll b (Chl b), (c) carotenoids (Car), (d) Chl a/Chl b, (e) (a+b)/(x+c). (x+c) denotes a total amount of carotenoids, including xanthophyll and carotenoids.

The spectral signatures obtained by ASD are subjected to derivative analysis to locate the 'red edge' shift in the range of 680-740nm and the peak shift in the blue range. The red edge is determined by the inflection point in the red-light range. Thus, the SOD is performed to locate the position. Likewise, the absorptance peak around 540 nm is identified by the FOS analysis. Figure 3.15(a) displays the four inflection points at approximately 701 nm, 718 nm, 721 nm, and 728 nm developed over time. During the field test over time, the 'red edges' at 728 nm and 701 nm are slightly shifted to the shorter and longer wavelengths, respectively. A similar observation was also reported in a biochemical characterization of gas stress by Smith (2004). This shift is attributed to the change of chlorophyll due to gas treatment applied on the grasses. The wavelength shift around both 718 nm and 721 nm is not obvious. The difference in wavelength shift between the control and gas-treated trenches is difficult to discern. The wavelength featured by carotenoids is presented in Figure 3.15(b). Both global and local wavelength shifts of the absorptance peak around 552 nm are unclear.

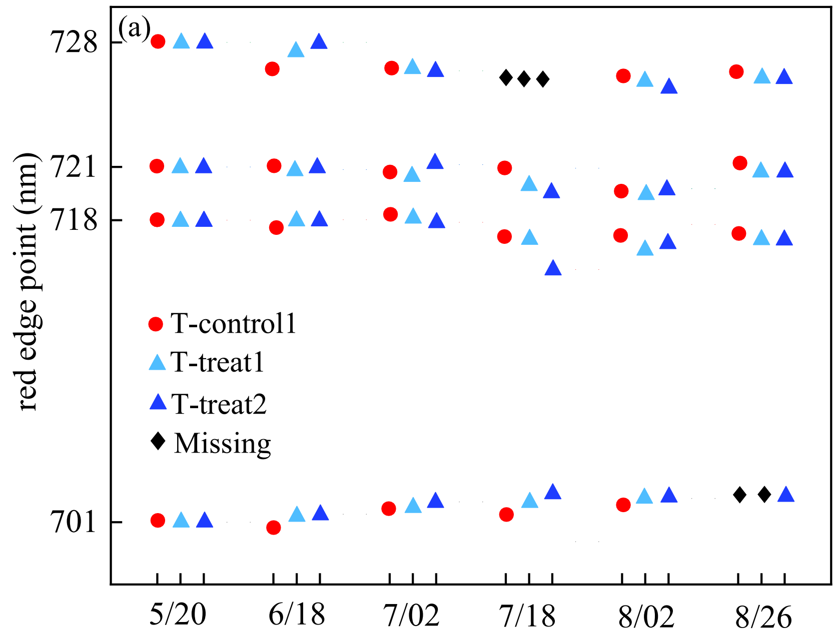

(a) The four inflection points within 680 nm -750 nm as an indication of 'red edge' shift

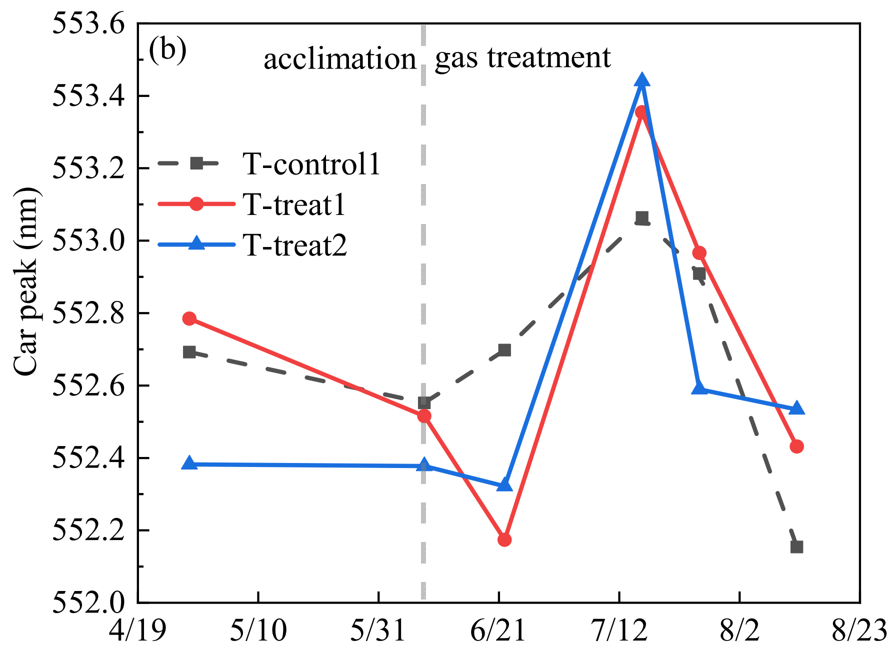

(b) The carotenoid peak shift at 552 nm

Figure 3.15 The spectral shifts based on the derivative analysis of ASD spectra

4. Thermal analysis

Unlike grass symptoms that take a long time to develop under gas treatment, temperature differences surrounding a gas treatment area can rapidly respond to the heat trapped in ground soil as a result of gas leakage. As such, the change in ground temperature is a convenient indicator of heat transfer during gas leakage. In addition to the gas leakage, the test field experiences three forms of heat transfer under sunlight: conduction, convection, and radiation that are heat fluxes through soil materials, air through vertical PVC tubes, and electromagnetic waves, respectively.

Two thermographic images captured around noon on June 8 and July 18, 2022, right after and 40 days of gas treatment, are presented in Figure 3.16. During those test days, the atmospheric temperatures under sunlight were reported to be 68-73 °F and 70-82 °F, respectively. It can be observed from Figure 3.16 that the highest ground temperature recorded on June 8 is approximately 10 °F lower than that on July 18, which agrees well with the difference in atmospheric temperature on those two days. More importantly, the temperature contrast between the trench areas and their surroundings are also much higher on July 18 than that on June 8. This high temperature contrast makes the trench boundaries more identifiable. On July 18, the temperature within the domain of trenches is 10 °F or lower than that in surrounding areas mainly due to the 3-ft deep excavation and gravel placement in the trenches. This contrast remains significant even after the gas treatment may slightly heat underground in the trenches due to warm air flow through the vertical PVC pipes and then horizontal perforated pipes. As shown in Figure 3.16(b), the thermal contrast between the control and gas-treated trenches is also notable mainly due to air circulation in soil through the vertical and horizontal pipes. The gas-treated trenches show a more even thermal emission, revealing a more identifiable trench boundary. On June 8, the thermal contrast between the control and gas-treated trenches is too low to reliably identify the trench boundaries from a first glimpse. The soil in excavated trench areas is consolidated in trenches after approximately nine months of waiting for field tests. In addition, since the vertical PVC pipes stay above the ground surface, grass in the domain of trenches may be longer than that in surrounding areas. This effect has not been quantified in this report.

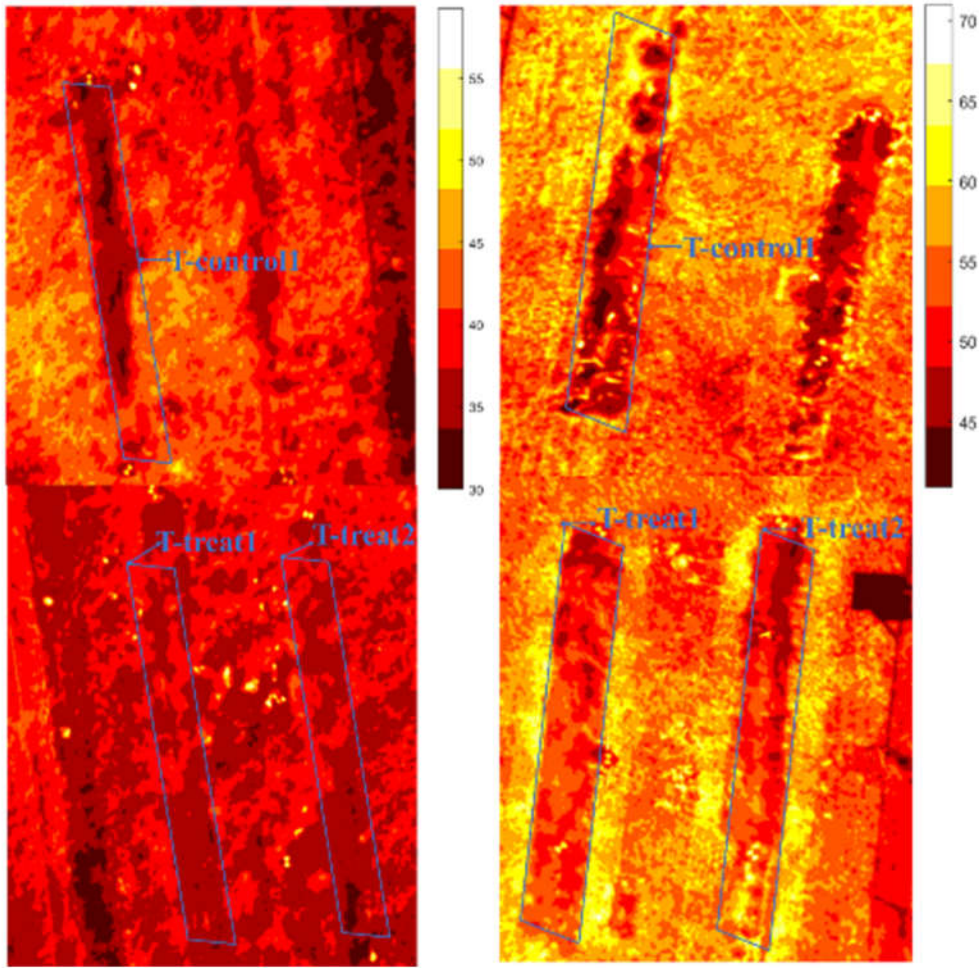

(a) Day 0 (b) Day 40

Figure 3.16 Thermographic images of the test field on two different dates after gas treatment (Unit: °C)

To quantify the thermal contrast between the control and gas-treated trenches, the distributed temperature data within the domain of each trench are analyzed statistically. The (mean ± standard deviation) temperatures of each trench are presented in Figure 3.17. Prior to the gas treatment, the average temperature of the control trench is between those of the two gas-treated trenches. The gas treatment obviously yields a stronger thermal field as opposed to the control trenches. The average thermal difference is approximately 6 °C except 1.5 months into the field test program on July 22, 2022. In the following three weeks till August 12, there seems no difference in thermal emission between the control and gas-treated trenches. This is likely caused by the heavy rainfalls (thunder storms) that were reported on July 17 and August 2, which were five and three days before their respective field measurements on July 22 and August 5, respectively. During that period, the variation in ground temperature is substantially higher than other periods. Note that the field measurement on August 26, six days after the regular rain on August 20 was nearly unaffected.

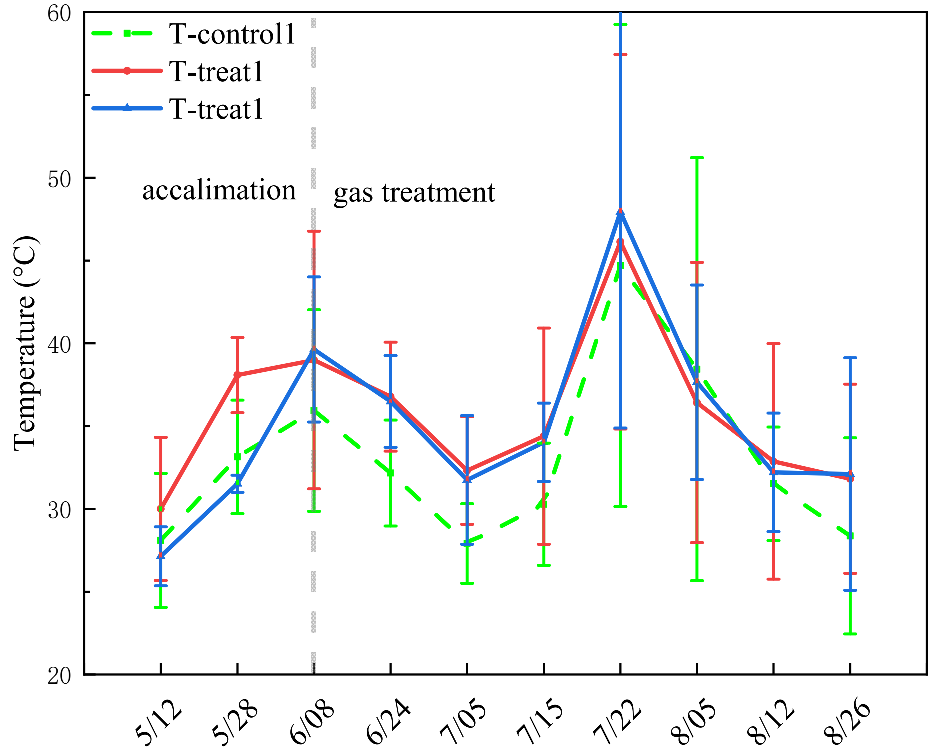

Figure 3.17 The thermal difference between the control and the gas trenches

5. Deep leaning networks for stress identification

Hyperspectral images provide a wealth of information cutting across a wide range of spectral bands. Unfortunately, manually identifying the stress-sensitive features from such complex data cubes is computationally intractable due to the intricacies inherent in the problem. However, previous studies have indicated that state-of-the-art deep learning techniques can come in handy in such situations as they can detect useful features for autonomously classifying and localizing stress areas (Signoroni et., 2019; Chen, et., 2014; Li et., 2019; Audebert et., 2019; Paoletti et., 2019; Yang et., 2018). Many artificial intelligence (AI) techniques have been developed to solve the classification problem as for hyperspectral data. They are derived from the previous computer vison and pattern recognition problems. These methods can be categorized by different factors, from supervised learning (e.g., support vector machine, Naive bayes, and random forest) to unsupervised methods (e.g., K-means clustering and K-nearest neighbor), from statistical classifiers (e.g., multinomial logistic regression, linear discriminate analysis) to the deterministic techniques (e.g., extreme learning machine), from spectral-based methodologies (spectral angle mapper to spatial or spectral-spatial ones (sparse coding). However, the supervised leaning faces changes due to the availability of the sufficient training samples as well as the high dimensionality of the hyperspectral data. In contrast, unsupervised techniques do not require the *priori* knowledge when performing classifications; they optimize the border parameters by the similarities between the input data. To compromise the limitations in supervised leaning, a multilayer perceptron (MLP)-based (Noriega, 2005; Ramchoun et., 2016) deep neural network (DNN) (Sze et., 2017; Miikkulainen et., 2019) is leveraged in this project to distinguish between stressed and non-stressed pixels accurately.

5.1 Material and methods

5.1.1 Deep learning neutral network

An MLP is the simplest form of a neural network consisting of interconnected neurons organized in the form of input, hidden, and output layers. Information flows from the input to the output layer in a feed-forward manner through the connections as shown in Figure 3.18. The input layer takes an input data which is subsequently processed by the intermediate hidden layers through a series of linear and nonlinear operations. Finally, the prediction of the neural network is displayed in the output layer. The input layer in the proposed MLP had 273 nodes representing approximate spectral bands used in this project. In other words, the reflectance values corresponding to each pixel as illustrated in Figure 3.19 are input to the DNN and classified as stressed or non-stressed. The DNN contains five hidden layers comprising 512, 1024, 2048, 1024, and 512 neurons. Each linear layer is followed by a Rectified Linear Unit (ReLU)-based activation (Agarap, 2018), except the last layer where a Sigmoid-based activation (Narayan, 1997) is used. The activation layers enable a DNN to deal with nonlinear relations. The connections between nodes are characterized by weights that are learned through a supervised back-propagation training algorithm (Hecht-Nielsen, 1992; Erb, 1993; Wythoff, 1993; Li et., 2012; Hegazy et., 1994). A stochastic gradient descent-based optimization technique (Amari, 1993; Ketkar, 2017) is used to minimize a binary cross-entropy loss (Ho and Wookey, 2019) between the target and predicted labels. The learning rate is set to 0.001. The model is trained using an NVIDIA A100-SXM4-40GB GPU.

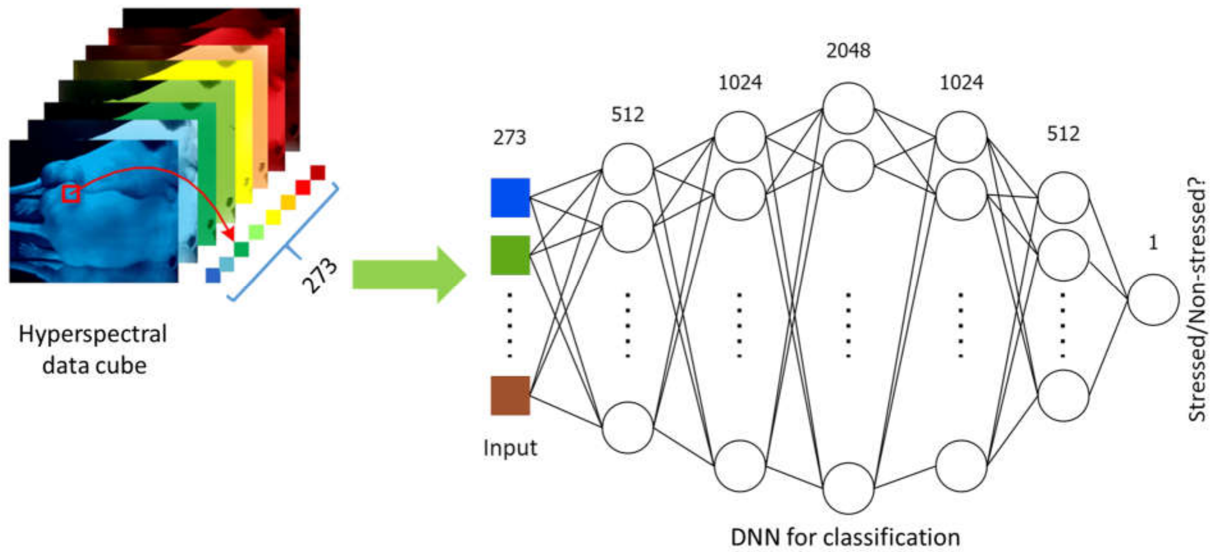

Figure 3.18 Layout of the proposed deep learning framework for identification of the stressed pixel points

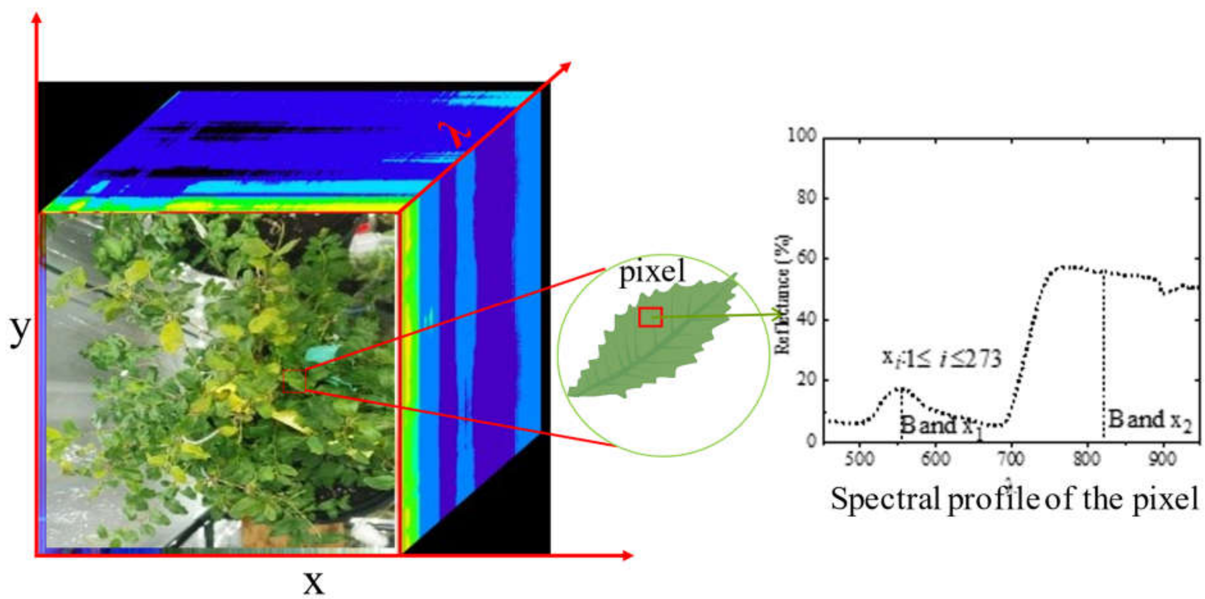

Figure 3.19 Demonstration of the spectral profile of a pixel

5.1.2 Data Preparation

To generate the training and test data sets, the hyperspectral data collected on 06/24/2022, 07/15/2022, 07/22/2022, 08/02/2022, 08/12/2022, and 08/26/2022 are considered. A set of two thousand pixels were randomly selected from each of the four monitored trenches on each day of monitoring. The resulting data set contained $6 \times 4 \times 2000 = 48000$ data points. Each data point comprised a one-dimensional (1D) vector characterized by 273 elements. Fifty percents (50%) of the available data were randomly chosen for training, and the remaining 50% were used for evaluation. Each input feature was transformed individually and scaled to a range of $[0,1]$ to ensure better convergence.

5.2 Results and discussion

5.2.1 The classification result by DNN

The test data set in this study contains 11,628 positive (stressed) samples and 12,372 negative (non-stressed) samples. Several evaluation metrics are considered to assess the performance of the proposed deep learning-based stress identification technique. A true positive (TP) is an outcome where the model correctly predicts the positive class. Similarly, a true negative (TN) is an outcome where the model correctly predicts the negative class. On the other hand, a false positive (FP) is an outcome where the model incorrectly predicts the positive class. Furthermore, a false negative (FN) is an outcome where the model incorrectly predicts the negative class. Table 3.1 presents the results of deep learning-based stress detection. It is observed that the trained model produces high TP and TN values and low FP and FN values, which indicate an excellent predictive performance of the proposed DNN. Other evaluation metrics considered in this study are accuracy, precision, recall, and F1 score, which are defined as follows:

$$Accuracy = \frac{TP + FP}{TP + FP + TN + FN}$$

$$Precision = \frac{TP}{TP + FP}$$

$$Recall = \frac{TP}{TP + FN}$$

$$F1 = \frac{2TP}{2TP + FP + FN}$$

Accuracy measures what percentage of all the test samples are correctly classified. Precision implies what percentage of the positive predictions are true positives. Recall denotes the percentage of actual positive samples correctly identified. Last but not least, the F1 score is the harmonic mean of precision and recall. The trained DNN produces an accuracy, precision, recall, and F1 score of 96.2%, 97.4%, 94.9%, and 96.1%, respectively. These values indicate that the proposed deep learning approach is bestowed with a very high degree of classification accuracy. A more detailed quantitative evaluation of stress levels is a scope for future work.

Table 3.1 Results of deep learning-based stress detection

Metric	TP	FP	FN	TN	Accuracy	Precision	Recall	F1 Score
Score	11,324	304	610	11,762	0.962	0.974	0.949	0.961

5.2.2 Identifying the most important bands

Shapley Additive Explanations (SHAP) is a concept derived from the game theory and used to explain the output of machine learning models (Lundberg and Lee, 2017). SHAP values help interpret how much a given feature or input contributes, positively or negatively, to the target outcome or prediction. It connects optimal credit allocation with local explanations using the Shapley values from game theory and their related extensions, where a Shapley value is the average marginal contribution of an instance of a feature among all possible coalitions. The key idea of SHAP is to calculate the Shapley values for each feature of the sample to be interpreted, where each Shapley value represents the impact that the feature with which it is associated, generates in the prediction.

In this project, each feature (band) was ranked according to the impact with respect to its associated Shapley values, and the top ten features are plotted in Fig. 3.20. It is observed that bands 163, 8, 124, 9, 126, 122, 121, 119, 128, and 118 have the greatest impact on the model in the decreasing order. On the left side of the figure, each feature is ordered according to its importance. The color represents the values that each feature can take, red for high values and blue for low values. Therefore, if the feature values (e.g., for band 163) are high (red), the Shapley values are low and consequently pushed towards class 0 (or non-stressed). On the other hand, when the feature values are low (blue), the Shapley values are high and consequently pushed towards class 1 (stressed). Similar conclusions can likewise be drawn for other bands also. This affords a great deal of interpretability to the predictions of the deep learning model.

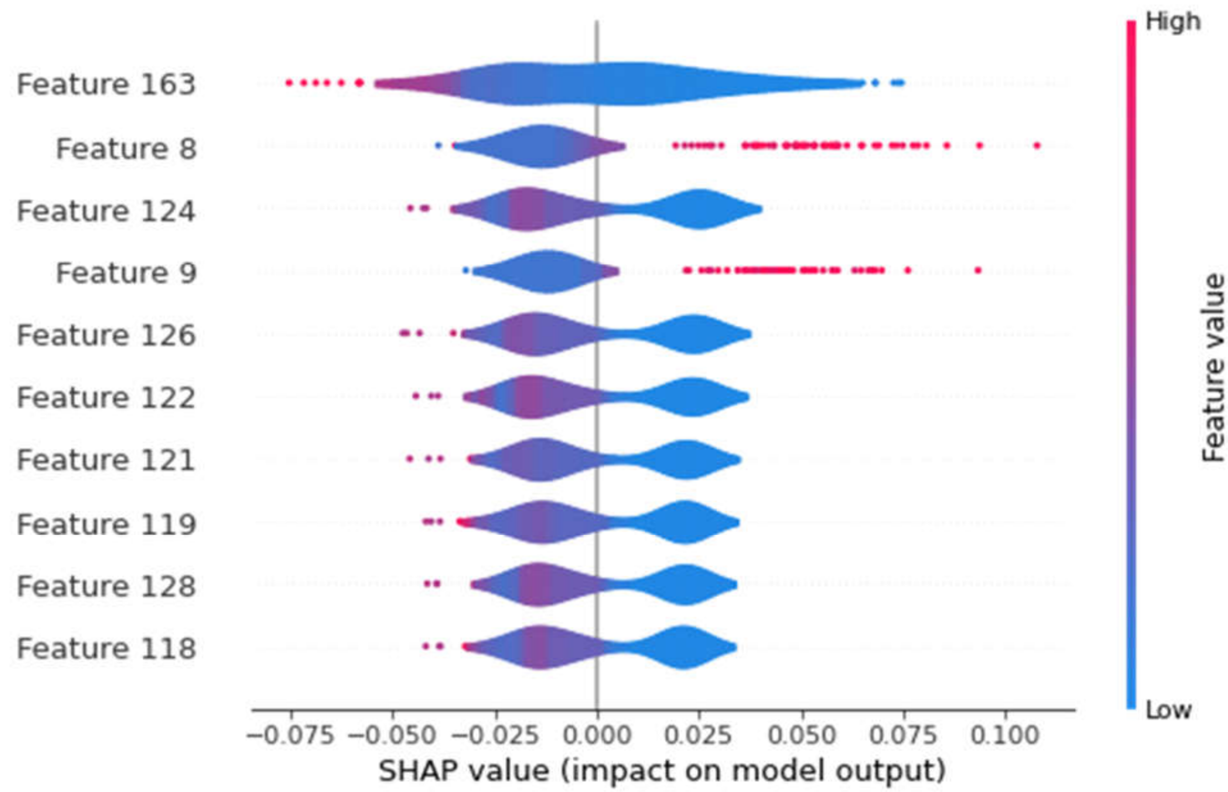

Figure 3.20 Summary of SHAP analysis

In the SHAP plot, the dot in the negative region means the feature value corresponds to the prediction that the smaller of the element value at Feature163 is prone to yield the class 'nonstress' and vice versa, while the dots around the zero indicates that they do not make too much difference in terms of stress state discrimination. For instance, the red dots are basically located in the far left of the SHAP axis, which illustrates that the more negative of the element values produces more negative effect on the nonstress state. In other words, large values at Feature163 characterize the stress status of the plants. In contrast, large values at Feature8 and Feature9 help the discrimination of stress states. In the SHAP plot, Feature represents the band in the VNIR range. To understand the significance of each band, the significance of the first100 bands with a decreasing order in SHAP plot are converted into columns as shown in Fig. 3.21. According to the band distribution, the VNIR can be divided into four regions. The red box represents the range of 671-720 nm, which is the red edge as illustrated in Figure 3.9. Red edge is sensitive to the stress occurrence on vegetations, which has been practiced in many stress factors, such as heavy mental contamination and saline soils. It is noted that the bands within 620-670 nm show great significance as for stress status differentiation. This range corresponds to the absorption of the chlorophyll that is the major plant pigment that works in both photosynthesis and photoprotection. When it comes to photoprotection, the stress factors basically generate some oxidative species in plant cells to prevent the metabolism and chlorophyll from counteracting the oxidative substances in order to maintain healthy status of the plant. Likewise, the secondary pigment in plants, carotenoid also displays huge significance as indicated by the bands in purple box around 530 nm. The last region is basically located in the NIR range that is reportedly dominated by the leaf mesophyll. Many bands are present in the NIR range, which demonstrates that plant cell structural components make a difference to identify the gas treatment stressed plants.

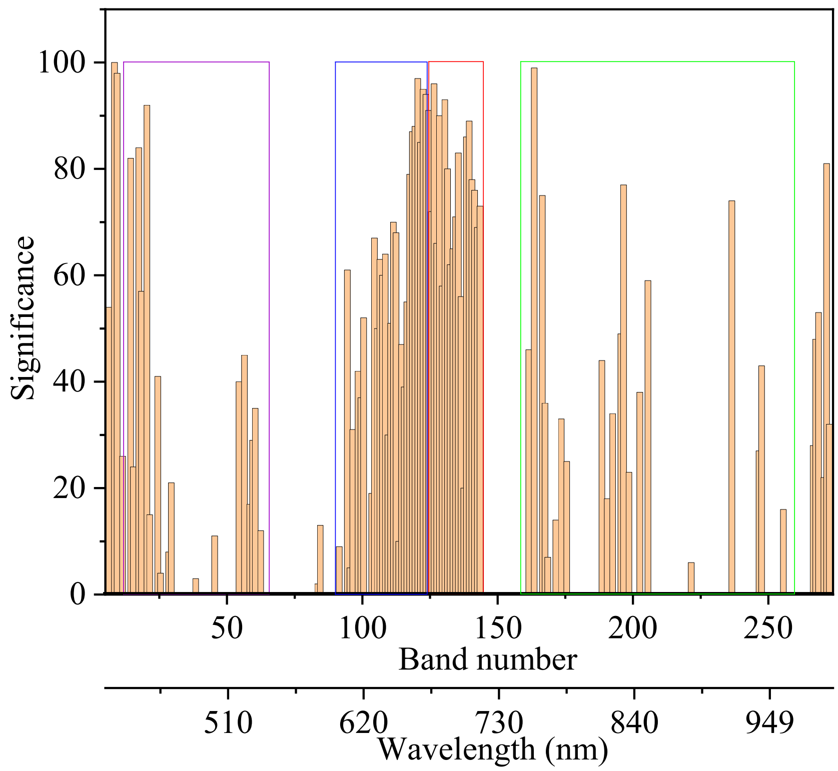

Figure 3.21 Significance of each band in VNIR to discriminate stressed plants

Beyond the band significance, the SHAP plot offers a view of how to differentiate the non-stressed plant from the stressed ones by the relative magnitude of band (Feature) values. Figure 3.22 presents the correlation of the magnitude of band values with the health stress. The plot is derived from a combination of band significance and the positive/negative effect on the determination of non-stressed status. If a higher value at the band is required, it is assigned as positive; otherwise, it is negative. As shown in Figure 3.22, the bands above zero mean that the non-stressed plant is associated with higher values in those bands. In this regard, the relative spectral intensity in VNIR can be speculated between nonstress and stress states. As indicated in Figure 3.22, a non-stressed plant yields higher intensities in the range of 420-560 nm and 750-950 nm and lower values between 600-720 nm in comparison with the stressed plants. In general, the close bands should somewhat be correlated due to their close wavelengths. However, some close bands in NIR show a reverse effect, which may be attributed to the undiscovered mechanisms that regulate the intensity in those narrow band regions, such as 770-780 nm and 845-852 nm. As depicted in Figure 3.22, the non-stressed plant should give a higher intensity between 400-600 nm and the NIR range as well as a smaller value in 600-730 nm than that of the stressed plants. This statement is consistent with the previous observations that natural gas leakage increases the hyperspectral reflectance red edge and chlorophyll-characterized absorption around 600 nm (Noomen et al., 2008; Barnes et al., 1992). Smith et al. (2004) observed the decrease in NIR on the canopy of winter wheat and bean plants in the simulated methane gas leakage experiment.

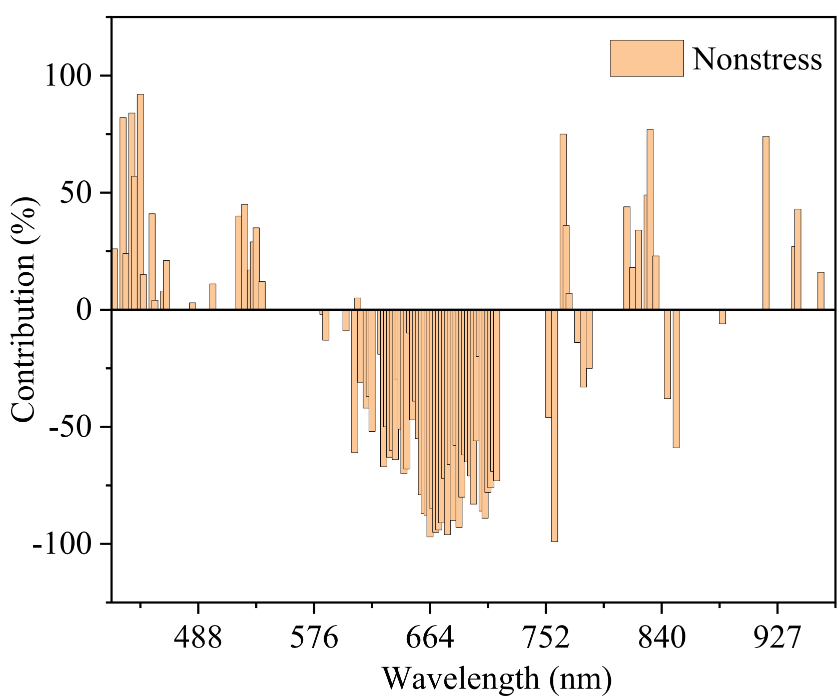

Figure 3.22 The relative change of the bands in VNIR to demonstrate the non-stress state

The spectral change in the visible range is associated with the generic response of the plant to the stress in pigment's concentration change. The pigments were measured in lab by the ultraviolet spectrometer and the pigment concentration change along with the field test is presented in Figure 3.14. It can be seen that both pigments increase after the methane gas treatment in comparison with the control condition. The increase in the carotenoid explains the decrease in the reflectance in the range of 500-550 nm for the stressed plants while the increase of the chlorophyll-featured absorption in response of the methane stress can be compromised by the observation that the chlorophyll increase is relatively low as opposed to the carotenoid as indicated by the lower (a+b)/(x+c) in Fig. 3.14. This means that the control plants basically contain more chlorophyll and thus lower reflectance than the gas-treated plants. The implication agrees with the indication in Figure 3.22 that the control plants yield a lower reflectance intensity between 600 nm and 720 nm.

5.3 Conclusion

This study investigates the use of an MLP-based DNN to classify the plants with or without the methane gas treatment and provides the indication of the features for the stressed plant from the perspective of spectral profiles. Based on the classification example, the proposed DNN can successfully classify the plant with an overall accuracy of 96.2%. The DNN also provides an indication that the 'red edge' chlorophyll-featured bands are the most informative in terms of the classification. By considering the marginal contribution of each element, the distribution of the element values demonstrates that the methane stressed plant should display a lower intensity in the NIR and 500-600 nm as well as a higher intensity in the range of chlorophyll absorption between 600 nm and 720 nm in comparison with the control group. This indication is also proven by the bio-chemical measurement of the plant pigments and therefore can be a reliable criterion for the identification of methane gas affected plants in the field practice.

VI. Future Work

The proposed HSI mapping will be tested in a real-world case to validate its feasibility and effectiveness. The thermal contrast technique will be fused with other data to enhance the applicability as so many heat sources may induce a false alert. More in-depth research will be conducted on the gas leakage detection on the more complex scenarios in the future.

VII. References

Accettura Margot, 2018, Methods for the Detection of Subterranean Methane Leakage. Thesis. Rochester Institute of Technology.

Adjorlolo, C., Mutanga, O., Cho, M.A. and Ismail, R., 2013. Spectral resampling based on user-defined inter-band correlation filter: C3 and C4 grass species classification. International Journal of Applied Earth Observation and Geoinformation, 21, pp.535-544.

Agarap, A. F., 2018. Deep learning using rectified linear units (ReLU). arXiv preprint arXiv:1803.08375.

Ahanger, M.A., Akram, N.A., Ashraf, M., Alyemeni, M.N., Wijaya, L. and Ahmad, P., 2017. Plant responses to environmental stresses-from gene to biotechnology. AoB Plants, 9(4).

Alonso, M.C., Malpica, J.A. and de Agirre, A.M., 2011. Consequences of the Hughes phenomenon on some classification techniques. In Proceedings of the ASPRS 2001 annual conference, pp.1-5.

Alvarez, R.A., Zavala-Araiza, D., Lyon, D.R., Allen, D.T., Barkley, Z.R., Brandt, A.R., Davis, K.J., Herndon, S.C., Jacob, D.J., Karion, A. and Kort, E.A., 2018. Assessment of methane emissions from the US oil and gas supply chain. Science, 361(6398), pp.186-188.

Amari, S. I., 1993. Backpropagation and stochastic gradient descent method. Neurocomputing, 5(4-5), pp.185-196.

Arellano, P., Tansey, K., Balzter, H. and Boyd, D.S., 2015. Detecting the effects of hydrocarbon pollution in the Amazon Forest using hyperspectral satellite images. Environmental Pollution, 205, pp.225-239.

Asaari, M.S.M., Mishra, P., Mertens, S., Dhondt, S., Inzé, D., Wuyts, N. and Scheunders, P., 2018. Close-range hyperspectral image analysis for the early detection of stress responses in individual plants in a high-throughput phenotyping platform. ISPRS Journal of Photogrammetry and Remote Sensing, 138, pp.121-138.

Audebert, N., Le Saux, B., and Lefèvre, S., 2019. Deep learning for classification of hyperspectral data: A comparative review. IEEE Geoscience and Remote Sensing Magazine, 7(2), pp.159-173.

Banica, V., Carles, R. and Staffilani, G., 2008. Scattering theory for radial nonlinear Schrödinger equations on hyperbolic space. Geometric and Functional Analysis, 18(2), pp.367-399.

Barnes, J. D., Balaguer, L., Manrique, E., Elvira, S., and Davison, A. W., 1992. A reappraisal of the use of DMSO for the extraction and determination of chlorophylls a and b in lichens and higher plants. Environmental and Experimental botany, 32(2), pp.85-100.

Behmann, J., Steinrücken, J. and Plümer, L., 2014. Detection of early plant stress responses in hyperspectral images. ISPRS Journal of Photogrammetry and Remote Sensing, 93, pp.98-111.

Bellante, G.J., Powell, S.L., Lawrence, R.L., Repasky, K.S. and Dougher, T., 2014. Hyperspectral detection of a subsurface CO2 leak in the presence of water stressed vegetation. PloS One, 9(10), p.e108299.

Blackburn, G.A., 2007. Hyperspectral remote sensing of plant pigments. Journal of Experimental Botany, 58 (4), pp.855–867

Bouabdallah, S., 2007. Design and Control of Quadrotors with Application to Autonomous Flying (No. THESIS). Epfl.

Brodetsky, I. and Savic, M., 1993. Leak monitoring system for gas pipelines. In 1993 IEEE International Conference on Acoustics, Speech, and Signal Processing, Vol. 3, pp. 17-20.

Carter GA, Knapp AK, 2001. Leaf optical properties in higher plants: linking spectral characteristics to stress and chlorophyll concentration. American Journal of Botany, 88, pp. 677–684.

Carter, G.A. and Miller, R.L., 1994. Early detection of plant stress by digital imaging within narrow stress-sensitive wavebands. Remote Sensing of Environment, 50(3), pp.295-302.

Chen, Y., Lin, Z., Zhao, X., Wang, G., and Gu, Y., 2014. Deep learning-based classification of hyperspectral data. IEEE Journal of Selected Topics in Applied Earth Observations and Remote Sensing, 7(6), pp.2094-2107.

Cotrozzi, L. and Couture, J.J., 2020. Hyperspectral assessment of plant responses to multi - stress environments: Prospects for managing protected agrosystems. Plants, People, Planet, 2(3), pp.244-258.

D’Ambrosio, N., Szabo, K., and Lichtenthaler, H., 1992. Increase of the fluorescence ratio F690/F735 during the autumnal chlorophyll beak-down. Radiation and Environmental Biophysics, 31, pp.51–62.

De Swaef, T., Maes, W.H., Aper, J., Baert, J., Cougnon, M., Reheul, D., Steppe, K., Roldán-Ruiz, I. and Lootens, P., 2021. Applying RGB-and thermal-based vegetation indices from UAVs for high-throughput field phenotyping of drought tolerance in forage grasses. Remote Sensing, 13(1), pp.147-171.

Drew, M.C., 1991. Oxygen deficiency in the root environment and plant mineral nutrition. In: Jackson, M.B., Davies, D.D., Lambers, H. (Eds.), Plant Life Under Oxygen Deprivation. SPB Academic Publishing, The Hague, pp.303–316.

Elvanidi, A., Katsoulas, N., Ferentinos, K.P., Bartzanas, T. and Kittas, C., 2018. Hyperspectral machine vision as a tool for water stress severity assessment in soilless tomato crop. Biosystems Engineering, 165, pp.25-35.

Erb, R.J., 1993. Introduction to backpropagation neural network computation. Pharmaceutical Research, 10(2), pp.165-170.

Foody, G.M., 2002. Status of land cover classification accuracy assessment. Remote Sensing of Environment, 80 (1), pp.185–201.

Frings, J. and Walk, T., 2011. Distributed fiber optic sensing enhances pipeline safety and security. Oil, Gas (Hamburg), pp.37-41.

Furness, R.A. and van Reet, J.D., 1998. Pipeline Leak Detection Technologies in Pipeline Rules of Thumb Handbook.

Gerhards, M., Schlerf, M., Mallick, K. and Udelhoven, T., 2019. Challenges and future perspectives of multi-/Hyperspectral thermal infrared remote sensing for crop water-stress detection: A review. Remote Sensing, 11(10), pp.1240-1264.

Gittins, C.M., Lawrence, W.G. and Marinelli, W.J., 1998. Frequency-agile bandpass filter for direct detection lidar receivers. Applied Optics, 37(36), pp.8327-8335.

Goncalves, M.D.A., Silva, C.B. and Pedras, M.H., 1996. Slug measurements in gas-oil pipeline.

Havaux, M., 2014. Carotenoid oxidation products as stress signals in plants. The Plant Journal, 79(4), pp.597-606.

Hecht-Nielsen, R., 1992. Theory of the backpropagation neural network. In Neural networks for perception. Academic Press, pp. 65-93.

Hegazy, T., Fazio, P., and Moselhi, O., 1994. Developing practical neural network applications using back-propagation. Computer-Aided Civil and Infrastructure Engineering, 9(2), pp.145-159.

Hennessy, A., Clarke, K. and Lewis, M., 2020. Hyperspectral classification of plants: A review of waveband selection generalisability. Remote Sensing, 12(1), pp.113-134.

Ho, Y., and Wookey, S., 2019. The real-world-weight cross-entropy loss function: Modeling the costs of mislabeling. IEEE Access, 8, pp.4806-4813.

Jacquemoud, S., Verhoef, W., Baret, F., Bacour, C., Zarco-Tejada, P.J., Asner, G.P., Franois, C., Ustin, S.L., 2009. PROSPECT + SAIL models: a review of use for vegetation characterization. Remote Sensing of Environment, 113 (Suppl. 1), S56–S66.

Jadin, M.S., Taib, S. and Ghazali, K.H., 2014. Feature extraction and classification for detecting the thermal faults in electrical installations. Measurement, 57, pp.15-24.

Jones, H.G., Serraj, R., Loveys, B.R., Xiong, L., Wheaton, A. and Price, A.H., 2009. Thermal infrared imaging of crop canopies for the remote diagnosis and quantification of plant responses to water stress in the field. Functional Plant Biology, 36(11), pp.978-989.

Kale, K.V., Solankar, M.M., Nalawade, D.B., Dhumal, R.K. and Gite, H.R., 2017. A research review on hyperspectral data processing and analysis algorithms. Proceedings of the National Academy of Sciences, India Section A: Physical Sciences, 87(4), pp.541-555.

Karberg, J.M., Beattie, K.C., O'Dell, D.I. and Omand, K.A., 2015. Salinity tolerance of common reed (Phragmites australis) at the Medouie Creek restoration site, Nantucket MA. Wetland Science Practice, 32, pp.19-23.

Ketkar, N., 2017. Stochastic gradient descent. In Deep Learning with Python: a Hands-on Introduction (pp. 113-132). Springer Link, Apress, Berkeley, CA.

Khulief, Y.A., Khalifa, A., Mansour, R.B. and Habib, M.A., 2012. Acoustic detection of leaks in water pipelines using measurements inside pipe. Journal of Pipeline Systems Engineering and Practice, 3(2), pp.47-54.

Kooistra, L., Salas, E.A.L., Clevers, J.G.P.W., Wehrens, R., Leuven, R.S.E.W., Nienhuis, P.H. and Buydens, L.M.C., 2004. Exploring field vegetation reflectance as an indicator of soil contamination in river floodplains. Environmental Pollution, 127(2), pp.281-290.

Koyro, H.W., 2006. Effect of salinity on growth, photosynthesis, water relations and solute composition of the potential cash crop halophyte Plantago coronopus (L.). Environmental and Experimental Botany, 56(2), pp.136-146.

Lakkaraju, V. R., Zhou, X., Apple, M. E., Cunningham, A., Dobeck, L. M., Gullickson, K., and Spangler, L. H., 2010. Studying the vegetation response to simulated leakage of sequestered CO2 using spectral vegetation indices. Ecological Informatics, 5(5), pp.379-389.

Lara, M.Á., Diezma, B., Lleó, L., Roger, J.M., Garrido, Y., Gil, M.I. and Ruiz-Altisent, M., 2016. Hyperspectral Imaging to Evaluate the Effect of Irrigation Water Salinity in Lettuce. Applied Sciences, 6(12), pp.412-428.

Lassalle, G., Elger, A., Credoz, A., Hédacq, R., Bertoni, G., Dubucq, D. and Fabre, S., 2019. Toward quantifying oil contamination in vegetated areas using very high spatial and spectral resolution imagery. Remote Sensing, 11(19), pp.2241-2265.

Lassalle, G., Credoz, A., Hédacq, R., Fabre, S., Dubucq, D. and Elger, A., 2018. Assessing soil contamination due to oil and gas production using vegetation hyperspectral reflectance. Environmental science & technology, 52(4), pp.1756-1764.

Lazhar, A., Hadj-Taïeb, L. and Hadj-Taïeb, E., 2013. Two leaks detection in viscoelastic pipeline systems by means of transient. Journal of Loss Prevention in the Process Industries, 26(6), pp.1341-1351.

Lee, X., Fuentes, J.D., Staebler, R.M. and Neumann, H.H., 1999. Long‐term observation of the atmospheric exchange of CO2 with a temperate deciduous forest in southern Ontario, Canada. Journal of Geophysical Research: Atmospheres, 104(D13), pp.15975-15984.

Li, J., Cheng, J. H., Shi, J. Y., and Huang, F., 2012. Brief introduction of back propagation (BP) neural network algorithm and its improvement. In Advances in computer science and information engineering. Springer, Berlin, Heidelberg, (pp. 553-558).

Li, S., Song, W., Fang, L., Chen, Y., Ghamisi, P., and Benediktsson, J. A., 2019. Deep learning for hyperspectral image classification: An overview. IEEE Transactions on Geoscience and Remote Sensing, 57(9), pp.6690-6709.

Lichtenthaler, H.K. and Buschmann, C., 2001. Chlorophylls and carotenoids: Measurement and characterization by UV-VIS spectroscopy. Current Protocols in Food Analytical Chemistry, 1(1), pp.F4-3.

Lichtenthaler, H.K., 1996. Vegetation stress: an introduction to the stress concept in plants. Journal of Plant Physiology, 148(1-2), pp.4-14.

Liou, J.J., Huang, C.I., Bayraktaroglu, B., Williamson, D.C. and Parab, K.B., 1996. Bias and temperature dependencies of base and collector leakage currents of AlGaAs/GaAs heterojunction bipolar transistors. Solid-State Electronics, 39(3), pp.415-426.

Lowe, A., Harrison, N. and French, A.P., 2017. Hyperspectral image analysis techniques for the detection and classification of the early onset of plant disease and stress. Plant Methods, 13(1), pp.1-12.

Lowry, M.N., 2002. Performance-based regulation of utilities. Energy LJ, 23, pp.383-393.

Lu, H., Iseley, T., Behbahani, S. and Fu, L., 2020. Leakage detection techniques for oil and gas pipelines: State-of-the-art. Tunnelling and Underground Space Technology, 98, pp.103249-103266.

Lundberg, S. M., and Lee, S. I., 2017. A unified approach to interpreting model predictions. Advances in Neural Information Processing Systems, 30.

Ma, P., Fan, L., and Chen, G., 2023. Hyperspectral reflectance for determination of steel rebar corrosion and Cl− concentration. Construction and Building Materials, 368, pp.130506-130515.

Manolakis, D., Truslow, E., Pieper, M., Cooley, T. and Brueggeman, M., 2013. Detection algorithms in hyperspectral imaging systems: An overview of practical algorithms. IEEE Signal Processing Magazine, 31(1), pp.24-33.

Mahesh, S., Manickavasagan, A., Jayas, D.S., Paliwal, J. and White, N.D.G., 2008. Feasibility of near-infrared hyperspectral imaging to differentiate Canadian wheat classes. Biosystems Engineering, 101(1), pp.50-57.

Manley, P.V., Sagan, V., Fritschi, F.B. and Burken, J.G., 2019. Remote sensing of explosives-induced stress in plants: Hyperspectral imaging analysis for remote detection of unexploded threats. Remote Sensing, 11(15), pp.1827-1845.

Melo, R.O., Costa Filho, C.F.F. and Costa, M.G.F., 2014. Leak detection of natural gas with based on the components of color spaces RGB and HSI using novelty filter. IEEE Latin America Transactions, 12(8), pp.1560-1565.

Micro Hyperspec Imaging Sensors, https://www.headwallphotonics.com/hubfs/MicroHyperspec%20Sensor%2004May2022.pdf

Miikkulainen, R., Liang, J., Meyerson, E., Rawal, A., Fink, D., Francon, O., Raju, B., Shahrzad, H., Navruzyan, A., Duffy, N., and Hodjat, B., 2019. Evolving deep neural networks. In Artificial intelligence in the age of neural networks and brain. Academic Press Computing, pp. 293-312.

Mirzaei, M., Verrelst, J., Marofi, S., Abbasi, M. and Azadi, H., 2019. Eco-friendly estimation of heavy metal contents in grapevine foliage using in-field hyperspectral data and multivariate analysis. Remote Sensing, 11(23), pp.2731-2753.

Moghimi, A., Yang, C., Miller, M.E., Kianian, S.F. and Marchetto, P.M., 2018. A novel approach to assess salt stress tolerance in wheat using hyperspectral imaging. Frontiers in Plant Science, pp.1182-1199.

Murvay, P.S. and Silea, I., 2012. A survey on gas leak detection and localization techniques. Journal of Loss Prevention in the Process Industries, 25(6), pp.966-973.

Narayan, S., 1997. The generalized sigmoid activation function: Competitive supervised learning. Information Sciences, 99(1-2), pp.69-82.

Noomen, M., Van der Meer, F. and Skidmore, A., 2005, June. Hyperspectral remote sensing for detecting the effects of three hydrocarbon gases on maize reflectance. In International Symposium of Remote Sensing of Environment (31), pp.20-24.

Noomen, M.F., Skidmore, A.K. and Van der Meer, F.D., 2003, May. Detecting the influence of gas seepage on vegetation, using hyperspectral remote sensing. In 3rd EARSel Workshop on Imaging Spectroscopy (May), pp.13-16.

Noomen, M.F., Smith, K.L., Colls, J.J., Steven, M.D., Skidmore, A.K. and Van Der Meer, F.D., 2008. Hyperspectral indices for detecting changes in canopy reflectance as a result of underground natural gas leakage. International Journal of Remote Sensing, 29(20), pp.5987-6008.

Noomen, M.F., van der Werff, H.M. and van der Meer, F.D., 2012. Spectral and spatial indicators of botanical changes caused by long-term hydrocarbon seepage. Ecological Informatics, 8, pp.55-64.

Noriega, L., 2005. Multilayer perceptron tutorial. School of Computing. Staffordshire University, 4, 5.

Paoletti, M. E., Haut, J. M., Plaza, J., and Plaza, A., 2019. Deep learning classifiers for hyperspectral imaging: A review. ISPRS Journal of Photogrammetry and Remote Sensing, 158, pp.279-317.

Parry, B., Mactaggart, R. and Toerper, C., 1992. Compensated volume balance leak detection on a batched LPG pipeline. In Proceedings of the International Conference on Offshore Mechanics and Arctic Engineering. American Society of Mechanical Engineers, pp.501-501.

Paulus, S. and Mahlein, A.K., 2020. Technical workflows for hyperspectral plant image assessment and processing on the greenhouse and laboratory scale. GigaScience, 9(8), p.giaa090.

Plant, G., Kort, E.A., Murray, L.T., Maasakkers, J.D. and Aben, I., 2022. Evaluating urban methane emissions from space using TROPOMI methane and carbon monoxide observations. Remote Sensing of Environment, 268, pp.112756-112770.

PHMSA, 2021. Underground Natural Gas Storage Facility Safety Site Assessment Report, October 2021, U.S. Department of Transportation, Pipeline and Hazardous Materials Safety Administration (PHMSA). https://portal.phmsa.dot.gov/analytics/saw.dll?Portalpages&PortalPath=%2Fshared%2FPDM%20Public%20Website%2F_portal%2FPublic%20Reports&Page=Infrastructure

PHMSA, 2022. U.S. Department of Transportation, Pipeline and Hazardous Materials Safety Administration (PHMSA). https://portal.phmsa.dot.gov/analytics/saw.dll?Portalpages&PortalPath=%2Fshared%2FPDM%20Public%20Website%2F_portal%2FSC%20Incident%20Trend&Page=All%20Reported

Postaire, J.G., Zhang, R.D. and Lecocq-Botte, C., 1993. Cluster analysis by binary morphology. IEEE Transactions on Pattern Analysis and Machine Intelligence, 15(2), pp.170-180.

Provin, T. and Pitt, J.L., 2001. Managing soil salinity. Texas FARMER Collection.

Qi, Y., Dennison, P.E., Jolly, W.M., Kropp, R.C. and Brewer, S.C., 2014. Spectroscopic analysis of seasonal changes in live fuel moisture content and leaf dry mass. Remote Sensing of Environment, 150, pp.198-206.

Ramchoun, H., Ghanou, Y., Ettaouil, M., and Janati Idrissi, M.A., 2016. Multilayer perceptron: Architecture Optimization and Training.

Ren, F., Pearton, S.J. and Kim, J., 2016. Quasi-two-dimensional β-gallium oxide solar-blind photodetectors with ultrahigh responsivity. Journal of Materials Chemistry C, 4(39), pp.9245-9250.

Roy, I.G., 2015. On computing first and second order derivative spectra. Journal of Computational Physics, 295, pp.307-321.

Sandberg, G. and Goransson, P., 1988. A symmetric finite element formulation for acoustic fluid-structure interaction analysis. Journal of Sound Vibration, 123(3), pp.507-515.

Sankaran, S., Mishra, A., Maja, J.M. and Ehsani, R., 2011. Visible-near infrared spectroscopy for detection of Huanglongbing in citrus orchards. Computers and Electronics in Agriculture, 77(2), pp.127-134.

Saunois, M., Stavert, A.R., Poulter, B., Bousquet, P., Canadell, J.G., Jackson, R.B., Raymond, P.A., Dlugokencky, E.J., Houweling, S., Patra, P.K., and Ciais, P., 2020. The global methane budget 2000–2017. Earth System Science Data, 12(3), pp.1561-1623.

Shah, S.H., Houborg, R. and McCabe, M.F., 2017. Response of chlorophyll, carotenoid and SPAD-502 measurement to salinity and nutrient stress in wheat (Triticum aestivum L.). Agronomy, 7(3), pp.61-82.

Signoroni, A., Savardi, M., Baronio, A., and Benini, S., 2019. Deep learning meets hyperspectral image analysis: A multidisciplinary review. Journal of Imaging, 5(5), pp.52-68.

Sims, D.A. and Gamon, J.A., 2002. Relationships between leaf pigment content and spectral reflectance across a wide range of species, leaf structures and developmental stages. Remote Sensing of Environment, 81(2-3), pp.337-354.

Slonecker, E.T., 2018. Analysis of the effects of heavy metals on vegetation hyperspectral reflectance properties. In Advanced Applications in Remote Sensing of Agricultural Crops and Natural Vegetation, pp. 49-66.

Smirnoff, N., 1998. Plant resistance to environmental stress. Current Opinion in Biotechnology, 9(2), pp.214-219.

Smith, K.L., Steven, M.D. and Colls, J.J., 2004. Use of hyperspectral derivative ratios in the red-edge region to identify plant stress responses to gas leaks. Remote Sensing of Environment, 92(2), pp.207-217.

Smith, K.L., Steven, M.D. and Colls, J.J., 2005. Plant spectral responses to gas leaks and other stresses. International Journal of Remote Sensing, 26(18), pp.4067-4081.

Song, S., Gong, W., Zhu, B. and Huang, X., 2011. Wavelength selection and spectral discrimination for paddy rice, with laboratory measurements of hyperspectral leaf reflectance. ISPRS Journal of Photogrammetry and Remote Sensing, 66(5), pp.672-682.

Sperl, J.L., 1991. System pinpoints leaks on Point Arguello offshore line. Oil and Gas Journal, 89(36).

Sultana, W., Begum, F., Saifuzzaman, M., Nessa, A. and Salahuddin, A.B.M., 1999. Salt tolerance of three barley cultivars of early growth stage. The Bangladesh Journal of Science and Technology, 1(1), pp.29-34.

Sun, W., Li, C., Ling, S., Reddy, R.V., Pacheco, J.L., Asmann, M., Wilken, G. and Franco, R.J., 2011, March. Laboratory study of sour localized/pitting corrosion. In CORROSION 2011. OnePetro.

Sze, V., Chen, Y. H., Yang, T. J., and Emer, J. S., 2017. Efficient processing of deep neural networks: A tutorial and survey. Proceedings of the IEEE, 105(12), pp.2295-2329.

Thenkabail, P.S., Mariotto, I., Gumma, M.K., Middleton, E.M., Landis, D.R. and Huemmrich, K.F., 2013. Selection of hyperspectral narrowbands (HNBs) and composition of hyperspectral twoband vegetation indices (HVIs) for biophysical characterization and discrimination of crop types using field reflectance and Hyperion/EO-1 data. IEEE Journal of Selected Topics in Applied Earth Observations and Remote Sensing, 6(2), pp.427-439.

Thorhaug, A., Richardson, A.D. and Berlyn, G.P., 2006. Spectral reflectance of Thalassia testudinum (Hydrocharitaceae) seagrass: low salinity effects. American Journal of Botany, 93(1), pp.110-117.

Thorp, K.R., Wang, G., Bronson, K.F., Badaruddin, M. and Mon, J., 2017. Hyperspectral data mining to identify relevant canopy spectral features for estimating durum wheat growth, nitrogen status, and grain yield. Computers and Electronics in Agriculture, 136, pp.1-12.

Tokarczyk, P., Montoya, J., Schindler, K., 2012. An evaluation of feature learning methods for high resolution image classification. ISPRS Annals of the Photogrammetry, Remote Sensing, and Spatial Information Sciences, I-3, pp.389–394.

Tsai, F. and Philpot, W., 1998. Derivative analysis of hyperspectral data. Remote Sensing of Environment, 66(1), pp.41-51.

Uddin, M.Z., 2015. A local feature-based facial expression recognition system from depth video. In Emerging Trends in Image Processing, Computer Vision and Pattern Recognition, pp. 407-419.

Udelhoven, T., Schlerf, M., Segl, K., Mallick, K., Bossung, C., Retzlaff, R., Rock, G., Fischer, P., Müller, A., Storch, T. and Eisele, A., 2017. A satellite-based imaging instrumentation concept for hyperspectral thermal remote sensing. Sensors, 17(7), pp.1542-1566.

Van derWerff, H., Van der Meijde, M., Jansma, F., Van der Meer, F. and Groothuis, G.J., 2008. A spatial-spectral approach for visualization of vegetation stress resulting from pipeline leakage. Sensors, 8(6), pp.3733-3743.

Verde, C. and Visairo, N., 2001, September. Bank of nonlinear observers for the detection of multiple leaks in a pipeline. In Proceedings of the 2001 IEEE International Conference on Control Applications (CCA'01) (Cat. No. 01CH37204), pp.714-719.

Verde, C., 2001. Multi-leak detection and isolation in fluid pipelines. Control Engineering Practice, 9(6), pp.673-682.

Vogelmann, J.E., Rock, B.N. and Moss, D.M., 1993. Red edge spectral measurements from sugar maple leaves. Remote Sensing, 14(8), pp.1563-1575.

Wang, F., Gao, J. and Zha, Y., 2018. Hyperspectral sensing of heavy metals in soil and vegetation: Feasibility and challenges. ISPRS Journal of Photogrammetry and Remote Sensing, 136, pp.73-84.

Wang, H., Chen, J., Lin, H. and Yuan, D., 2010. Research on effectiveness of hyperspectral data on identifying rice of different genotypes. Remote Sensing Letters, 1(4), pp.223-229.

Wythoff, B. J., 1993. Backpropagation neural networks: a tutorial. Chemometrics and Intelligent Laboratory Systems, 18(2), pp.115-155.

Xia, X., Guo, W., Tan, S. and Liu, H., 2017. Synechococcus assemblages across the salinity gradient in a salt wedge estuary. Frontiers in Microbiology, 8, pp.1254-1266.

Yang, X., Ye, Y., Li, X., Lau, R. Y., Zhang, X., and Huang, X., 2018. Hyperspectral image classification with deep learning models. IEEE Transactions on Geoscience and Remote Sensing, 56(9), pp.5408-5423.

Yu, K., Li, F., Gnyp, M.L., Miao, Y., Bareth, G., Chen, X., 2013. Remotely detecting canopy nitrogen concentration and uptake of paddy rice in the Northeast China Plain. ISPRS Journal of Photogrammetry and Remote Sensing 78, pp.102–115.

Zhang, T.T., Zeng, S.L., Gao, Y., Ouyang, Z.T., Li, B., Fang, C.M. and Zhao, B., 2011. Using hyperspectral vegetation indices as a proxy to monitor soil salinity. Ecological Indicators, 11(6), pp.1552-1562.

Zhou, H., Sun, M., Ren, X. and Wang, X., 2021. Visible-Thermal Image Object Detection via the Combination of Illumination Conditions and Temperature Information. Remote Sensing, 13(18), p.3656-3666.

Zhu, L., Chen, Z., Wang, J., Ding, J., Yu, Y., Li, J., Xiao, N., Jiang, L., Zheng, Y. and Rimmington, G.M., 2014. Monitoring plant response to phenanthrene using the red edge of canopy hyperspectral reflectance. Marine Pollution Bulletin, 86(1-2), pp.332-341.